MEASUREMENTS OF THE PROPERTIES OF THE HIGGS-LIKE BOSON
IN THE FOUR LEPTON DECAY CHANNEL
WITH THE ATLAS DETECTOR

Approved by:

Dr. Stephen J. Sekula

Professor of Physics

Dr. Ryszard Stroynowski

Professor of Physics

Dr. Fredrick Olness

Professor of Physics

Dr. Peng Tao

Professor of Chemistry

MEASUREMENTS OF THE PROPERTIES OF THE HIGGS-LIKE BOSON IN THE FOUR LEPTON DECAY CHANNEL WITH THE ATLAS DETECTOR

A Dissertation Presented to the Graduate Faculty of the

Dedman College: School of Humanities and Sciences

Southern Methodist University

in

Partial Fulfillment of the Requirements

for the degree of

Doctor of Philosophy

with a

Major in Physics

by

Tingting Cao

(B.S., Tsinghua University, 2008)

May 14, 2016

ACKNOWLEDGMENTS

As a PHD student, I am enormously grateful to have the fortune of meeting and working with a remarkable group of people. This thesis would not be made possible without the help and support provided by them over the last couple years. First and foremost I wish to thank my supervisor, Stephen J. Sekula, for giving me the freedom to pursue my own interests, encouraging me to work on challenging problems and teaching me to maintain abroad perspective. Particularlly, I appreciate his tireless support of the work in this thesis, and his precious hours spent on end teaching me simple lessons in particle physics. I also thank Ryszard Stroynowski for positioning me to succeed in a large colloration. His support enabled me to work and sustain life at CERN in pursuit of my degree, which was instrumental in furthering my career afterwards. When I set myself ambitious goals, he helped to ensure they became a reality.

I was extremly lucky to work with a bunch of talented people on the spin and parity measurement of Higgs boson. Many thanks to Kirill Prokefiev, Stefano Rosati, Roberto DiNardo and Attlia Krasznakorkay for the great help and guide on the very-first-time physics analysis, which resulted into this thesis. Also thank Lars Egholm Pedersen for working together on BDT method. I owe thanks many other collaborators in the ATLAS HSG2 and HSG7 group; this is truly a shared piece of work.

I want thank ATLAS TDAQ and trigger group for completing my initial service. Thank Joerge Stelzer and Frank Winklmeier for helping and instructing me on the work of trigger core software. Thank Emanuel Strauss, Ivana Radoslavova Hristova and Tae Min Hong for the help and guide on ATLAS trigger system. Great thanks to

Sami Kama for the help on teaching me the TDAQ system and improving my coding skill.

I was fortunate to have the generous support of multiple benefactors during my studies. Firstly I want to send a wider thank-you to the Physics department of SMU and the SMU ATLAS group for repeatedly supporting my research and funding years of my time at cern. It is due to the awesome group I was able to conduct the research which went into this thesis. Also, there many people at the Southern Methodist University who helped me along the way. I would like to thank my committee members, Fredrik Olness, Peng Tao, Ryszard Stroynowski and Stephen Sekula, for carefully reviewing this disertation. Many thanks to the great people of SMU ATLAS group. Thank Jingbo Ye, Bob Kehoe, Ryszard Stroynowski, Stephen Sekula and Hulin Wang for great help on my research. Their advices and comments helped me extending my perspective and furthering my professional development. My great thanks to Aidan Randle-Conde for his tremendous and invaluable help at the begining of my research. He was very patient and professional to teach me how to start the service work, the physics anlysis and taking shifts. He helped me on almost everything not only my ATLAS research but also the life at CERN. All the Feynman Diagrams in this thesis were made by Feynman diagram maker which developed by him. I want to thank the graduated students from our group, Ryan Rois, Renat Ishmukhatemov and Rozmin Daya for helping me to start on ATLAS experiment and settle at CERN. Thanks to Justin Ross and Amit Kumar for maintaining computing systems which my works had to run on.

Lastly, thanks to my family and friends for alway having my back. Mom, thank you for your love and all that you have done, and still do, behind the scenes over the years and for all of the packages and gifts. Thanks to everyone, mentioned here or not, for making my graduate school a wonderful and enjoyable journey.

Cao, Tingting B.S., Tsinghua University, 2008

Measurements of the properties of the Higgs-like boson
in the four lepton decay channel
with the ATLAS detector

Advisor: Professor Stephen J. Sekula

Doctor of Philosophy degree conferred May 14, 2016
Dissertation completed Dec 03, 2015

On July 4, 2012, experimental physicists from both the A Toroidal LHC Apparatus (ATLAS), and the Compact Muon Solenoid (CMS) experiments at the Large Hadron Collider(LHC), reported evidence for the existence of a particle consistent with the Higgs boson at the level of 5 standard deviations, with a mass around 125 GeV. In March 2013, in the light of the updated ATLAS and CMS results, CERN announced that the new particle was indeed a Higgs boson. Having analyzed two-and-a-half times more data than was available for the discovery announcement in July, the confidence of observation has risen to 10 standard deviations. The experiments were also able to show that the properties of the particle as well as the ways it interacts with other particles were well-matched with those of a Higgs boson, which is expected to have spin 0 and even(+) parity .

This dissertation presents Higgs property measurements using the "golden" channel $H \to ZZ^* \to \ell^+\ell^-\ell'^+\ell'^-$, where $\ell, \ell' = e, \mu$. A clear excess of events over the background is observed at $m_H = 124.3$ GeV in the combined analysis of the two datasets with a significance of 6.6 standard deviations, corresponding to a background fluctuation probability of 2.7×10^{-11}. The mass of the Higgs-like boson is measured to be $m_H = 124.3^{+0.6}_{-0.5}(\text{stat.})^{+0.5}_{-0.3}(\text{syst.})$ GeV. The signal strength (the ratio of the observed cross section to the expected Standard Model (SM) cross section) at this mass

is found to be $\mu = 1.7 \pm 0.5(\text{stat.}) \pm 0.4(\text{syst.})$. My key contribution has been the analysis of the spin-parity quantum numbers, one of the essential measurements to establishing the new boson as the Higgs boson. This analysis is performed on events that are most consistent with decays of the new boson. It is performed on the events with resonstructed four-lepton invariant mass, $m_{4\ell}$, satisfying 115 GeV $< m_{4\ell}<$ 130 GeV. The Higgs-like boson is found to be compatible with the SM expectation of $J^P = 0^+$ when comapred pairwise with $J^P = 0^-,\ 1^+,\ 1^-,\ 2^+$ and 2^-.

In 2013, two of the theoretical physicists who predicted the existence of the Standard Model Higgs boson, Peter Higgs and Franois Englert, were awarded the Nobel Prize in Physics. Physicists have now to pursue their measurements to determine if this Higgs particle corresponds indeed to the SM Higgs boson or if it is part of a new physics scenario.

TABLE OF CONTENTS

LIST OF FIGURES . . . xi

LIST OF TABLES . . . xix

CHAPTER

1. Preface . . . 1

2. Theoretical Introduction . . . 3

2.1. Units . . . 3

2.2. The Standard Model . . . 3

2.2.1. Matter particles . . . 4

2.2.2. Forces and carrier particles . . . 5

2.2.3. Unanswered questions and the Standard Model . . . 6

2.3. The SM Higgs Mechanism . . . 8

2.4. Expected Properties of the SM Higgs . . . 18

2.5. Higgs production and decay mechnisms . . . 23

2.5.1. Production mechanisms at hadron colliders . . . 23

3. Introduction of ATLAS detector . . . 25

3.1. Large Hadron Collider (LHC) . . . 25

3.2. ATLAS detector . . . 26

3.2.1. Tracking System . . . 28

3.2.2. Muon Spectrometer . . . 28

3.2.2.1. The toroid magnets . . . 33

3.2.2.2. Muon chamber types . . . 34

3.2.3. Calorimetry . . . 35

3.2.3.1. Liquid Argon (LAr) electromagnetic Calorimeter . . . 38
3.2.3.2. Hadron Calorimeter . . . 39
3.2.4. Forward detectors . . . 40
3.2.5. Trigger System . . . 41
3.3. Magnet system . . . 43
3.4. Conclusions . . . 46
4. Particle Selection . . . 48
4.1. Muon Reconstuction and Identification . . . 49
4.1.1. Reconstruction and identification algorithms in ATLAS . . . 49
4.1.2. Reconstruction and identification efficiency . . . 52
4.1.3. Muon resolution . . . 57
4.1.4. Muon trigger . . . 57
4.2. Electron . . . 65
4.2.1. $E-p$ combination for electrons . . . 71
4.2.2. Electron calibration . . . 71
5. Event Selection and Backgrounds Estimate . . . 75
5.1. Event Selection . . . 75
5.2. Background Estimate . . . 79
5.2.1. Backgrounds Introduction . . . 80
5.2.2. ZZ^* Background . . . 81
5.2.3. Background $\ell\ell+\mu\mu$ . . . 81
5.2.4. Background $\ell\ell+ee$ . . . 86
5.2.4.1. Background estimation from $3\ell+X$ . . . 89
5.2.4.2. Background estimation from the $\ell\ell$+XX region using the transfer-factor method . . . 93

5.2.4.3. Summary of reducible background estimates for $\ell\ell + ee$ 96

5.2.5. Shape of the reducible background contributions 96

6. Production Rate and Mass of a New Heavy Boson 99

6.1. Signal and background yield 99

6.2. Background ZZ^* 100

6.3. Mass and signal strength 104

7. Spin-Parity Quantum Number Measurement of the New Boson 108

7.1. Modeling spin and parity states 108

7.1.1. Scattering Amplitudes 110

7.2. Matrix element 111

7.3. Monte Carlo simulations 113

7.4. Re-weighting validation 116

7.5. Measured observables and parameters 116

7.6. Final state interference 123

8. Hypothesis Testing 124

8.1. Spin-parity discriminating variables 124

8.2. Statistical treatment 124

8.3. Boosted Decision Tree (BDT) 126

8.3.1. BDT Training 126

8.3.2. PDF construction 129

8.3.3. Backgrounds 130

8.3.4. Systematic uncertainties 130

8.3.5. Summary of BDT strategy 133

8.3.6. Expected exclusion (μ=1) 134

8.3.7. Expected separation significance (μ=1) for the spin 2 samples with non-universal couplings 134

9. Results 146

9.1. Results of spin and parity measurement 146

9.2. Results of Higgs properties measurements at $H \to ZZ^* \to 4\ell$ 149

10. Conclusions 150

10.1. Establishing the New Boson as the Higgs Boson Using ATLAS Data 150

10.2. Conclusion of combination 152

10.3. Outlook and Prospects for Future Measurements 154

APPENDIX

A. APPENDIX 155

A.1. Physical Constants and Conversion Factors 155

A.2. MC Samples 156

A.3. JHU Monte Carlo Validation 156

A.4. Reco-truth unfolding method 161

REFERENCES 162

LIST of FIGURES

Figure Page

2.1. Elementary particles included in the Standard Model 5

2.2. (a) A ground state of the ferromagnet, with all spins aligned; (b) another ground state, with all spins rotated; (c) a low-energy spin-wave excitation.[40] 9

2.3. The sombrero potential with an unstable state at $\phi = 0$ and minima around a circle.[41] 11

2.4. Definition of the shifted fields, representing fluctuations about the stable equilibrium state (red dot, on right), instead of the unstable point (green dot, centre).[42] 12

2.5. The Feynman diagrams of dominant Higgs decay. 20

2.6. The Feynman diagrams of Higgs production. 21

2.7. The Feynman diagrams of Higgs decaying to gluons. 22

2.8. The Feynman diagrams of Higgs to photons decay. 22

2.9. The SM Higgs boson production cross sections as a function of the center of mass energy, $\sqrt{s}$, for pp collisions.[32] 24

3.1. Cut-away view of the ATLAS detector 27

3.2. Cut-away view of the ATLAS inner detector 30

3.3. Cut-away view of the ATLAS muon system 31

3.4. Diagrams illustrating the sensors and structural elements in (a) the barrel and (b) end-cap of the ID 34

3.5. Cut-away view of the ATLAS calorimeter detector 36

3.6. Geometry of magnet windings and tile calorimeter steel. The eight barrel toroid coils, with the end-cap coils interleaved are visible. The solenoid winding lies inside the calorimeter volume. The tile calorimeter is modelled by four layers with different magnetic properties, plus an outside return yoke. For the sake of clarity the forward shielding disk is not displayed 44

3.7. Barrel toroid as installed in the underground cavern; note the symmetry of the supporting structure. The temporary scaffolding and green platforms were removed once the installation was complete. The scale is indicated by the person standing in between the two bottom coils. Also visible are the stainless-steel rails carrying the barrel calorimeter with its embedded solenoid, which await translation towards their final position in the center of the detector.. 46

4.1. An illustration of the four types of muon reconstruction, emphasizing information from ATLAS subdetectors used for each type. 50

4.2. Efficiency of track reconstruction in the MS and ID, using STACO procedure, as a function of p_T. [36] 53

4.3. Efficiency of track reconstruction using MUONBOY, STACO and MuTag procedures, as a function of p_T. [36] 55

4.4. Muon reconstruction efficiency as a function of η for muons with $p_T >$ 20 GeV and different muon reconstruction types. CB and ST muon types are reconstructed using the Chain 1 reconstruction algorithm. CaloTag muons are used only in the region $|\eta| < 0.1$. The panel at the bottom shows the ratio between the measured and predicted efficiencies. [27] 56

4.5. Measured ID muon reconstruction efficiency as a function of η for muons with $p_T > 20$ GeV. On the left plot the efficiency is calculated with the standard selection requirements on the hit multiplicity in the ID while the requirements are relaxed on the right plot. The panel at the bottom shows the ratio between the measured and predicted efficiencies. [27] 57

4.6. p_T resolution of track reconstruction in the MS and in the ID, using the STACO procedure, as a function of p_T. [36] 58

4.7. Schema of L1 muon barrel trigger. [10] 60

4.8. L1 geometrical acceptance in the $\eta - \phi$ plane. [26] 61

4.9. L1 barrel efficiency as function of p_T for high-p_t thresholds. [26] 62

4.10. The end-cap trigger efficiency curves for high-p_T thresholds of 11, 20 and 40 GeV. [26] 63

4.11. Efficiency of the primary single muon trigger separately for L1, L2, EF at barrel region in data. [1] 64

4.12. Efficiency of the primary single muon trigger separately for L1, L2, EF at endcap region in data. [1] 65

4.13. Ratio of background efficiencies for the likelihood/cut-based menus.The uncertainties are statistical only. The ratio is shown vs. η (left) and vs. E_T (right). The light jet background samples is taken form data using electron supporting triggers to look at inclusive backgrounds samples in data. The efficiencies are calculated using objects in the electron container that also pass track quality requirements. To reject real electron contamination from Zs and Ws, electron objects which lie in the Z-peak or have MET> 25 GeV or M$_T > 40$ GeV are rejected.For the eta plot, we use > 20 GeV electrons, and for the E_T plot we use > 7 GeV electrons. 68

4.14. Crystal Ball function fits of $p_{\mathrm{T}}^{\mathrm{Cluster}}/p_{\mathrm{T}}^{\mathrm{Truth}}$ ((a), (b) and (c)) and $p_{\mathrm{T}}^{\mathrm{Track}}/p_{\mathrm{T}}^{\mathrm{Truth}}$ ((d), (e) and (f)) in various transverse momentum and pseudorapidity regions. 73

4.15. Improvement in $p_{\mathrm{T}}/p_{\mathrm{T}}^{\mathrm{Truth}}$ for Monte Carlo single electrons after the likelihood $E-p$ combination, as compared to the standard approach (E_{Cluster} only). Low and medium p_{T} ranges are shown in various η regions of the detector. 74

5.1. (a) The invariant mass distributions of $Z \to \mu^+\mu^-(\gamma)$ events in data before collinear FSR correction (filled triangles) and after collinear FSR correction (filled circles) (b) The invariant mass distributions of $Z \to \mu^+\mu^-(\gamma)$ events with a noncollinear FSR photon. The prediction of the simulation is shown before correction (red histogram) and after correction (blue histogram).[15] 79

5.2. Feyman diagrams of main Higgs to four leptons backgrounds. (a) Irreducible background ZZ^*; (b) Reducible background $\ell\ell$+jets; (c) Reducible background $t\bar{t}$ 80

5.3. The observed m_{12} distributions (filled circles) and the results of the maximum likelihood fit are presented for the four control regions: (a) inverted requirement on impact parameter significance, (b) inverted requirement on isolation, (c) $e\mu$ leading dilepton, where the backgrounds besides $t\bar{t}$ are small and not visible, and (d) same-sign subleading dilepton. The fit results are shown for the total background (black line) as well as the individual components: $Z+$ jets decomposed into $Z + b\bar{b}$ (blue line) and Z+light-flavor jets (green line), $t\bar{t}$ (dashed red line), and the combined WZ and ZZ (dashed gray line), where the WZ and ZZ contributions are estimated from simulation. 85

5.4. The distribution of the difference between the transverse momentum measured in the ID and in the MS normalized to the ID measurement, $(p_{T_{ID}} p_{T_{MS}})/p_{T_{ID}}$, for combined muons accompanying a $Z \to \ell\ell$ candidate. The data (filled circles) are compared to the background simulation (filled histograms) which has the Z+light-flavor background shown separately to distinguish the contribution from π/K in-flight decays. The additional muon is selected to be a combined muon with $p_T > 6$ GeV, which fulfills the δR requirement for the lepton separation of the analysis and in the case of $Z(\to \mu^+\mu^-)+\mu$ final state, the opposite sign pairs are required to have $m_{\mu^+\mu^-} > 5$ GeV to remove J/Ψ decays. 87

5.5. The results of a simultaneous fit to (a) $n_{hits}^{B-layer}$, the number of hits in the innermost pixel layer, and (b) r_{TRT}, the ratio of the number of high-threshold to low-threshold TRT hits, for the background components in the $3l$+X control region. The fit is performed separately for the $2\mu 2e$ and $4e$ channels and summed together in the present plots. The data are represented by the filled circles. The sources of background electrons are denoted as: light-flavor jets faking an electron (f, green dashed histogram), photon conversions (γ, blue dashed histogram) and electrons from heavy-flavor quark semileptonic decays (q, red dashed histogram). The total background is given by the solid blue histogram. 91

5.6. Invariant mass distributions of the lepton pairs in the control sample defined by a Z boson candidate and an additional same-flavor lepton pair, including all signal and background contributions, for the $\sqrt{s} = 7$ TeV and $\sqrt{s} = 8$ TeV datasets. The sample is divided according to the flavor of the additional lepton pair. In (a) and (c) the m_{12} and m_{34} distributions are presented for $\ell\ell + \mu^+\mu$ events, where $\ell\ell$ is $\mu^+\mu$ or e^+e. In (b) and (d) the m_{12} and m_34 distributions are presented for $\ell\ell + e^+e$ events. The data are shown as filled circles and the different backgrounds as filled histograms with the total background systematic uncertatinty represented by the hatched areas. The kinematic selection of the analysis is applied. Isolation and impact parameter significance requirements are applied to the first lepton pair only. The simulation is normalized to the data-driven background estimates. . . 98

6.1. The distribution of the four-lepton invariant mass, $m_{4\ell}$, for the selected candidates (filled circles) compared to the expected signal and background contributions (filled histograms) for the combined $\sqrt{s} = 7$ TeV and $\sqrt{s} = 8$ TeV data for the mass ranges: (a) 80-170 GeV, and (b) 80-600 GeV. The signal expectation shown is for a mass hypothesis of $m_H = 125$ GeV and normalized to $\mu = 1.51$ (see text). The expected backgrounds are shown separately for the ZZ^* (red histogram), and the reducible Z+jets and $t\bar{t}$ backgrounds (violet histogram); the systematic uncertainty associated to the total background contribution is represented by the hatched areas. 102

6.2. Distributions of data (filled circles) and the expected signal and backgrounds events in (a) the m_{34} m_{12} plane with the requirement of $m_{4\ell}$ in 120130 GeV. The projected distributions for (b) m_{12} and (c) m_{34} are shown for $m_{4\ell}$ in 110140 GeV, the fit range. The signal contribution is shown for $m_H = 125$ GeV and normalized to $\mu = 1.51$ (see text) as blue histograms in (b) and (c). The expected background contributions, ZZ^* (red histogram) and Z+jets plus $t\bar{t}$ (violet histogram), are shown in (b) and (c); the systematic uncertainty associated to the total background contribution is represented by the hatched areas. The expected distributions of the Higgs signal (blue) and total background (red) are superimposed in (a), where the box size (signal) and color shading (background) represent the relative density. In every case, the combination of the 7 TeV and 8 TeV results is shown. 103

6.3. Distributions of data (filled circles) and the expected signal and background events in (a) the BDT$_{ZZ^*}$ $m_{4\ell}$ plane, (b) BDT$_{ZZ^*}$ with the restriction $120 < m_{4\ell} < 130$ GeV, and (c) $m_{4\ell}$ with the additional requirement that the BDT$_{ZZ^*}$ is positive. The expected Higgs signal contribution is shown for $m_H = 125$ GeV and normalized to $\mu = 1.51$ (see text) as blue histograms in (b) and (c). The expected background contributions, ZZ^* (red histogram) and Z+jets plus $t\bar{t}$(violet histogram), are shown in (b) and (c); the systematic uncertainty associated to the total background contribution is represented by the hatched areas. The expected distributions of the Higgs signal (blue) and total background (red) are superimposed in (a), where the box size (signal) and color shading (background) represent the relative density. In every case, the combination of the 7 TeV and 8 TeV results is shown.105

6.4. The observed local p_0-value for the combination of the 2011 and 2012 data sets (solid black line) as a function of m_H; the individual results for $\sqrt{s}$ = 7TeV and 8TeV are shown separately as red and blue solid lines, respectively, The dashed curves show the expected median of the local p_0 for the signal hypothesis with signal strength $\mu = 1$, when evaluated at the corresponding m_H. The horizontal dot-dashed lines indicate the p_0 values corresponding to local significances of 1-8σ. 106

6.5. (a) The 68% and 95% confidence level (CL) contours in the μ m_H plane for the inclusive analysis. (b) The profile likelihood as a function of the inclusive signal strength μ for the individual channels ($4e$, green line; 4μ, blue line; $2e2\mu$, red line; $2\mu 2e$, yellow line) as well as for their combination (black lines); the scan for the combination of all channels is shown both with (solid line) and without (dashed line) systematic uncertainties. The value of m_H is fixed to 125.36 GeV while all the other nuisance parameters are profiled in the fit. In every case, the combination of the 7TeV and 8TeV results is shown. 107

7.1. Definitions of production and decay angles in $X \to ZZ^{(*)} \to 4l$ decay [34]. 109

7.2. Standard Model final state observables. The figures contain in order: $\cos(\theta_1)$, $\cos(\theta_2)$, m_{Z1}, m_{Z2}, Φ, and are evaluated after full detector simulation and selection. The red distributions are reweighted from the sample with couplings $g_1 = 1$, $g_2 = 1 + i$, $g_4 = 1 + i$ while the black distributions are reweighted from $g_1 = 1$, $g_2 = 1$, $g_4 = 1$. 117

7.3. Reweighted (red) and directly-generated (black) final state observables. The figures show in order: $\cos(\theta_1)$, $\cos(\theta_2)$, m_{Z1}, m_{Z2}, Φ. The distributions shown correspond to the set of couplings: $g_1 = 1$, $g_2 = 1$, $g_4 = 1$ and are evaluated after full detector simulation and selection; the inset plots show the corresponding distributions for the frequency. . . . 118

7.4. Reweighted (red) and directly-generated (black) final state observables. The figures show in order: $\cos(\theta_1)$, $\cos(\theta_2)$, m_{Z1}, m_{Z2}, Φ. The distributions shown correspond to the set of couplings: $g_1 = 1$, $g_2 = 1 + i$, $g_4 = 0$ and are evaluated after full detector simulation and selection; the inset plots show the corresponding distributions for the frequency. . . . 119

7.5. Reweighted (red) and directly-generated (black) final state observables. The figures show in order: $\cos(\theta_1)$, $\cos(\theta_2)$, m_{Z1}, m_{Z2}, Φ. The distributions shown correspond to the set of couplings: $g_1 = 1$, $g_2 = 0$, $g_4 = 2 + 2i$ and are evaluated after full detector simulation and selection; the inset plots show the corresponding distributions for the frequency. 120

8.1. Distributions of spin and parity sensitive observables for events selected by the main analysis in the signal mass range: 115GeV $\leq m_{4\ell} \leq$ 130GeV. The expected contributions from the signal (0^+ and 0^-) and irreducible ZZ background are shown, normalized to the expected number of events for the luminosity of the data sample. The contributions from reducible non-ZZ backgrounds, which are derived using data and normalized to the luminosity of the data sample, are also shown. (a) ϕ, (b) $\cos\theta_1$,(c) $\cos\theta_2$, (d) m_{12}, (e) m_{34}. 139

8.2. Distributions of spin and parity sensitive observables for events selected by the main analysis in the signal mass range: 115GeV $\leq m_{4\ell} \leq$ 130GeV. The expected contributions from the signal (0^+ and 0^+_h) and irreducible ZZ background are shown, normalized to the expected number of events for the luminosity of the data sample. The contributions from reducible non-ZZ backgrounds, which are derived using data and normalized to the luminosity of the data sample, are also shown. (a) ϕ, (b) $\cos\theta_1$,(c) $\cos\theta_2$, (d) m_{12}, (e) m_{34}. 140

8.3. Distributions of spin and parity sensitive observables forevents selected by the main analysis in the signal mass range: 115GeV $\leq m_{4\ell} \leq$ 130GeV. The expected contributions from the signal (0^+ and 2^+_m) and irreducible ZZ background are shown, normalized to the expected number of events for the luminosity of the data sample. The contributions from reducible non-ZZ backgrounds, which are derived using data and normalized to the luminosity of the data sample, are also shown. (a) $\cos\theta^*$, (b) ϕ_1, (c) ϕ, (d) $\cos\theta_1$,(e) $\cos\theta_2$, (f) m_{12}, (g) m_{34}. 141

8.4. BDT distributions for $J^p = 0^+$ vs. $J^p = 0^-$, discrimination (left column), $J^p = 0^+$ vs. $J^p = 0_h^+$ discrimination (middle column) and $J^p = 0^+$ vs. $J^p = 2_m^+$ discrimination (right column). The top row show the training as perform on the 8 TeV (2012) MC, while the bottom row shows the corresponding figures for 7 TeV (2011). The BDT training is performed on an mixture of the four different final states corresponding to their expected normalisations. In all cases, the 0^+ hypothesis is labeled as signal while the alternative distribution is labeled as background. The samples are divided in two; a test and a training sample. The BDT optimisation has been done on the training sample and overtraining is evaluated by comparing the resulting ROC integrals as presented in Tab. 8.2. 142

8.5. BDT distributions for the $J^p = 0^+$ vs. ZZ-continuum discriminant. The BDT training is performed per final state, where the columns from left to right shows the 4e, 4μ, $2e2\mu$, $2\mu2e$ final states. The top row show the training as perform on the 8 TeV (2012) MC, while the bottom row shows the corresponding figures for 7 TeV (2011). In all cases, the 0^+ hypothesis is labeled as signal while the ZZ-continuum distribution is labeled as background. The samples are divided in two; a test and a training sample. The BDT optimisation has been done on the training sample and overtraining is evaluated by comparing the resulting ROC integrals as presented in Tab. 8.2. . 143

8.6. Example of validation of the KDE procedure. The presented figures are taken from the $2e2\mu$ final state. Top row: Two dimensional distributions of $J^p = 0^+$ vs $J^p = 2_m^+$ (first axis) and $J^p = 0^+$ vs ZZ^* (second axis) for process types $J^p = 0^+$ (left column), $J^p = 2_m^+$ (middle column) and ZZ^* (right row). The scatter indicate the simulated Monte Carlo events, while the contours show the smoothed distribution arrived at with the KDE approach. Center row: The color of each bin shows the difference between the event distribution and smoothed KDE distribution from above in units of the statistical uncertainty. The corresponding pull distribution for each process type is found in the bottom row. It is seen that the center of each is close to zero and width close to one. 144

8.7. MC toys distributions for the different hypothesis tests performed. The three figures from left to right show, $J^p = 0^-$, 0^+, $J^p = 0_h^+$, 0^+ and $J^p = 2_m^+$, 0^+. The test statistic values are calculated as described in Sec. 8.2. In each figure a Standard Model Higgs is assumed and its value indicated by 'test statistic data'. The reported p-values correspond to the tail integral of the alternative models. 145

9.1. Variation of the medians of the log-likelihood ratio distribution generated for varying fractions of $q\bar{q}$ in a mixed $q\bar{q}$ and ggF production for testing the 2_m^+ hypothesis when assuming the spin-0^+ hypothesis. Each distribution is generated with more than 500k Monte Carlo experiments. In each experiment the expected numbers of signal and background events are fixed to the observed yields. The blue and red data points correspond to the median values for the 0^+ and 2_m^+ hypotheses, respectively, for each fraction. The black points represent the log-likelihood values observed in data. The lines connecting the points are there to guide the eye. 147

10.1. Expected and observed ratio of profiled likelihoods for the combination of channels as a function of the fraction of the $q\bar{q}$ spin-2 production mechanism. The green and yellow bands represent, respectively, the one and two standard deviation bands for the $J^P = 0^+$ (a) and for the $J^P = 2^+$ (b) hypotheses.[5] 152

10.2. Expected (blue dashed line) and observed (black solid line) confidence level, $\mathrm{CL}_s(J^P = 2^+)$, of the $J^P = 2^+$ hypothesis as a function of the fraction of $q\bar{q}$ production of the spin-2 particle.[5] 153

A.1. Comparison between JHU (blue) and POWHEG (red) predictions for SM Higgs p_T and acoplanarity. The ratio between the two predictions is also shown with the statistical error on the bottom of each plot. 159

A.2. Comparison of predicted p_T spectra for resonances produced in gg collisions. (a) JHU 0^+ and PowHeg Standard Model Higgs. (b) JHU states with different spin and parity. 160

LIST OF TABLES

Table Page

2.1. Production cross section (in pb) for $m_H = 125$ GeV [32] 24

3.1. Main parameters of the inner-detector system.......................... 29

3.2. Main parameters of the muon spectrometer. Numbers in brackets for the MDTs and the RPCs refer to the final configuration of the detector in 2009 32

3.3. Main parameters of the calorimeter system 37

3.4. Main parameters of the ATLAS magnet system 45

4.1. The muon identification menus 52

4.2. Definition of electron discriminating variables [22]. 67

4.3. The electron identification menus [13]................................. 70

4.4. Definitions of the p_{T} and $|\eta|$ regions used in this analysis. 72

5.1. Expected contribution of the $\ell\ell + \mu\mu$ background sources in each of the control regions. 83

5.2. Data driven $\ell\ell + \mu\mu$ background estimates for the $\sqrt{s} = 7$ TeV and $\sqrt{s} = 8$ TeV data, expressed as yields in the reference control region, for the combined fit and fits to the individual control regions. In the individual control regions only the total Z+jets contribution can be determined, while the $e\mu + \mu\mu$ control region is only sensitive to the $t\bar{t}$ background. The statistical uncertainties are also shown. 84

5.3. Estimates for the $\ell\ell + \mu\mu$ background in the signal region for the full m_{4l} mass range for the $\sqrt{s} = 7$ TeV and $\sqrt{s} = 8$ TeV data. The Z+jets and $t\bar{t}$ background estimates are data-driven and the WZ contribution is from simulation. The decomposition of the Z+jets background in terms of the $Zb\bar{b}$ and the Z+light-flavor-jets contributions is also provided.................................. 88

5.4. The fit results for the $3l+X$ control region, the extrapolation factors and the signal region yields for the reducible $\ell\ell + ee$ background. The second column gives the fit yield of each component in the $3l+X$ control region. The corresponding extrapolation efficiency and signal region yield are in the next two columns. The background values represent the sum of the $2\mu 2e$ and $4e$ channels. The uncertainties are the combination of the statistical and systematic uncertainties. 92

5.5. Summary of the $\ell\ell + ee$ data-driven background estimates for the $\sqrt{s} = 7$ TeV and $\sqrt{s} = 8$ TeV data for the full $m_{4\ell}$ mass range. OS (SS) stands for opposite (same) sign lepton pairs. The "†" symbol indicates the estimates used for the background normalization; the other estimates are used as cross-checks. The first uncertainty is statistical, while the second is systematic. The SS data full analysis is limited to the region with $m_{4\ell}$ below 160 GeV to avoid a ZZ contribution; this region contains 70% of the expected background. 94

6.1. The number of events expected and observed for a $m_H = 125$ GeV hypothesis for the four-lepton final states in a window of $120 < m_{4\ell} < 130$GeV. The second column shows the number of expected signal events for the full mass range, without a selection on $m_{4\ell}$. The other columns show for the 120130 GeV mass range the number of expected signal events, the number of expected ZZ^* and reducible background events, the signal-to-background ratio (S/B), together with the number of observed events, for 4.5 fb^{-1} at $\sqrt{s} = 7$ TeV and 20.3 fb^{-1} at $\sqrt{s} = 8$ TeV as well as for the combined sample. 101

7.1. Choice of coupling parameters for the spin-0 and spin-2 models considered in the current analysis [18]. 111

7.2. Choice of tensor couplings configurations used for reweighting tests. . . . 115

8.1. Table of parameters used for the BDT training. The definitions of the options can be found in Table 22, 23 and 24 of [39]. The names are translated as follows: $\mathrm{N_{Trees}}$: NTrees, Shrink.: Shrinkage, MNP: NodePurityLimit, S/B: SigToBkgFraction, BSF: BaggedSampleFraction, $\mathrm{N_{Cuts}}$: nCuts, Max depth: MaxDepth. All the forest of trees are moreover boosted using bagging resampling. 127

8.2. BDT summary table. The columns show in consecutive order: the two models for any training, the final state observables used as training parameters and the resulting ROC integral for the sample the training has been performed on and a statistical independent sample of equal size and the difference between the two. The ROC has been defined in such a way that a integral of 0.5 indicates no separation, and 1.0 indicates perfect separation. The differences indicate the size magnitude of overtraining and is seen to be at most at the percent level. 128

8.3. The expected exclusion for 8 TeV only of different alternative spin and parity models for the BDT analysis. The exclusions are given in terms of p-values and corresponding number of Gaussian sigmas. The 'alt' numbers reported are where a Standard Model Higgs $J^p = 0^+$ is assumed and the alternative model is excluded. The 'Null' numbers assume a alternative model and excludes the Standard Model Higgs hypothesis. The stated values take into account all the systematic uncertanties that are evaluated to be significant (impact $\geq$ 0.45%). The numbers in parenthesis indicate the values when not taking systematic uncertainties into account. The impact of including all significanct nuisance parameters is 3.8%, 7.0% and 5.0% for excluding $J^p = 0^-$, $J^p = 0_h^+$ and $J^p = 2_m^+$ respectively. The values are derived from MC toy distributions and as such have a related statistical uncertainty. The statistical uncertainty on the significances corresponds to 0.01 sigma and equvalently is of the size of the last reported digit of the p-values. 135

8.4. The expected exclusion for 7 TeV-only of different alternative spin and parity models for the BDT analysis. The exclusions are given in terms of p-values and corresponding number of Gaussian sigmas. The 'alt' numbers reported are where a Standard Model Higgs $J^p = 0^+$ is assumed and the alternative model is excluded. The stated values take into account the all systematic uncertanties that are evaluated to be significant (impact $\geq$ 0.45%). The numbers in parenthesis indicate the values when not taking systematic uncertainties into account. The values are derived from MC toy distributions and as such have a related statistical uncertainty. The statistical uncertainty on the significances corresponds to 0.01 sigma (0.02 $J^p = 0^-$, 0^+ w.o syst.) and equvalently is of the size of the last reported digit of the p-values. 135

8.5. The expected exclusion for 7 and 8 TeV-combined of different alternative spin and parity models for the BDT analysis. The exclusions are given in terms of p-values and corresponding number of Gaussian sigmas. The 'alt' numbers reported are where a Standard Model Higgs $J^p = 0^+$ is assumed and the alternative model is excluded. The stated values take into account the all systematic uncertanties that are evaluated to be significant (impact $\geq$ 0.45%). The numbers in parenthesis indicate the values when not taking systematic uncertainties into account. The values are derived from MC toy distributions and as such have a related statistical uncertainty. The statistical uncertainty on the significances corresponds to at most 0.04 sigma and equvalently is of the size of the last reported digit of the p-values. 136

8.6. The expected exclusion for 8 TeV only of different alternative spin and parity models for the BDT analysis. The exclusions are given in terms of p-values and corresponding number of Gaussian sigmas. The 'alt' numbers reported are where a Standard Model Higgs $J^p = 0^+$ is assumed and the alternative model is excluded. The stated values take into account the all systematic uncertainties that are evaluated to be significant (impact $\geq$ 0.45%). The numbers in parenthesis indicate the values when not taking systematic uncertainties into account. The values are derived from MC toy distributions and as such have a related statistical uncertainty. 137

8.7. The expected exclusion for 7 TeV only of different alternative spin and parity models for the BDT analysis. The exclusions are given in terms of p-values and corresponding number of Gaussian sigmas. The 'alt' numbers reported are where a Standard Model Higgs $J^p = 0^+$ is assumed and the alternative model is excluded. The stated values take into account the all systematic uncertainties that are evaluated to be significant (impact $\geq$ 0.45%). The numbers in parenthesis indicate the values when not taking systematic uncertainties into account. The values are derived from MC toy distributions and as such have a related statistical uncertainty. 138

8.8. The expected exclusion for 7+8 TeV only of different alternative spin and parity models for the BDT analysis. The exclusions are given in terms of p-values and corresponding number of Gaussian sigmas. The 'alt' numbers reported are where a Standard Model Higgs $J^p = 0^+$ is assumed and the alternative model is excluded. The stated values take into account the all systematic uncertainties that are evaluated to be significant (impact $\geq$ 0.45%). The numbers in parenthesis indicate the values when not taking systematic uncertainties into account. The values are derived from MC toy distributions and as such have a related statistical uncertainty. 138

9.1. For an assumed 0^+ hypothesis $\mathrm{H_0}$, the values for the expected and observed $\mathrm{p_0}$-values of the different tested spin and parity hypotheses $\mathrm{H_1}$ for the BDT and $\mathrm{J^p - MELA}$ analyses. The results are given combining the $\sqrt{s} = 7$TeV and $\sqrt{s} = 8$TeV data sets. Also given is the observed $\mathrm{p_0}$-value where 0^+ is the test hypothesis and the other spins states are the assumed hypothesis(observed*). These two observed $\mathrm{p_0}$-values are combined to provide the $\mathrm{CL_S}$ confidence level for each test hypothesis. The production mode is assumed to be 100% ggF. 148

10.1. Main parameters of the inner-detector syste 151

A.1. MC samples of different signal hypotheses used for the spin-CP analysis. 157

A.2. MC samples of final state interference used for the spin-CP analysis. . . . 158

Many thanks to Aidan Randle-Conde for making the website of Fernman diagram maker.

Chapter 1

Preface

I have worked on the ATLAS experiment since the summer of 2010. My initial service to the collaboration to earn authorship was to design and build an on-line trigger rates prediction system for shifters and experts. I worked with the TDAQ and trigger groups to enable reliable ATLAS triggering and data-taking. I used existing data of trigger rates (both L1 and HLT triggers) to derive formulas to calculate trigger rates from luminosities and cross sections; I then used these formulas to predict trigger rates with current luminosity and cross section, compare the predicted rates with the current trigger rates, and determine if the current rates are reasonable. This system alerted shifters and experts when the trigger rates became abnormal or were projected to go too high. More details of ATLAS trigger system please check the Section 3.2.5, and the specific moun trigger system can be found in the Section 4.1.4. The triggers which used for event selection at $H \rightarrow ZZ^* \rightarrow 4\ell$ channel can be found in the Section 5.1.

I have worked on the spin and parity measurement of the new Higgs-like boson since 2012. I worked on the event selection at $H \rightarrow ZZ^* \rightarrow 4\ell$ channel to get the signal samples which can be used for conresponding measurements, and the details are in Section 5.1. My direct contributions to the spin-parity measurement included:

1. Being the first to use the JHU[35] simulation software to generate samples with different spin quantum numbers; this will be discussed in Section 7.3;

2. Reweighting the MC samples using transverse momentum, to improve the physical modeling of data; details are found in Section 7.4;

3. Studied the distributions of all variables that are sensitive to spin-parity measurement; see Section 7.5;
4. Worked on the BDT training for different spin-parity samples; the details can be found in Section 8.3;
5. Performed essential statistical work for hypothesis testing; see Chapter 8 and 9 for more details.

Also I worked with the Higgs combination group to combine the measurements of different channels on ATLAS. My contributions were recognized when I was invited to give a talk titled "Measurements of Higgs Boson Properties using the ATLAS Detector" at 2nd International Conference on New Frontiers in Physics in September of 2013.[52].

Chapter 2

Theoretical Introduction

In this chapter, first of all, I describe the theoretical motivations for my analysis: the Standard Model (SM) and Higgs mechanism. Also I introduce the predicted properties of the SM Higgs including its mass, couplings to other particles, spin and parity.

2.1. Units

I will work in "God-given" units, where

$$\hbar = c = 1. \tag{2.1}$$

In this system,

$$[\text{length}] = [\text{time}] = [\text{energy}]^{-1} = [\text{mass}]^{-1}. \tag{2.2}$$

The mass (m) of a particle is therefore equal to its rest energy (mc^2), and also to its inverse Compton wavelength ($mc/\hbar$). For example,

$$m_{electron} = 9.109 \times 10^{-28} g = 0.511 \text{ MeV} = (3.862 \times 10^{-11}\text{cm})^{-1}. \tag{2.3}$$

A selection of other userful numbers and conversion factors is given in the Appendix A.1.

2.2. The Standard Model

The Standard Model is the name given in the 1970s to a theory of fundamental particles and how they interact. It incorporated all that was known about subatomic particles at the time and also predicted the existence of additional particles as well.

The theories and discoveries of thousands of physicists since the 1930s have resulted in a remarkable insight into the fundamental structure of matter: everything in the universe is found to be made from a few basic building blocks called "fundamental particles," governed by four "fundamental forces." Our best understanding of the relationships between the particles and three of these forces is encapsulated in the Standard Model of particle physics. It has successfully explained almost all experimental results and precisely predicted a wide variety of phenomena. Over time and through many experiments, the Standard Model has become established as a well-tested, though incomplete, description of nature.

2.2.1. Matter particles

All matter around us is made of elementary particles, the building blocks of matter. These particles occur in two basic types called "quarks" and "leptons." Each type consists of six particles, which are related in pairs, or "generations." The lightest and most stable particles make up the first generation, whereas the heavier and less-stable particles belong to the second and third generations. All stable matter in the universe is made from particles that belong to the first generation; any heavier particles quickly decay to the next most stable level. The six quarks are paired in three generations: the "up quark" and the "down quark" form the first generation, followed by the "charm quark" and "strange quark," then the "top quark" and "bottom (or beauty) quark." Quarks also come in three different "color charges", which are "red," "green," and "blue." When a "red," "green," and "blue" charged object are combined, this forms a "colorless" objects. Since all particles have antiparticles, and antiparticles carry anti-charge ("anti-red," "anti-green," and "anti-blue"), there is another way to form a "colorless" object, which is for a certain "color" quark and an "anti-color" quark (not necessarily of the same flavors!) to bind. Therefore, quarks only combine in ways that form colorless objects. The six leptons are similarly arranged in three generations: the “electron” and the “electron neutrino,” the “muon” and the “muon neutrino,” and the “tau” and the “tau neutrino.” The electron, the muon and the tau all have an electric charge and a sizeable mass, whereas the neutrinos are electrically neutral and have very little mass. The properties of quarks and leptons are shown in Figure 2.1.

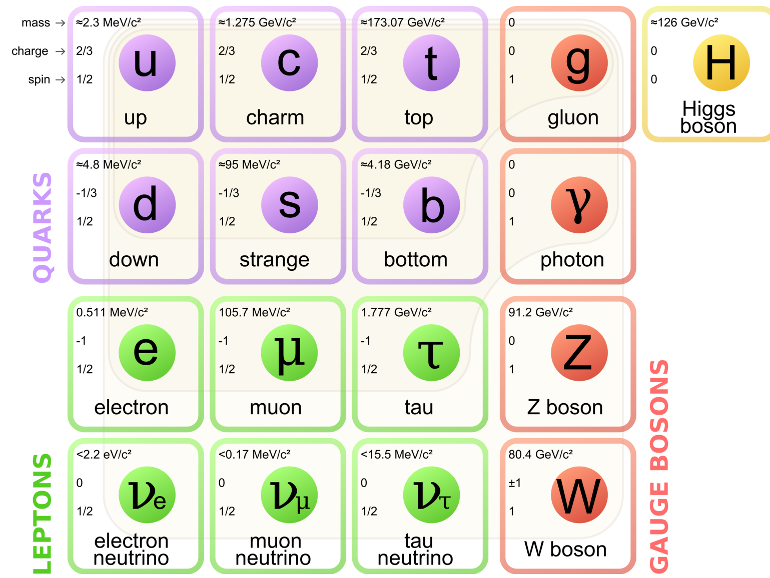

Figure 2.1. Elementary particles included in the Standard Model

2.2.2. Forces and carrier particles

There are four known fundamental forces at work in the universe: the strong force, the weak force, the electromagnetic force, and the gravitational force. They work over different ranges and have different strengths. Gravity is the weakest but it has an infinite range. The electromagnetic force also has infinite range but it is many times stronger than gravity. The weak and strong forces are effective only over a very short range and dominate only at the level of subatomic particles. Despite its name, the weak force is much stronger than gravity but it is indeed the weakest of the other three. The strong force, as the name suggests, is the strongest of all four fundamental interactions.

Three of the fundamental forces result from the exchange of force-carrier particles, which belong to a broader group of particles called "bosons." Particles of matter transfer discrete amounts of energy by exchanging bosons with each other. Each fundamental force has its own corresponding boson: the strong force is carried by the "gluon," the electromagnetic force is carried by the "photon," and the "W and Z bosons" are responsible for the weak force. Although not yet found, there might be a "graviton" that is the corresponding force-carrying particle of gravity. Known boson properties are summarized in 2.1. The Standard Model includes the electromagnetic, strong and weak forces and all their carrier particles, and explains well how these forces act on all of the matter particles. However, the most familiar force in our everyday lives, gravity, is not part of the Standard Model. Describing gravity using a quantum field theory, like that in the Standard Model, is an ongoing theoretical challenge. No one has managed to make the two mathematically compatible in the context of the Standard Model. But luckily for particle physics, when it comes to the minuscule scale of particles, the effect of gravity is so weak as to be negligible. Only when matter is in bulk, at the scale of the human body or of the planets, for example, does the effect of gravity dominate. So the Standard Model still works well despite its reluctant exclusion of one of the fundamental forces.

2.2.3. Unanswered questions and the Standard Model

Even though the Standard Model is currently the best description there is of the subatomic world, it does not explain all observations. The theory incorporates only three out of the four fundamental forces, omitting gravity. Since the formulation of the Standard Model based on then-known components of nature, more components of nature have been observed: dark matter and dark energy. In addition, neutrino mixing has been observed. The conditions under which the Big Bang occured are not explained by the Standard Model because one needs to incorporate gravity to explain the Big Bang, where conditions were likely more akin to those in a black hole, where gravity is very strong and scales are subatomic in size. There are also important questions that it does not answer, such as "What is dark matter?", or "What happened to the antimatter after the big bang?", "Why are there three generations of quarks and leptons with such a different mass scale?" and more. Last but not least is a particle called the Higgs boson, an essential component of the Standard Model.

The SM Higgs particle is a massive scalar elementary particle theorized by Robert Brout, Franois Englert, Peter Higgs, Gerald Guralnik, C. R. Hagen, and Tom Kibble in 1964 (see 1964 PRL symmetry breaking papers) and is a key building block in the Standard Model. It has no intrinsic spin, and for that reason is classified as a boson (like the gauge bosons, which have unit spin).

The Higgs boson plays a unique role in the Standard Model, by explaining why the other elementary particles, except the photon and gluon, are massive. In particular, the Higgs boson explains why the photon has no mass, while the W and Z bosons are very heavy. Elementary particle masses, and the differences between electromagnetism (mediated by the photon) and the weak force (mediated by the W and Z bosons), are critical to many aspects of the structure of microscopic (and hence macroscopic) matter. In the Standard Model, the Higgs boson generates the masses of the leptons (electron, muon, and tau) and quarks. As the Higgs boson is massive, it must interact with itself.

On 4 July 2012, the ATLAS and CMS experiments at CERN's Large Hadron Collider (LHC) announced they had each observed a new particle in the mass region around 126 GeV. This thesis will assess the consistency of this particle with the SM

Higgs boson. The Higgs boson, as proposed within the Standard Model (see Figure 2.1), is the simplest manifestation of the Brout-Englert-Higgs mechanism. Other types of Higgs bosons are predicted by other theories that go beyond the Standard Model.

2.3. The SM Higgs Mechanism

The SM Higgs mechanism, which also known as the **Englert-Brout-Higgs-Guralnik-Hagen-Kibble** mechanism, provides the means by which gauge vector bosons can acquire nonzero masses in the process of spontaneous symmetry breaking. It is a key element of the electroweak theory that forms part of the standard model of particle physics, and of many models, such as Grand Unified Theories, that go beyond it.

Since the weak interactions are of short range and very weak at low energies, it was clear that if they were mediated by an intermediate vector boson W, it must have a large mass - an apparent problem, since gauge bosons were believed to always be massless, like the photon. Some mechanism was required to give mass to the W while leaving the photon massless.

Initially, invoking spontaneous symmetry breaking was thought to introduce yet another problem: the appearance of the massless scalar Nambu-Goldstone bosons, as seemingly required by the Goldstone theorem[49, 47]. It turns out, however, that these two problems in a sense "cancel out." The mechanism is essentially a relativistic version of one that operates in a superconductor. For brevity, it is often called the "Higgs mechanism."

Spontaneous symmetry breaking

Spontaneous symmetry breaking occurs when the ground state of a system does not share the full symmetry of the underlying theory. The clearest example is that of an isotropic ferromagnet, composed of an array of spins attached to the sites of a lattice, and described by the Hamiltonian

$$H = -\frac{1}{2}\sum_{\mathbf{x},\mathbf{y}} J_{\mathbf{x}-\mathbf{y}}\mathbf{S}_{\mathbf{x}} \cdot \mathbf{S}_{\mathbf{y}}, \tag{2.4}$$

where $\mathbf{S}_{\mathbf{x}}$ denotes the spin at the lattice site $\mathbf{x}$. The strength of the interaction J depends only on the distance between the lattice sites $\mathbf{x}$ and $\mathbf{y}$, and is assumed to fall off rapidly as the distance becomes large.

This model is invariant under a simultaneous rotation of all the spins, and correspondingly the total spin

$$\mathbf{S} = \sum_{\mathbf{x}} \mathbf{S}_{\mathbf{x}} \tag{2.5}$$

is conserved. But if J is positive, then clearly the lowest energy state is one with all the spins aligned (see Figure 2.2(a)). The direction in which they point is arbitrary. Thus there is a degenerate ground state. Making a simultaneous rotation of all the spins yields another ground state, with exactly the same energy (see Figure 2.2(b)).

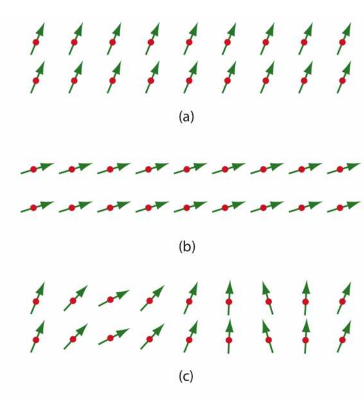

Figure 2.2. (a) A ground state of the ferromagnet, with all spins aligned; (b) another ground state, with all spins rotated; (c) a low-energy spin-wave excitation.[40]

A very important consequence of spontaneous symmetry breaking of a continuous symmetry like this one is that there are excitations whose energy goes to zero in the long wavelength limit. These are the **Goldstone** bosons or **Nambu-Goldstone** bosons. In this case these are spin waves, in which a periodic space-dependent rotation is applied to the spins (see Figure 2.2(c)). Since it costs no energy to rotate all the spins, from Figure 2.2(a) to (b), it costs very little energy to make a long-wavelength periodic change. This is the content of the **Goldstone theorem**.

Spontaneous breaking of a local gauge symmetry

The simplest relativistic field theory [46] that exhibits such spontaneous symmetry breaking is one of a complex scalar field ϕ with the Lagrangian density function

$$L = \partial_\mu \phi^* \partial^\mu \phi - V(\phi), \tag{2.6}$$

where

$$V(\phi) = m^2 \phi^* \phi + \frac{1}{2}\lambda(\phi^*\phi)^2. \tag{2.7}$$

Here, the metric is $(1, 1, 1, 1)$ and m and λ are the mass and self-interaction coupling constant of the scalar field. The model is invariant under a global change of phase

$$\phi(x) \to \phi(x)e^{i\alpha}. \tag{2.8}$$

This set of transformations defines the Abelian symmetry group U(1).

So long as $m^2 > 0$, this model is just a self-interacting scalar field, whose quanta are particles and antiparticles of mass m. Things are different, however, if $m^2 < 0$. Then $\phi = 0$ is a maximum of the potential V, representing an unstable equilibrium. Here

$$V(\phi) = -\frac{1}{2}\lambda v^2 \phi^* \phi + \frac{1}{2}\lambda(\phi^*\phi)^2, \tag{2.9}$$

where $v^2 = -2m^2/\lambda$. This is often called the sombrero potential (see Figure 2.3). Its minima now lie on the circle $|\phi|^2 = v^2/2$. So in the ground state, or vacuum state, one expects the value of ϕ to be non-zero, with a magnitude close to $v/\sqrt{2}$, but arbitrary phase. There will be a degenerate family of vacuum states $|0_\alpha\rangle$, labelled by the phase angle α.

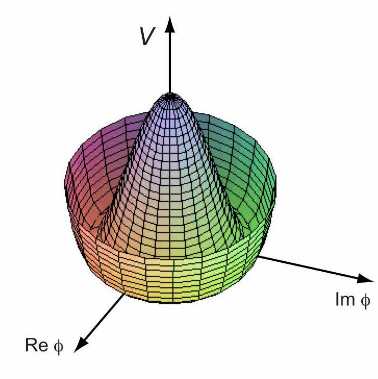

Figure 2.3. The sombrero potential with an unstable state at $\phi = 0$ and minima around a circle.[41]

For a ferromagnet, the symmetry is broken even in finite volume. For the Goldstone model, the situation is different. If this system were confined to a finite volume, then the true vacuum state would be a symmetric linear superposition of all these "ground states," in which the expectation value of ϕ would still vanish. But this is not the case for a field theory (in infinite volume). Then the states $|0_\alpha\rangle$ are mutually orthogonal, and all matrix elements between distinct vacua involving a finite number of fields vanish. Each $|0_\alpha\rangle$ is the vacuum state of a distinct Hilbert space constructed by applying the field operators to it. (Note that the representation of the canonical commutation relations on this Hilbert space is inequivalent to the usual Fock-space representation - in contrast to the situation in ordinary quantum mechanics where all irreducible representations of the Heisenberg commutation relations are unitarily equivalent.)

Nambu-Goldstone bosons appear here too. One can see this by choosing one particular minimum, say the one where ϕ is real and positive, and expanding about that point (see Figure 2.4), defining shifted real fields $\varphi_{1,2}$ by

$$\phi = \frac{1}{\sqrt{2}}(v + \varphi_1 + i\varphi_2). \tag{2.10}$$

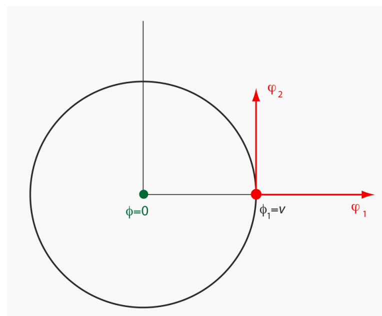

Figure 2.4. Definition of the shifted fields, representing fluctuations about the stable equilibrium state (red dot, on right), instead of the unstable point (green dot, centre).[42]

Then one finds

$$L = \frac{1}{2}[(\partial_\mu\varphi_1)^2 + (\partial_\mu\varphi_2)^2] - V, \tag{2.11}$$

with

$$V = -\frac{1}{8}\lambda v^4 + \frac{1}{2}\lambda v^2\varphi_1^2 + \frac{1}{2}\lambda v\varphi_1(\varphi_1^2 + \varphi_2^2) + \frac{1}{8}\lambda(\varphi_1^2 + \varphi_2^2)^2. \tag{2.12}$$

The first term here is merely an unimportant constant. By construction, there is no linear term, and, importantly, there is no term in φ_2^2.

Now canonical quantization can proceed as normal in terms of the fields $\varphi_{1,2}$. The model describes two kinds of particles, the ϕ_1 quanta of mass $\sqrt{\lambda}v$ and the massless ϕ_2 quanta, with cubic and quartic couplings. The ϕ_2 quanta, corresponding to a spatial variation of the phase angle, are the Nambu-Goldstone bosons. Their presence is required by the Goldstone theorem in any manifestly Lorentz covariant theory in which a continuous symmetry is spontaneously broken. (The theorem is also true for non-relativistic theories, provided that an additional assumption is satisfied.)

The global symmetry may be promoted to a local symmetry provided a corresponding gauge field is introduced, with potential A_μ. The Lagrangian is now

$$L = D_\mu \phi^* D^\mu \phi - \frac{1}{4} F_{\mu\nu} F^{\mu\nu} - V(\phi), \tag{2.13}$$

where the covariant derivative and gauge field are given by

$$D_\mu \phi = \partial_\mu \phi + ieA_\mu \phi, \qquad F_{\mu\nu} = \partial_\mu A_\nu - \partial_\nu A_\mu. \tag{2.14}$$

This Lagrangian is invariant under the local gauge transformations

$$\phi(x) \to \phi(x) e^{i\alpha(x)}, \qquad A_\mu(x) \to A_\mu - \frac{1}{e} \partial_\mu \alpha(x). \tag{2.15}$$

This is the simplest of all gauge theories, with an Abelian U(1) gauge group.

So long as $m^2 > 0$, this is ordinary scalar electrodynamics. It describes a charged particle of mass m, and its antiparticle, interacting with massless photons. But what happens if m^2 is again taken negative, say $m^2 = \frac{1}{2}\lambda v^2 < 0$ as before?

Here, too, one can make the substitution 2.10, and find that V takes the form 2.12. Now, however, there are additional quadratic terms arising from the first, kinetic term in 2.13. The Lagrangian now takes the form

$$L = \frac{1}{2}(\partial_\mu \varphi_1)^2 + \frac{1}{2}(\partial_\mu \varphi_2 + evA_\mu)^2 - \frac{1}{4} F_{\mu\nu} F^{\mu\nu} - \frac{1}{2}\lambda v^2 \varphi_1^2 + \dots, \tag{2.16}$$

where the dots denote cubic and quartic interaction terms (and the constant term). It is now clear that the second term gives the gauge field a mass. Indeed, one can introduce a new field

$$B_\mu = A_\mu + \frac{1}{ev} \partial_\mu \varphi_2, \tag{2.17}$$

so that the second term becomes a mass term for B_μ , with mass ev , and no kinetic term for φ_2 remains.

A rather neater way of describing the situation is to note that one may choose a gauge such that $\varphi_2 = 0$, so that A_μ and B_μ coincide.

This is then a model that describes only massive fields, a vector field B_μ with mass ev, interacting with a scalar field φ_1, whose mass is again $\sqrt{\lambda}v$. The apparently massless gauge field A_μ and the apparently massless scalar field φ_2 have combined to give the massive vector field B_μ. Note that the number of helicity states is unchanged: the two polarization states of A_μ and the single one of φ_2 combine to give the three of B_μ. This is the essence of the Englert-Brout-Higgs-Guralnik-Hagen-Kibble mechanism.

Evading the Goldstone theorem

How was it possible to arrive at a theory with no massless particles? To answer this question it may be helpful to start by examining one of the proofs of Goldstone's theorem. It is based on three hypotheses.

Firstly, the theory has a continuous symmetry, and correspondingly a Noether current $j_\mu(x)$ which is conserved, satisfying $\partial_\mu j_\mu = 0$. In the case of a scalar field with U(1) symmetry, this current is

$$j_\mu = -i\phi^* D_\mu \phi + i\phi D_\mu \phi^*. \tag{2.18}$$

Secondly, this symmetry is spontaneously broken; there is no invariant vacuum state, but rather a degenerate family of non-invariant vacuum states. Specifically, for any vacuum state $|0\rangle$, there exists some field ϕ (possibly composite) whose vacuum expectation value $\langle 0|\phi|0\rangle$ is not invariant. Now the generator $\mathcal{Q}$ of the transformation is the spatial integral of j^0:

$$\mathcal{Q}(t) = \int d^3\mathbf{x} j^0(t, \mathbf{x}), \tag{2.19}$$

so what this means is

$$-i\int d^3\mathbf{x}\langle 0|[j^0(0,\mathbf{x}),\phi(0)]|0\rangle \neq 0. \tag{2.20}$$

Finally, the theory is manifestly Lorentz covariant.

To determine how this argument fails in the case of a local, gauge symmetry, the key lies in the third hypothesis, that of manifest covariance. To quantize a gauge theory, one must choose a gauge, and impose a gauge-fixing condition of some kind. For the U(1) gauge theory, if one wants a formulation in terms of a Hilbert space containing only physical states, this cannot be done in a manifestly covariant way. The simplest choice is the Coulomb or radiation gauge, defined by the condition $\partial_k A^k = 0$, which is non-covariant since it depends on the choice of time axis. In this case, commutators are not required to vanish outside the light cone, and in fact fall off only like an inverse power. Consequently, the continuity equation $\partial_\mu j^\mu = 0$ no longer requires that the charge operator (Eq. 2.19) be time-independent, because when we integrate by parts the contribution from the surface term at infinity need not vanish. (In fact, $\mathcal{Q}$ is not really well defined, except inside commutators.) So it no longer follows that $k_\mu f^\mu(k) = 0$. (In the non-relativistic case, the third hypothesis of the Goldstone theorem is that there are no long-range forces involved, because that ensures that commutators fall off sufficiently rapidly at infinity that the surface integral can be dropped.)

Of course, there is an alternative, manifestly covariant way of quantizing the electromagnetic field, namely to use the Lorentz gauge, defined by $\partial_\mu A^\mu = 0$. In that case, however, the Hilbert space necessarily contains states of unphysical scalar and longitudinal photons. Here the Goldstone theorem definitely does apply, and there do exist massless Nambu-Goldstone bosons. But it turns out that they are purely gauge modes, uncoupled to the physical particles of the theory.

This mechanism is often said to exhibit "spontaneously broken gauge symmetry." That is a convenient shorthand description, but the terminology is potentially somewhat misleading. The process of quantization requires a choice of gauge, i.e., an explicit breaking of the gauge symmetry. However, the resulting theory does retain a global phase symmetry that is broken spontaneously by the choice of the phase of $\langle\phi\rangle$.

It is, however, very important that the model derives from an initial fully gauge-invariant one. In general, models involving massive vector fields are non-renormalizable. But this theory is renormalizable, as proved by 't Hooft (1971) (see gauge theories), primarily because it retains the Ward identities that play a key role in the renormalizability of quantum electrodynamics.

Non-Abelian symmetry breaking

Essentially the same mechanism can apply in the case of a non-Abelian gauge theory. The simplest example is that of a triplet of scalar fields, $\vec{\phi} = (\phi_j)$, transforming according to the three-dimensional adjoint representation of the group SO(3). The Lagrangian here is

$$L = \frac{1}{2}\overrightarrow{D_\mu\phi} \cdot \overrightarrow{D^\mu\phi} - \frac{1}{4}\vec{F}_{\mu\nu} \cdot \vec{F}^{\mu\nu} - V(|\vec{\phi}|), \tag{2.21}$$

where

$$\vec{D_\mu}\phi = \partial_\mu\vec{\phi} + g\vec{A}_\mu \times \vec{\phi}, \vec{F}_{\mu\nu} = \partial_\mu\vec{A}_\nu - \partial_\nu\vec{A}_m u + g\vec{A}_\mu \times \vec{A}_\nu, \tag{2.22}$$

and g is the gauge coupling constant.

This Lagrangian is invariant under SO(3) gauge transformations; in infinitesimal form these are

$$\delta\vec{\phi} = \overrightarrow{\delta\omega} \times \vec{\phi} \tag{2.23}$$

and

$$\delta\vec{A}_\mu = \overrightarrow{\delta\omega} \times \vec{A} - \frac{1}{g}\partial_\mu\overrightarrow{\delta\omega}, \tag{2.24}$$

where $\overrightarrow{\delta\omega} = (\delta\omega_j)$ are three infinitesimal parameters.

Now suppose that V is again chosen so that its minima are not at the symmetric point $\vec{\phi} = \vec{0}$ but on a sphere of non-zero radius, $|\vec{\phi}| = v$. Then there will as before be a degenerate family of vacuum states, characterized by vacuum expectation values lying on the sphere. For example, one such vacuum will have $\langle 0|\vec{\phi}|0\rangle = (0, 0, v) = \vec{\phi}_0$. Other points on the sphere will correspond to other vacua.

In this case, the symmetry group SO(3) is not broken completely. There is an unbroken subgroup SO(2), comprising rotations in the xy plane, which leave $\vec{\phi}_0$ unchanged. In this case, one of the three gauge bosons, the component $A_{3\mu}$ corresponding to this unbroken symmetry, remains massless. The other two $A_{1\mu}$ and $A_{2\mu}$ acquire masses, equal to gv. As before the longitudinal components of these massive gauge bosons come from the would-be Nambu-Goldstone bosons ϕ_1 and ϕ_2. Oscillations in the radial direction, described by $\phi_3 - v$, are the massive Higgs bosons.

In the case of a general symmetry group, suppose that the multiplet ϕ of real fields ϕ^α belongs to a representation of the symmetry group G with Hermitian (in fact imaginary, antisymmetric) generators T_a, and that the symmetry is spontaneously broken down to a subgroup H when ϕ acquires a non-zero expectation value ϕ_0. Then it is easy to see that the mass matrix for the vector fields is

$$(M_\nu^2)_{ab} = g^2\tilde{\phi}_0 T_a T_b \phi_0, \tag{2.25}$$

where the tilde denotes transposition. The generators of H are those generators of G for which $T_a\phi_0 = 0$. For them, the corresponding elements of M^2 vanish. So if G is of dimension n and H is of dimension m, there will be m massless gauge bosons and nm massive ones. For example, in the Weinberg-Salam model, where $G = SU(2) \times U(1)$

and $H = U(1)$, we have one massless and three massive gauge bosons.

Once again, the longitudinal components of the massive gauge bosons come from the would-be Nambu-Goldstone bosons, while the remaining components of ϕ (or rather of $\phi - \phi_0$) will acquire masses given by the scalar mass matrix,

$$(M_s^2)_{\alpha\beta} = \left(\frac{\partial^2 V}{\partial\phi^\alpha \partial\phi^\beta}\right)_{\phi=\phi_0}. \tag{2.26}$$

These are the Higgs bosons.

The primary purpose of the Englert-Brout-Higgs-Guralnik-Hagen-Kibble mechanism was to provide masses for the gauge vector bosons. A secondary effect, however, was to give masses to other fundamental particles.

Any fermion that interacts with the scalar field ϕ via an interaction term of the form $h\bar{\psi}'\phi\psi$ may acquire a mass, of order hv, by virtue of the non-zero expectation value $\langle 0|\phi|0\rangle$. In the SM, this is the mechanism that gives masses to the leptons and the quarks. These remain arbitrary parameters, however, because the masses are determined by the arbitrary coupling constants h; the top quark is heavy, for example, because it interacts relatively strongly with the Higgs field.

It is sometimes said that the Higgs field gives masses to all other particles, but that is not strictly correct. It is important to note that most of the mass of the nucleon in particular does not arise in this way. Only the masses of the quarks come from the Englert-Brout-Higgs-Guralnik-Hagen-Kibble mechanism. The larger part of the nucleon mass comes from a mechanism along the lines sketched out earlier by Nambu[46].

2.4. Expected Properties of the SM Higgs

The SM Higgs boson is a CP-even scalar of spin 0. [17] Its mass is given by $m_H = \sqrt{2\lambda}v$, where λ is the Higgs self-coupling parameter in $V(\phi)$. The expectation value of the Higgs field, $v = (\sqrt{2}G_F)^{-1/2} \approx 246$ GeV, is fixed by the Fermi coupling G_F, which is determined with a precision of 0.6 ppm from muon decay measurements.[54] The quartic coupling λ, instead, is a free parameter in the SM, and hence there is, a priori, no prediction for the Higgs mass. Moreover the sign of the mass parameter $m^2 = -\lambda v^2$ is crucial for the EW symmetry breaking to take place, but it is not specified in the SM. Therefore, if the newly discovered particle is indeed the SM Higgs boson with $m_H \simeq 125$ GeV, it implies that $\lambda \simeq 0.13$ and $|m| \simeq 88.8$ GeV. It is interesting to observe that in the SM one needs to assume that the mass term in the potential is negative in order to trigger EWSB. In other theories beyond the SM (BSM), such as supersymmetry, the analogue of the Higgs mass parameter can be made negative dynamically.

The Higgs boson couplings to the fundamental particles are set by their masses. This is a new type of interaction, very weak for ordinary particles, such as up and down quarks, and electrons, but strong for heavy particles such as the W and Z bosons and the top quark. More precisely, the SM Higgs couplings to fundamental fermions are linearly proportional to the fermion masses, whereas the couplings to bosons are proportional to the square of the boson masses. The SM Higgs boson couplings to gauge bosons, Higgs bosons and fermions are summarized in the following Lagrangian:

$$\mathcal{L} = -g_{Hf\bar{f}}\bar{f}fH + \frac{g_{HHH}}{6}H^3 + \frac{G_{HHHH}}{24}H^4 + \partial_V V_\mu V^\mu \left(g_{HVV}H + \frac{g_{HHVV}}{2}H^2\right) \quad (2.27)$$

with

$$\begin{aligned} g_{Hf\bar{f}} &= \tfrac{m_f}{v}, & g_{HVV} &= \tfrac{2m_V^2}{v}, & g_{HHVV} &= \tfrac{2m_V^2}{v^2}, \\ g_{HHH} &= \tfrac{3m_H^2}{v}, & g_{HHHH} &= \tfrac{3m_H^2}{v^2}. \end{aligned} \quad (2.28)$$

where $V = W^{\pm}$ or Z and $\delta_Z = 1/2$. As a result, the dominant mechanisms for Higgs boson production and decay involve the coupling of H to W, Z and/or the third generation quarks and leptons. Figure 2.5 shows the Feyman diagrams of dominant mechanisms of the Higgs decay.

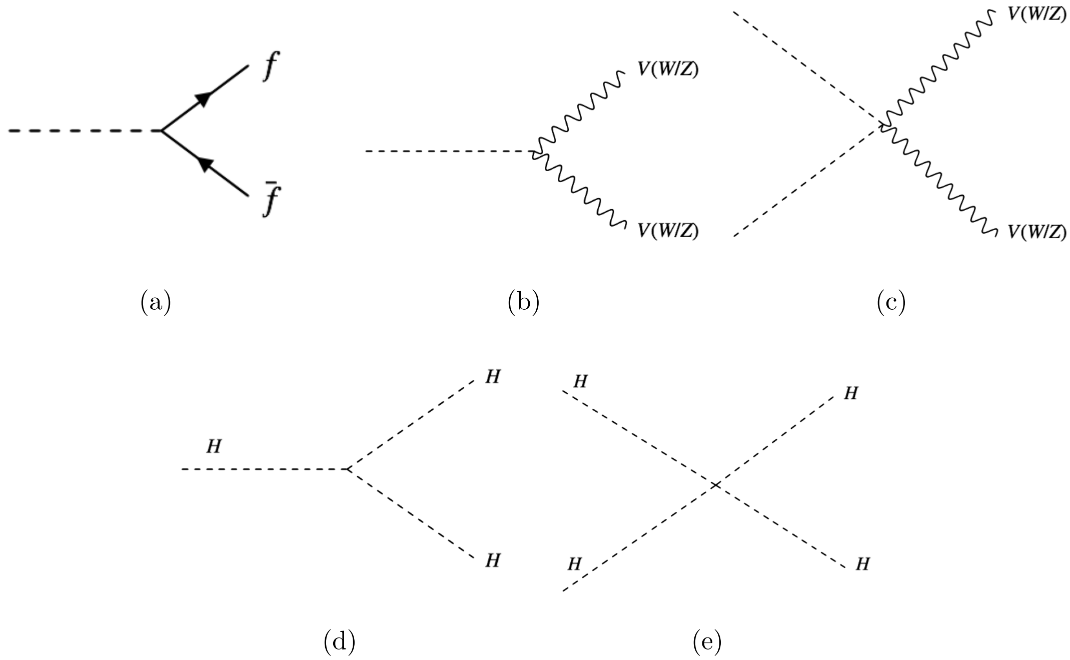

Figure 2.5. The Feynman diagrams of dominant Higgs decay.

The Higgs boson coupling to gluons is induced at leading order by a one-loop graph in which H couples to a virtual $t\bar{t}$ pair. Figure 2.6 shows the Feyman diagrams of the Higgs production mechanisms.

The Feyman diagrams of the Higgs boson decaying to gluons is shown on Figure 2.7.

Likewise, the Higgs boson coupling to photons is also generated via loops, although in this case the one-loop graph with a virtual W^+W^- pair provides the dominant contribution and the one involving a virtual $t\bar{t}$ pair is subdominant. [33] The Feynman diagrams of the Higgs boson decays to photons is shown on Figure 2.8.

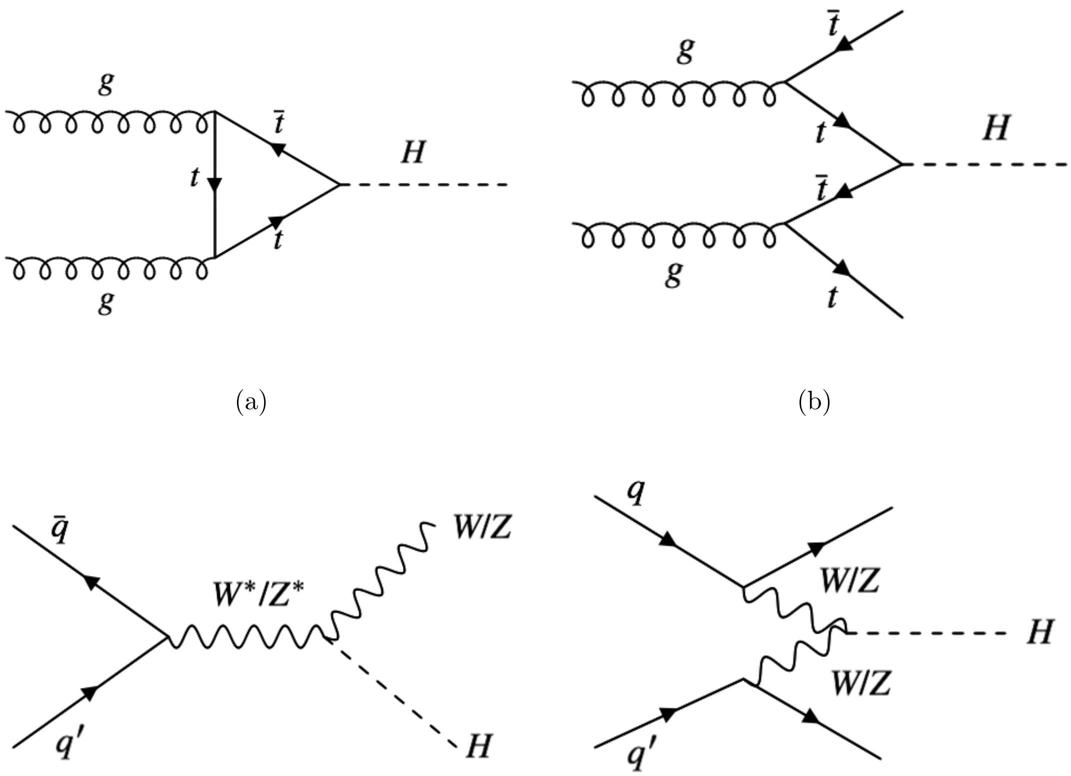

(a) (b) (c) (d)

Figure 2.6. The Feynman diagrams of Higgs production.

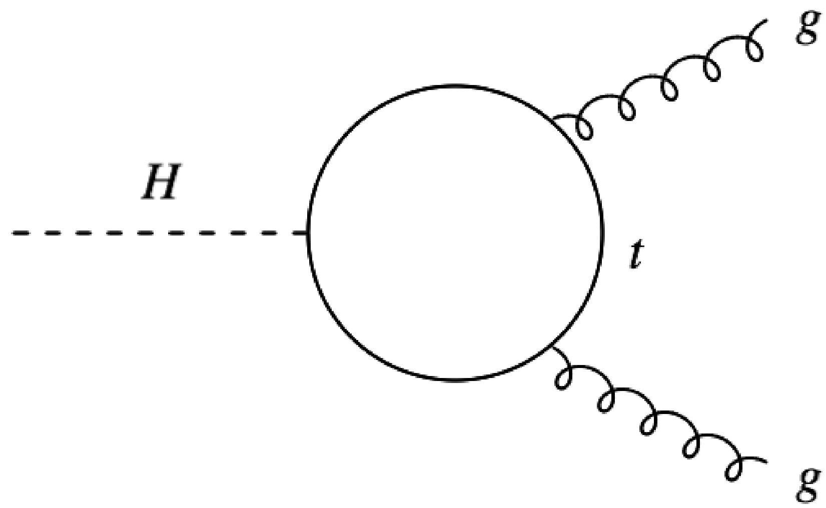

Figure 2.7. The Feynman diagrams of Higgs decaying to gluons.

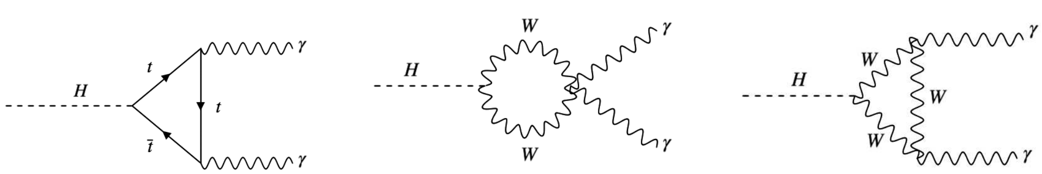

(a) (b) (c)

Figure 2.8. The Feynman diagrams of Higgs to photons decay.

2.5. Higgs production and decay mechnisms

Reviews of the SM Higgs boson's properties and phenomenology, with an emphasis on the impact of loop corrections to the Higgs boson decay rates and cross sections, can be found in [44, 57, 21, 37].

2.5.1. Production mechanisms at hadron colliders

The main production mechanisms at the Tevatron and the LHC are gluon fusion, weak-boson fusion, associated production with a gauge boson and associated production with top quarks. Figure 2.6 depicts representative diagrams for these dominant Higgs production processes.

The cross sections for the production of a SM Higgs boson as a function of $\sqrt{s}$, the center of mass energy, for pp collisions, including bands indicating the theoretical uncertainties, are summarized in Figure 2.9. A detailed discussion, including uncertainties in the theoretical calculations due to missing higher order effects and experimental uncertainties on the determination of SM parameters involved in the calculations can be found in Ref. [31].

These references also contain state-of-the-art discussions on the impact of theoretical uncertainties.

Table 2.5.1 summarizes the Higgs boson production cross sections and relative uncertainties for a Higgs mass of 125 GeV, for $\sqrt{s} = 7$, 8 and 14 TeV.

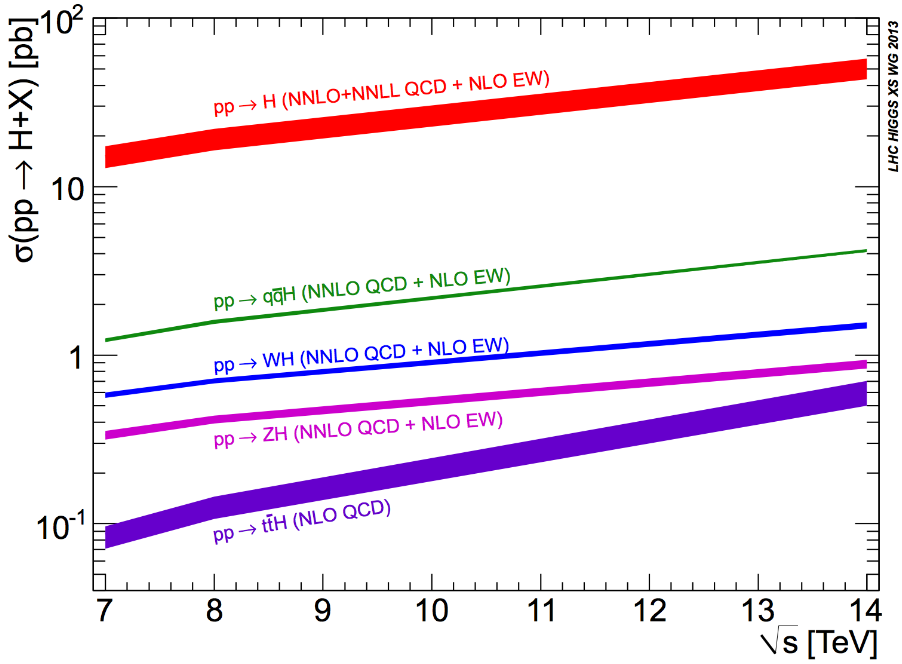

Figure 2.9. The SM Higgs boson production cross sections as a function of the center of mass energy, $\sqrt{s}$, for pp collisions.[32]

Table 2.1. Production cross section (in pb) for $m_H = 125$ GeV [32]

$\sqrt{s}$(TeV)	ggF	VBF	WH	ZH	$t\bar{t}H$	Total
7	15.1 $^{+17\%}_{-17\%}$	1.22 $^{+3\%}_{-2\%}$	0.58 $^{+4\%}_{-4\%}$	0.33 $^{+6\%}_{-6\%}$	0.009 $^{+12\%}_{-18\%}$	17.4
8	19.3 $^{+15\%}_{-15\%}$	1.58 $^{+3\%}_{-2\%}$	0.70 $^{+4\%}_{-5\%}$	0.41 $^{+6\%}_{-6\%}$	0.13 $^{+12\%}_{-18\%}$	22.1
14	49.8 $^{+20\%}_{-15\%}$	4.18 $^{+3\%}_{-3\%}$	1.50 $^{+4\%}_{-4\%}$	0.88 $^{+6\%}_{-5\%}$	0.61 $^{+15\%}_{-28\%}$	57.0

Chapter 3

Introduction of ATLAS detector

In this chapter I will introduce the Large Hadron Collider (LHC) and the ATLAS detector with emphasis on systems essential to this work, especially the calorimeter and muon system, as well as the tracking system and the trigger.

3.1. Large Hadron Collider (LHC)

The LHC is the world's largest and most powerful particle collider, built at the European Organization for Nuclear Research (CERN) from 1998 to 2008. It was built in collaboration with over 10,000 scientists and engineers from over 100 countries, as well as hundreds of universities and laboratories. It lies in a tunnel 27 kilometres (17 miles) in circumference, as deep as 175 metres (574 ft) beneath the France-Switzerland border near Geneva, Switzerland.

As of 2015, the LHC remains one of the largest and most complex experimental facilities ever built. Its synchrotron is designed to collide two opposing particle beams of either protons at up to 7 TeV or ions with energies up to 2.76 TeV. It operated at 3.5 TeV per beam in 2011, 4 TeV per beam in 2012, and will operate at 6.5 TeV per beam in 2015.

The aim of the LHC is to allow physicists to test the predictions of different theories of particle physics and high-energy physics, and access the existence of the predicted SM Higgs boson. It also supports a diversity of other physics programs, including direct and indirect tests of theories beyond the SM. The energy reach of the LHC allows physicists to try to address some of the unanswered questions meantioned in Section 2.2.3. It contains seven detectors, each designed for certain kinds of research.

Two of the detectors, A Toroidal LHC Apparatus (ATLAS) and the Compact Muon Solenoid (CMS), are large, general-purpose particle detectors. A Large Ion Collider Experiment (ALICE) and LHC-beauty (LHCb) have more specific roles with narrower programs. Three other experiments - Total Cross Section Elastic Scattering and Diffraction Dissociation (TOTEM), Monopole and Exotics Detector At the LHC (MoEDAL) and LHC-forward (LHCf) - are very much smaller and are for even more specialized research.

My thesis work uses the ATLAS detector to measure the main properties of the new boson discovered in 2012, so this chapter presents a comprehensive overview of the ATLAS detector.

3.2. ATLAS detector

ATLAS is 46 metres long, 25 metres in diameter, and weighs about 7,000 tonnes; it contains some 3000 km of cable. The overall layout is shown in Figure 3.1.

It is intended to investigate many different types of physics that might become detectable at the energies achievable at the LHC. Some of these are confirmations or improved measurements of the Standard Model, while many others are possible clues for new physical theories. These and other diverse physics programs require ATLAS to achieve precision in charged particle tracking and energy measurement, neutral particle electromagnetic and strong interactions, and missing energy resonstruction(as due to neutrinos). One of the most important goals of ATLAS was to investigate a missing piece of the Standard Model, the Higgs boson, which has been discoveried and measured by ATLAS and CMS.

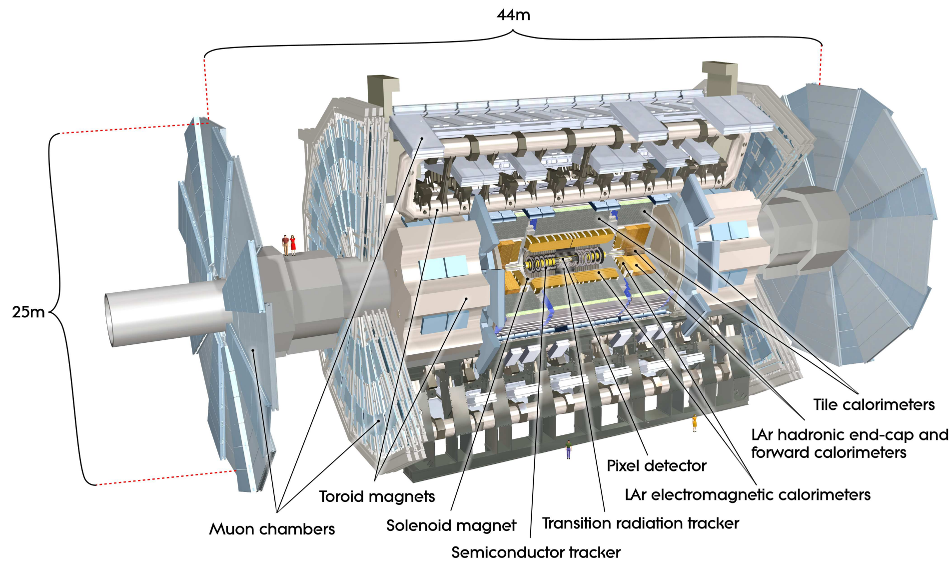

Figure 3.1. Cut-away view of the ATLAS detector

The ATLAS detector includes an inner tracking detector, calorimetry and muon spectrometer to detect particles. The Trigger and Data Acquisition (collectively TDAQ) systems, the timing- and trigger-control logic, and the Detector System (DCS) are partitioned into sub-systems, typically associated with sub-detectors (e.g. just the Liquid Argon Calorimeter, etc.), which have the same logical components and building blocks.

Due to the instability of new, heavy particles, it is expected that if produced they will decay down to lighter and lighter particles, ending with very stable particles that can be detected by a large, macroscopic detector. This places requirements on ATLAS to be able to detect, and possibly identify, electrons, photons, and protons (the most stable light particles). In addition, some unstable particles are long-lived enough to traverse some or all of ATLAS. These include muons, pions (neutral and charged), and kaons. Charged particles, such as electrons and charged pions, lose energy by ionization and in doing so leave tracks in material. Neutral particles do not ionize, but can be stopped and forced to deposit some of all of their energy in a dense calorimeter system. These basic ideas inform the principle detector designs in ATLAS, described in the following sections.

3.2.1. Tracking System

Approximately 1000 particles will emerge from the collision point every 25 ns within $|\eta| < 2.5$, creating a very large charged particle density in the detector. Charged particles leave traces of their flight trajectories in detector material; these traces are called "tracks" and are the primary means by which we detect the passage of such particles. To achieve the momentum and vertex resolution requirements imposed by the benchmark physics processes, high-precision measurements must be made with fine detector granularity. Pixel and silicon microstrip (SCT) trackers, used in conjunction with the straw tubes of the Transition Radiation Tracker (TRT), offer these features.

The layout of the Inner Detector (ID) is illustrated in Figure 3.2. Its basic parameters are summarised in Table 3.2.1.

The inner detector system provides tracking measurements in a range matched by the precision measurements of the electromagnetic calorimeter. The electron identification capabilities are enhanced by the detection of transition-radiation photons in the xenon-based gas mixture of the straw tubes. The semiconductor trackers also allow impact parameter (the distance of closest approach to the primary vertex) measurements and vertexing for heavy-flavour (e.g. B hadron vertex reconstruction) and τ-lepton tagging (the algorithms for identification of τ-jets). The secondary vertex measurement performance is enhanced by the innermost layer of pixels, at a radius of about 5 cm.

Table 3.1. Main parameters of the inner-detector system

Item		**Radial extension (mm)**	**Length (mm)**
Overall ID envelope		$0 < R < 1150$	$0 < \|z\| < 3512$
Beam-pipe		$29 < R < 36$	
Pixel	Overall envelope	$45.5 < R < 242$	$0 < \|z\| < 3092$
3 cylindrical layers	Sensitive barrel	$505 < R < 122.5$	$0 < \|z\| < 400.5$
2×3 disks	Sensitive end-cap	$88.8 < R < 149.6$	$495 < \|z\| < 650$
SCT	Overall envelopte	$255 < R < 549$(barrel)	$0 < \|z\| < 805$
		$251 < R < 610$(end-cap)	$810 < \|z\| < 2797$
4 cylindrical layers	Sensitive barrel	$299 < R < 514$	$0 < \|z\| < 749$
2×9 disks	Sensitive end-cap	$275 < R < 560$	$839 < \|z\| < 2735$
TRT	Overrall envelopt	$554 < R < 1082$(bareel)	$0 < \|z\| < 780$
		$617 < R < 1106$(end-cap)	$827 < \|z\| < 2744$
73 straw planes	Sensitive barrel	$563 < R < 1066$	$0 < \|z\| < 712$
160 straw planes	Sensitive end-cap	$644 < R < 1004$	$848 < \|z\| < 2710$

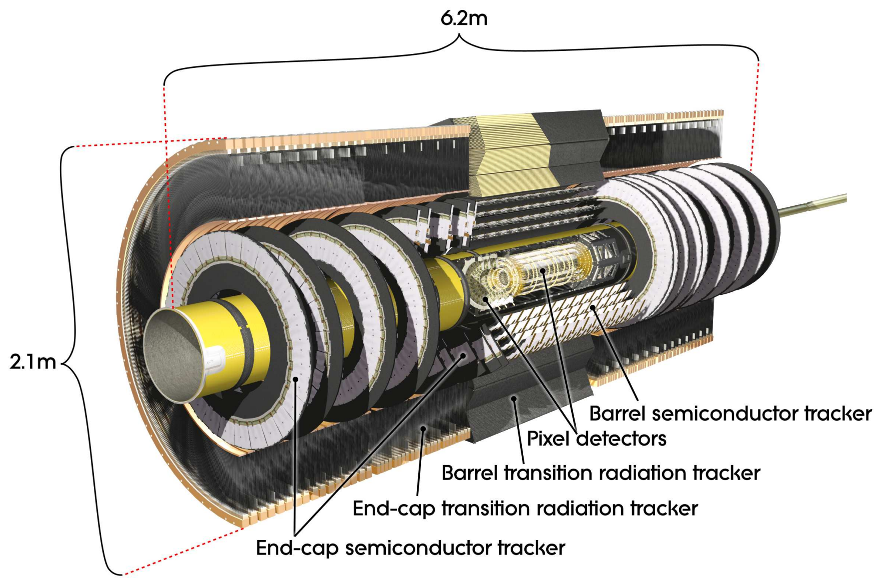

Figure 3.2. Cut-away view of the ATLAS inner detector

3.2.2. Muon Spectrometer

The conceptual layout of the muon spectrometer is shown in Figure 3.3 and the main parameters of the muon chambers are listed in Table 3.2.

It is based on the magnetic deflection of muon tracks in the large superconducting air-core toroid magnets, instrumented with a separate trigger and high-precision tracking chambers. Over the range $|\eta| < 1.4$, magnetic bending is provided by the large barrel toroid. For $1.6 < |\eta| < 2.7$, muon tracks are bent by two smaller end-cap magnets inserted into both ends of the barrel toroid. Over $1.4 < |\eta| < 1.6$, usually referred to as the "transition region", magnetic deflection is provided by a combination of barrel and end-cap fields. This magnet configuration provides a field which is mostly orthogonal to the muon trajectories, while minimising the degradation of resolution due to multiple scattering. The anticipated high level of particle flux has had a

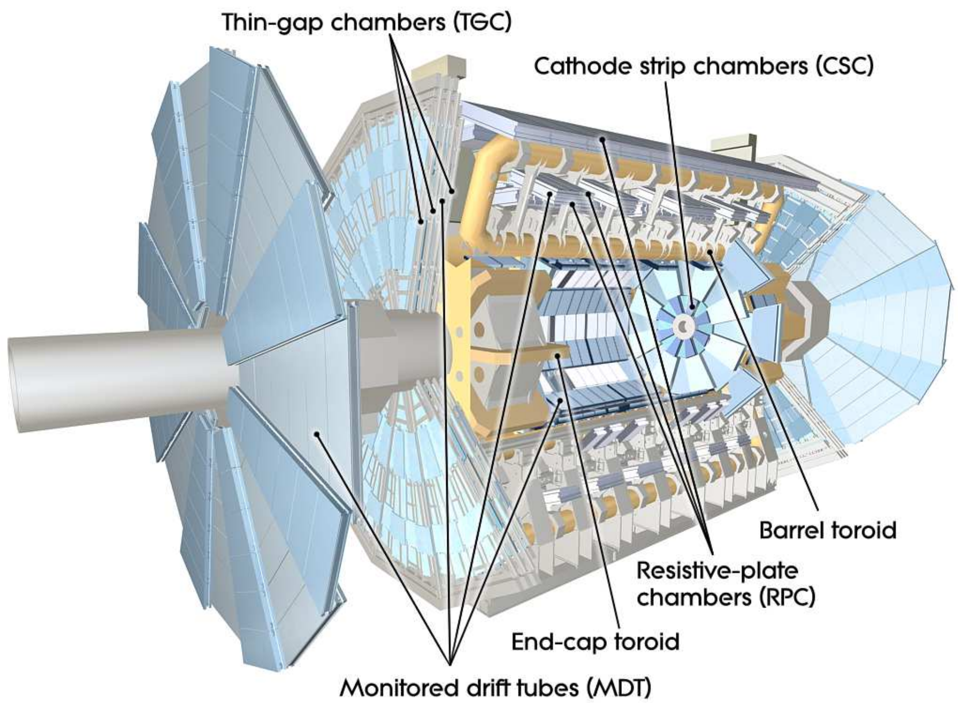

Figure 3.3. Cut-away view of the ATLAS muon system

Table 3.2. Main parameters of the muon spectrometer. Numbers in brackets for the MDTs and the RPCs refer to the final configuration of the detector in 2009

Monitored drift tubes	**MDT**
-Coverage	$\|\eta\| < 2.7$ (innermost layer: $\|\eta\| < 2.0$)
-Number of chambers	1088(1150)
-Number of channels	339000(354000)
-Function	Precision tracking
Cathode strip chambers	**CSC**
-Coverage	$2.0 < \|\eta\| < 2.7$
-Number of chambers	32
-Number of channels	31000
-Function	Precision tracking
Resistive plate chambers	**RPC**
-Coverage	$\|\eta\| < 1.05$
-Number of chambers	544(606)
-Number of channels	359000(373000)
-Function	Triggering, second coordinate
Thin gap chambers	**TGC**
-Coverage	$1.05 < \|\eta\| < 2.7$ (2.4 for triggering)
-Number of chambers	3588
-Number of channels	318000
-Function	Triggering, second coordinate

major impact on the choice and design of the spectrometer instrumentation, affecting performance parameters such as rate capability, granularity, ageing properties, and radiation hardness.

In the barrel region, tracks are measured in chambers arranged in three cylindrical layers around the beam axis; in the transition and end-cap regions, the chambers are installed in planes perpendicular to the beam, also in three layers.

3.2.2.1. The toroid magnets

A system of three large air-core toroids generates the magnetic field for the muon spectrometer. The two end-cap toroids are inserted in the barrel toroid at each end and line up with the central solenoid. Each of the three toroids consists of eight coils assembled radially and symmetrically around the beam axis. The end-cap toroid coil system is rotated by 22.5 degrees with respect to the barrel toroid coil system in order to provide radial overlap and to optimise the bending power at the interface between the two coil systems.

The barrel toroid coils are housed in eight individual cryostats, with the linking elements between them providing the overall mechanical stability. The structures of the barrel are shown in Figure 3.4 (a). Each end-cap toroid consists of eight racetrack-like coils in an aluminium alloy housing. Each coil has two double-pancake type windings. Its structures are shown in Figure 3.4 (b). They are cold-linked and assembled as a single cold mass, housed in one large cryostat. Therefore the internal forces in the end-cap toroids are taken by the cold supporting structure between the coils, a different design solution than in the barrel toroid.

The performance in terms of bending power is characterised by the field integral $\int \mathrm{B}\,\mathrm{d}l$, where B is the field component normal to the muon direction and the integral is computed along an infinite-momentum muon trajectory, between the innermost and outermost muon-chamber planes. The barrel toroid provides 1.5 to 5.5 $\mathrm{T \cdot m}$ of

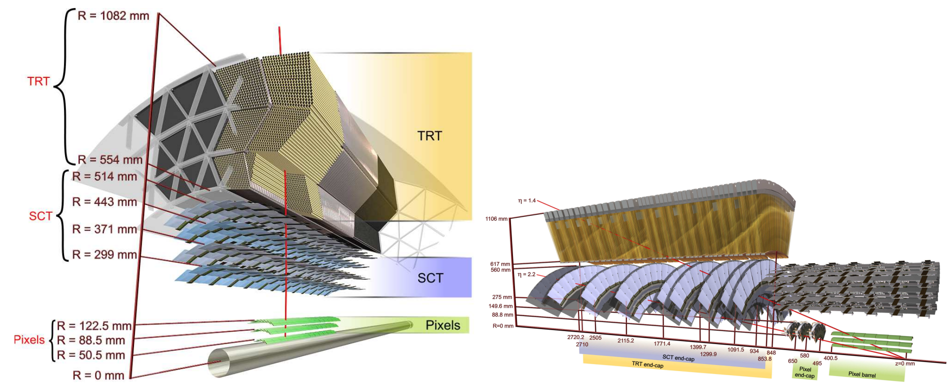

(a) (b)

Figure 3.4. Diagrams illustrating the sensors and structural elements in (a) the barrel and (b) end-cap of the ID

bending power in the pseudorapidity range $0 < |\eta| < 1.4$, and the end-cap toroids approximately 1 to 7.5 $\mathrm{T \cdot m}$ in the region $1.6 < |\eta| < 2.7$. The bending power is lower in the transition regions where the two magnets overlap ($1.4 < |\eta| < 1.6$).

3.2.2.2. Muon chamber types

Over most of the η-range, a precision measurement of the track coordinates in the principal bending direction of the magnetic field is provided by Monitored Drift Tubes (MDTs). The mechanical isolation in the drift tubes of each sense wire from its neighbours guarantees a robust and reliable operation. At large pseudorapidities, Cathode Strip Chambers (CSCs, which are multi-wire proportional chambers[1] with cathodes segmented into strips) with higher granularity are used in the innermost plane over $2 < |\eta| < 2.7$, to withstand the demanding rate and background conditions.

[1] A "multi-wire proportional chamber" is a type of proportional counter that detects charged particles and photons and can give positional information on their trajectory, by tracking the trails of gaseous ionization.

The stringent requirements on the relative alignment of the muon chamber layers are met by the combination of precision mechanical-assembly techniques and optical alignment systems both within and between muon chambers. The trigger system covers the pseudorapidity range $|\eta| < 2.4$.

Resistive Plate Chambers [2] are used in the barrel and Thin Gap Chambers (TGCs, which whole system is surrounded with sniffers at various heights for the detection of flammable mixtures.) in the end-cap regions. The trigger chambers for the muon spectrometer serve a threefold purpose: provide bunch-crossing identification, provide well-defined p_T thresholds, and measure the muon coordinate in the direction orthogonal to that determined by the precision-tracking chambers.

3.2.3. Calorimetry

A view of the sampling calorimeters is presented in Figure 3.5, and the pseudorapidity coverage, granularity, and segmentation in depth of the calorimeters are summarised in Table 3.3.

These calorimeters cover the range $|\eta| < 4.9$, using different techniques suited to the widely varying requirements of the physics processes of interest and of the radiation environment over this large η-range. Over the η region matched to the inner detector, the fine granularity of the EM calorimeter is ideally suited for precision measurements of electrons and photons. The coarser granularity of the rest of the calorimeter is sufficient to satisfy the physics requirements for E_{T} reconstruction and E_T^{miss} measurements.

Calorimeters must provide good containment for electromagnetic and hadronic showers, and must also limit punch-through into the muon system. Hence, calorimeter

[2] RPCs are gaseous detectors and their operation is based on the detection of the gas ionization produced by charged particles when traversing the active area of the detector, under a strong uniform electric field applied by resistive electrodes.

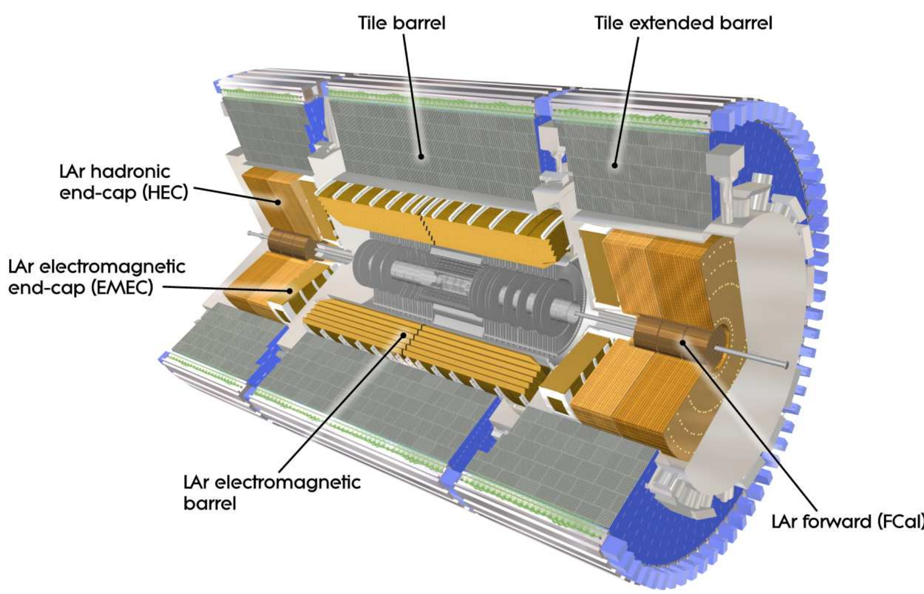

Figure 3.5. Cut-away view of the ATLAS calorimeter detector

Table 3.3. Main parameters of the calorimeter system

	Barrel		**End-cap**	
EM calorimeter				
Number of layers and $\|\eta\|$ coverage				
Presampler	1	$\|\eta\| < 1.52$	1	$1.5 < \|\eta\| < 1.8$
Calorimeter	3	$\|\eta\| < 1.35$	2	$1.375 < \|\eta\| < 1.5$
	2	$1.35 < \|\eta\| < 1.475$	3	$1.5 < \|\eta\| < 2.5$
			2	$2.5 < \|\eta\| < 3.2$
Granularity $delta\eta \times \delta\phi$ versus $\|\eta\|$				
Presampler	0.025×0.1	$\|\eta\| < 1.52$	0.025×0.1	$1.5 < \|\eta\| < 1.8$
Calorimeter 1st layer	$0.025/8 \times 0.1$	$\|\eta\| < 1.40$	0.050×0.1	$1.375 < \|\eta\| < 1.425$
	0.025×0.025	$1.40 < \|\eta\| < 1.475$	0.025×0.1	$1.425 < \|\eta\| < 1.5$
			$0.025/8 \times 0.1$	$1.5 < \|\eta\| < 1.8$
			$0.025/6 \times 0.1$	$1.8 < \|\eta\| < 2.0$
			$0.025/4 \times 0.1$	$2.0 < \|\eta\| < 2.4$
			0.025×0.1	$2.4 < \|\eta\| < 2.5$
			0.1×0.1	$2.5 < \|\eta\| < 3.2$
Calorimeter 2nd layer	0.025×0.025	$\|\eta\| < 1.40$	0.050×0.025	$1.375 < \|\eta\| < 1.425$
	0.075×0.025	$1.40 < \|\eta\| < 1.475$	0.25×0.025	$1.425 < \|\eta\| < 2.5$
			0.1×0.1	$2.5 < \|\eta\| < 3.2$
Calorimeter 3rd layer	0.050×0.025	$\|\eta\| < 1.35$	0.050×0.025	$1.5 < \|\eta\| < 2.5$
Number of readout channels				
Presampler	7808		1536 (both sides)	
Calorimeter	101760		62208 (both sides)	
LAr hadronic end-cap				
$\|\eta\|$ coverage			$1.5 < \|\eta\| < 3.2$	
Number of layers			4	
Granularity $\delta\eta \times \delta\phi$			0.1×0.1	$1.5 < \|\eta\| < 2.5$
			0.2×0.2	$2.5 < \|\eta\| < 3.2$
Readout channels			5632 (both sides)	
LAr forward calorimeter				
$\|\eta\|$ coverage			$3.1 < \|\eta\| < 4.9$	
Number oflayers			3	
Granularity $\delta x \times \delta y$(cm)			FCal1: 3.0×2.6	$3.15 < \|\eta\| < 4.30$
			FCal1: $\sim$ four times finer	$3.10 < \|\eta\| < 3.15$
				$4.30 < \|\eta\| < 4.83$
			FCal2: 3.3×4.2	$3.24 < \|\eta\| < 4.50$
			FCal2: $\sim$ four times finer	$3.20 < \|\eta\| < 3.24$
				$4.50 < \|\eta\| < 4.81$
			FCal3: 5.4×4.7	$3.32 < \|\eta\| < 4.60$
			FCal3: $\sim$ four times finer	$3.39 < \|\eta\| < 3.32$
				$4.60 < \|\eta\| < 4.75$
Readout channels			3524 (both sides)	
Scintillator tile calorimeter				
$\|\eta\|$ coverage	$\|\eta\| < 1.0$		$0.8 < \|\eta\| < 1.7$	
Number of layers	3		3	
Granularity $\delta\eta \times \delta\phi$	0.1×0.1		0.1×0.1	
Last layer	0.2×0.1		0.2×0.1	
Readout channels	5760		4092 (both sides)	

depth is an important design consideration. The total thickness of the EM calorimeter is > 22 radiation lengths (X_0) in the barrel and > 24 X_0 in the end-caps. The approximate 9.7 interaction lengths (λ) of active calorimeter in the barrel (10 λ in the end-caps) are adequate to provide good resolution for high-energy jets. The total thickness, including 1.3 λ from the outer support, is 11 λ at $\eta = 0$ and has been shown both by measurements and simulations to be sufficient to reduce punch-through well below the irreducible level of prompt or decay muons. Together with the large η-coverage, this thickness will also ensure a good E_T^{miss} measurement, which is important for many physics signatures and in particular for SUSY particle searches.

3.2.3.1. Liquid Argon (LAr) electromagnetic Calorimeter

The EM calorimeter is divided into a barrel part ($|\eta| < 1.475$) and two end-cap components ($1.375 < |\eta| < 3.2$), each housed in their own cryostat. The position of the central solenoid in front of the EM calorimeter demands optimisation of the material in order to achieve the desired calorimeter performance. As a consequence, the central solenoid and the LAr calorimeter share a common vacuum vessel, thereby eliminating two vacuum walls. The barrel calorimeter consists of two identical half-barrels, separated by a small gap (4 mm) at $\mathcal{Z} = 0$. Each end-cap calorimeter is mechanically divided into two coaxial wheels: an outer wheel covering the region $1.375 < |\eta| < 2.5$, and an inner wheel covering the region $2.5 < |\eta| < 3.2$. The EM calorimeter is a lead-LAr detector with accordion-shaped kapton electrodes and lead absorber plates over its full coverage. The accordion geometry provides complete ϕ symmetry without azimuthal cracks. The lead thickness in the absorber plates has been optimised as a function of η in terms of EM calorimeter performance in energy resolution. Over the region devoted to precision physics ($|\eta| < 2.5$), the EM calorimeter is segmented in three sections in depth. For the end-cap inner wheel, the calorimeter is segmented in two sections in depth and has a coarser lateral granularity than for the rest of the acceptance.

In the region of $|\eta| < 1.8$, a presampler detector is used to correct for the energy lost by electrons and photons upstream of the calorimeter. The presampler consists of an active LAr layer of thickness 1.1 cm (0.5 cm) in the barrel (end-cap) region.

3.2.3.2. Hadron Calorimeter

Tile calorimeter. The tile calorimeter is placed directly outside the EM calorimeter envelope. Its barrel covers the region $|\eta| < 1.0$, and its two extended barrels the range $0.8 < |\eta| < 1.7$. It is a sampling calorimeter using steel as the absorber and scintillating tiles as the active material. The barrel and extended barrels are divided azimuthally into 64 modules. Radially, the tile calorimeter extends from an inner radius of 2.28 m to an outer radius of 4.25 m. It is segmented in depth in three layers, approximately 1.5, 4.1 and 1.8 interaction lengths (λ) thick for the barrel and 1.5, 2.6, and 3.3 λ for the extended barrel. The total detector thickness at the outer edge of the tile-instrumented region is 9.7 λ at $\eta = 0$ Two sides of the scintillating tiles are read out by wavelength-shifting fibers into two separate photomultiplier tubes. In η, the readout cells built by grouping fibers into the photomultipliers are pseudo-projective towards the interaction region.

LAr hadronic end-cap calorimeter. The Hadronic End-cap Calorimeter (HEC) consists of two independent wheels per end-cap, located directly behind the end-cap electromagnetic calorimeter and sharing the same LAr cryostats. To reduce the drop in material density at the transition between the end-cap and the forward calorimeter (around $|\eta| = 3.1$, the HEC extends out to $|\eta| = 3.2$, thereby overlapping with the forward calorimeter. Similarly, the HEC η range also slightly overlaps that of the tile calorimeter ($|\eta| < 1.7$) by extending to $|\eta| = 1.5$. Each wheel is built from 32 identical wedge-shaped modules, assembled with fixtures at the periphery and at the central bore. Each wheel is divided into two segments in depth, for a total of four layers per end-cap. The wheels closest to the interaction point are built from 25 mm parallel copper plates, while those further away use 50 mm copper plates (for all wheels the first plate is half-thickness). The outer radius of the copper plates is 2.03 m, while the inner radius is 0.475 m (except in the overlap region with the forward calorimeter where this radius becomes 0.372 m). The copper plates are interleaved with 8.5 mm LAr gaps, providing the active medium for this sampling calorimeter.

LAr forward calorimeter. The Forward Calorimeter (FCal) is integrated into the end-cap cryostats, as this provides clear benefits in terms of uniformity of the calorimetric coverage as well as reduced radiation background levels in the muon spectrometer. In order to reduce the amount of neutron albedo (which includes neutrons that are created by interactions of the primary radiation field in the surface or atmosphere and backscatter in directions opposite to the direction of the incoming, primary radiation.) in the inner detector cavity, the front face of the FCal is recessed by about 1.2 m with respect to the EM calorimeter front face. This severely limits the depth of the calorimeter and therefore calls for a high-density design. The FCal is approximately 10 interaction lengths deep, and consists of three modules in each end-cap: the first, made of copper, is optimised for electromagnetic measurements, while the other two, made of tungsten, measure predominantly the energy of hadronic interactions. Each module consists of a metal matrix, with regularly spaced longitudinal channels filled with the electrode structure consisting of concentric rods and tubes parallel to the beam axis. The LAr in the gap between the rod and the tube is the sensitive medium. This geometry allows for excellent control of the gaps, which are as small as 0.25 mm in the first section, in order to avoid problems due to ion buildup.

3.2.4. Forward detectors

Three smaller detector systems cover the ATLAS forward region. The main function of the first two systems is to determine the luminosity delivered to ATLAS. At 17 m from the interaction point lies LUCID (LUminosity measurement using Cerenkov Integrating Detector). It detects inelastic $p-p$ scattering in the forward direction, and is the main online relative-luminosity monitor for ATLAS. The second detector is ALFA (Absolute Luminosity For ATLAS). Located at 240 m, it consists of scintillating fiber trackers located inside Roman pots[3] which are designed to approach as close as 1 mm to the beam. The third system is the Zero-Degree Calorimeter (ZDC), which plays a key role in determining the centrality of heavy-ion collisions. It is located at 140 m from the interaction point, just beyond the point where the common straight-section vacuum-pipe divides back into two independent beam-pipes. The ZDC modules consist of layers of alternating quartz rods and tungsten plates which measure neutral particles at pseudorapidities $|\eta| \geq 8.2$.

3.2.5. Trigger System

The trigger system has three distinct levels: Level 1 (L1), Level 2 (L2), and the event filter. Each trigger level refines the decisions made at the previous level and, where necessary, applies additional selection criteria. The data acquisition system receives and buffers the event data from the detector-specific readout electronics, at the L1 trigger accept rate, over 1600 point-to-point readout links. The first level uses a limited amount of the total detector information to make a decision in less than 2.5μs, reducing the rate to about 75 kHz while the final recording rate, in proton-proton collisions, of approximately 300 Hz. The two higher levels access more detector information for a final rate of up to 200 Hz with an event size of approximately 1.3 Mbyte.

[3] "Roman pot" is an important tool to measure the total cross section of two particle beams in a collider, named after its implementation by the CERN Rome group in the early 1970s.

The L1 trigger searches for high transverse-momentum muons, electrons, photons, jets, and τ-leptons decaying into hadrons, as well as large missing and total transverse energy. Its selection is based on information from a subset of detectors. High transverse-momentum muons are identified using trigger chambers in the barrel and end-cap regions of the muon spectrometer. Calorimeter selections are based on reduced-granularity information from all the calorimeters. Results from the L1 muon and calorimeter triggers are processed by the central trigger processor, which implements a trigger 'menu' made up of combinations of trigger selections. Pre-scaling (accepting only every Nth trigger) of trigger menu items is also available, allowing optimal use of the bandwidth as luminosity and background conditions change. Events passing the L1 trigger selection are transferred to the next stages of the detector-specific electronics and subsequently to the data acquisition via point-to-point links. In each event, the L1 trigger also defines one or more Regions-of-Interest (RoIs), i.e. the geographical coordinates in η and ϕ, of those regions within the detector where its selection process has identified interesting features, such as a large energy deposit. The RoI data include information on the type of feature identified and the criteria passed, e.g. a minumum threshold. This information is subsequently used by the high-level trigger.

The L2 selection is seeded by the RoI information provided by the L1 trigger over a dedicated data path. L2 selections use, at full granularity and precision, all the available detector data within the RoIs (approximately 2% of the total event data). The L2 menus[4] are designed to reduce the trigger rate to approximately 3.5 kHz, with an event processing time of about 40 ms, averaged over all events. The final stage of the event selection is carried out by the event filter, which reduces the event rate to

[4]a "menu" is a set of selection criteria designed to identify interesting physics processes.

roughly 200 Hz. Its selections are implemented using those similar to offline[5] analysis procedures within an average event processing time of the order of four seconds.

My work was to designed and built on-line trigger rates prediction system for shifters and experts. I Worked with TDAQ and trigger groups to use the existing data of trigger rates (both L1 and HLT triggers) to derive formulas to calculate trigger rates from luminosities and cross sections; and to use these formulas to predict trigger rates with current luminosity and cross section, compare the predicted rates with the current trigger rates to check if the current rates are reasonable. This system alerted shifters and experts when the trigger rates became abnormal or were projected to go too high.

3.3. Magnet system

ATLAS features a unique hybrid system of four large superconducting magnets. This magnetic system is 22 m in diameter and 26 m in length, with a stored energy of 1.6 GJ. The system required approximately 15 years of design, construction in industry, and finally system integration and operation at CERN.

Figure 3.6 shows the general layout, the four main layers of detectors and the four superconducting magnets which provide the magnetic field over a volume of approximately 12,000 m^3 (defined as the region in which the field exceeds 50 mT). The ATLAS magnet system, whose main parameters are listed in Table 3.4, consists of:

• a **solenoid**, which is aligned on the beam axis and provides a 2 T axial magnetic field for the inner detector, while minimising the radiative thickness in front of the barrel electromagnetic calorimeter;

[5] "online" refers to algorithms that run in real-time to aid in data-taking, while "offline" refers to a possibly refined and expanded set of algorithms used to aid in the later analysis of data, which can take weeks or months.

• a **barrel toroid** and two **end-cap toroids**, which produce a toroidal magnetic field of approximately 0.5 T and 1 T for the muon detectors in the central and end-cap regions, respectively.

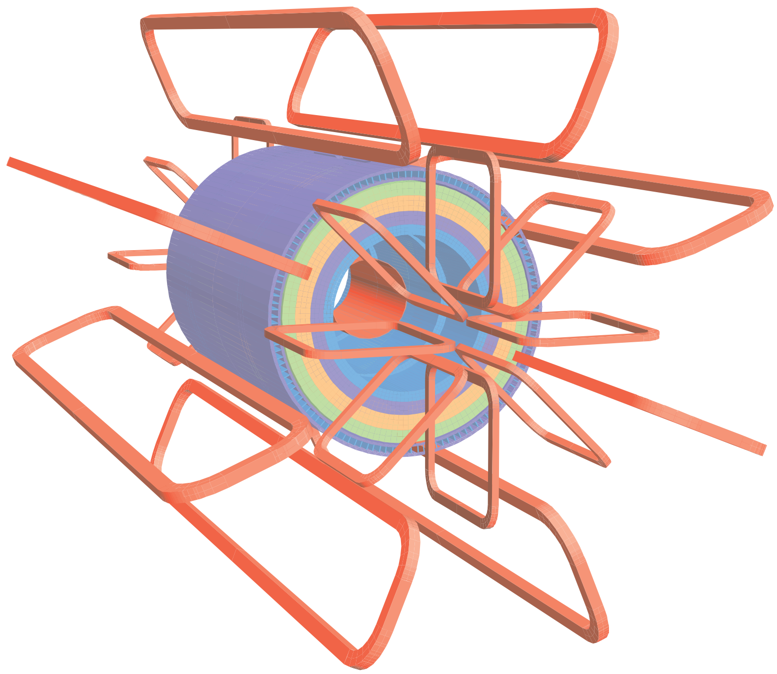

Figure 3.6. Geometry of magnet windings and tile calorimeter steel. The eight barrel toroid coils, with the end-cap coils interleaved are visible. The solenoid winding lies inside the calorimeter volume. The tile calorimeter is modelled by four layers with different magnetic properties, plus an outside return yoke. For the sake of clarity the forward shielding disk is not displayed

The main parameters of the magnet are listed in Table 3.4. The cylindrical volume surrounding the calorimeters and both end-cap toroids (see Figure 3.1) is filled by the magnetic field of the barrel toroid, which consists of eight coils encased in individual racetrack-shaped, stainless-steel vacuum vessels (see Figure 3.7). The coil assembly is supported by eight inner and eight outer rings of struts. The overall size of the

Table 3.4. Main parameters of the ATLAS magnet system

Property	Feature	Unit	Solenoid	Barrel toroid	End-cap toroids
Size	Inner diameter	m	2.46	9.4	1.65
	Outer diameter	m	2.56	20.1	10.7
	Axial length	m	5.8	25.3	5.0
	Number of coils		1	8	2×8
Mass	Conductor	t	3.8	118	2×20.5
	Cold mass	t	5.4	370	2×140
	Total assembly	t	5.7	830	2×239
Coils	Turns per coil		1154	120	116
	Nominal current	kA	7.73	20.5	20.5
	Magnet stored energy	GJ	0.04	1.08	2×0.25
	Peak field in the windings	T	2.6	3.9	4.1
	Field range in the bore	T	0.9-2.0	0.2-2.5	0.2-3.5
Conductor	Overall size Ratio Al:Cu:NbTi	mm^2	30×4.25 15.6:0.9:1	57×12 28:1.3:1	41×12 19:1.3:1
	Number of strands(NbTi)		12	38-40	40
	Strand diameter(NbTi)	mm	1.22	1.3	1.3
	Critical current (at 5 T and 4.2 K)	kA	20.4	58	60
	Operating/critical-current ratio at 4.5 K	%	20	30	30
	Residual resisivity ratio (RRR) for AI		> 500	> 800	> 800
	Temperature margin	K	2.7	1.9	1.9
	Number of units $\times$ length	m	4×2290	$8 \times 4 \times 1730$	$2 \times 8 \times 2 \times 800$
	Total length (produced)	km	10	56	2×13
Heat load	At 4.5 K	W	130	990	330
	At 60-80 K	kW	0.5	7.4	1.7
	Liquid helium mass flow	g/s	7	410	280

barrel toroid system as installed is 25.3 m in length, with inner and outer diameters of 9.4 m and 20.1 m, respectively.

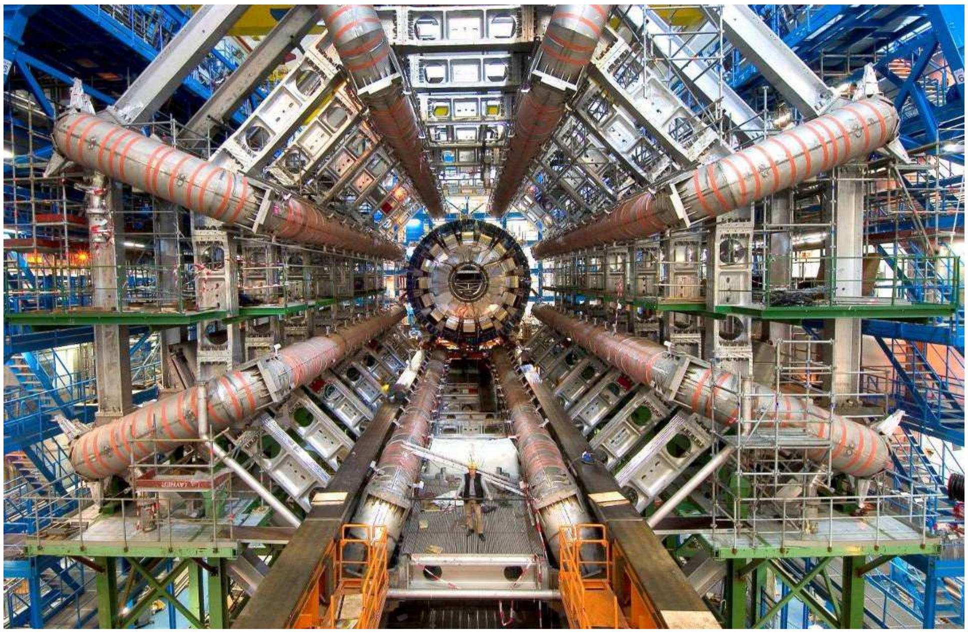

Figure 3.7. Barrel toroid as installed in the underground cavern; note the symmetry of the supporting structure. The temporary scaffolding and green platforms were removed once the installation was complete. The scale is indicated by the person standing in between the two bottom coils. Also visible are the stainless-steel rails carrying the barrel calorimeter with its embedded solenoid, which await translation towards their final position in the center of the detector.

The main parameters of the two end-cap toroids are listed in Table 3.4. These toroids generate the magnetic field required for optimising the bending power in the end-cap regions of the muon spectrometer system. They are supported by central rails, that also enable them to slide and facilitate the opening of the detector for access and maintenance.

3.4. Conclusions

The most salient systems required to faciliate the analysis in the remainder of this thesis are the tracking system, electromagnetic calorimeter, muon spectrometer, all associated magnets systems, and the trigger to select information for offline analysis. In the next chapter, I will describe how different types of particles are reconstructed and identified by the ATLAS detector systems and algorithms that combine information from those systems.

Chapter 4

Particle Selection

This chapter will introduce the objects detected in LHC by ATLAS detectors which are used in my analysis. Photons, electrons and muons and their reconstruction and identification, as well as important phenomena such as photon Final State Radiation (FSR) and bremsstrahlung will be covered.

The collisions at the LHC produce a broad spectrum of final-state muons, ranging from low-momentum non-isolated muons in b-jets to high-momentum isolated muons from W/Z-boson decays or from possible new physics. The experiment will detect and measure muons in the muon spectrometer and will also exploit the measurements in the inner detector and the calorimeters to improve the muon identification efficiency and momentum resolution. Muon measurements are a combination of detector responses in the muon spectrometer and in the inner detector.

Efficient and accurate reconstruction and identification of electrons and photons will be a task of unprecedented difficulty at the LHC, where the ratios of inclusive electrons and photons to jets from QCD processes are expected to be between one and two orders of magnitude worse than at the Tevatron (as an example, the electron-to-jet ratio is expected to be $\sim 10^{-5}$ at $p_T = 40$ GeV). In addition, the large amount of material in front of the electromagnetic calorimeters and the harsh operating conditions at the LHC design luminosity provide a difficult challenge in terms of preserving most of the electrons and photons with their energies and directions measured as well as would be expected from the intrinsic performance of the electromagnetic calorimeters measured in test-beams.

For the standard reconstruction of electrons and photons, a seed cluster is taken from the electromagnetic calorimeter and a loosely matching track is searched for among all reconstructed tracks. Additionally, the candidate is flagged if it matches a photon conversion reconstructed in the inner detector. Electron and photon candidates are thus separated reasonably cleanly, by requiring the electrons to have an associated track but no associated conversion. In contrast, the photons are defined as having no matched track, or as having been matched to a reconstructed conversion.

4.1. Muon Reconstuction and Identification

The muon detection system of the ATLAS detector is characterized by two high-precision tracking systems, namely the Inner Detector (ID) and the Muon Spectrometer (MS), plus a thick calorimeter that ensures safe hadron absorption filtering with high purity muons with energy above 3 GeV. Muon identification algorithms have been developed to combine the muon tracks reconstructed in the ID and the MS. The purpose of these algorithms is to associate segments and tracks found in the MS with the corresponding ID track and calorimeter information in order to identify muons at their production vertex with optimum parameter resolution.

4.1.1. Reconstruction and identification algorithms in ATLAS

Muon identification can be performed in four ways as shown in Figure 4.1: combined reconstruction, which matches and combines the MS tracks with ID tracks; standalone reconstruction with only MS track information; and "segment-tagged" or "calorimeter-tagged" reconstruction of ID tracks as muons performed with corresponding MS segment information or minimum ionizing signature in calorimeter.

Combined muons are defined in the range $|\eta| < 2.5$ that corresponds to the geometrical acceptance of the ID as discussed in Section 3.2.2 of Chapter 3. Tracks result

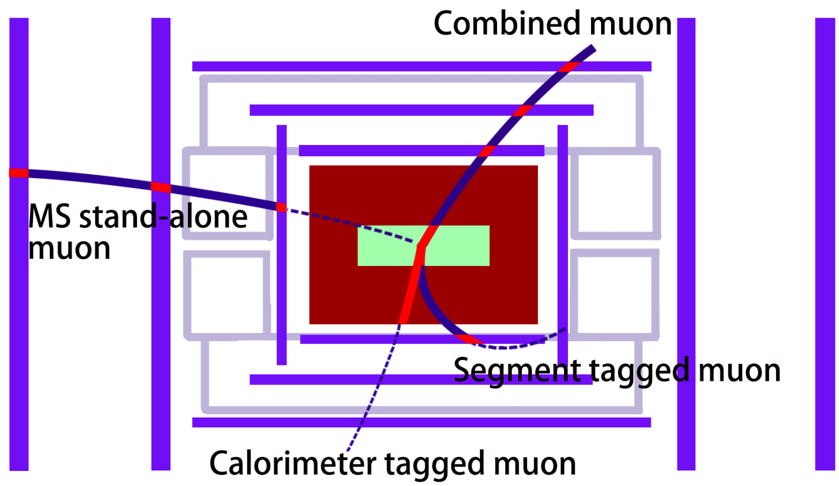

Figure 4.1. An illustration of the four types of muon reconstruction, emphasizing information from ATLAS subdetectors used for each type.

from the combination of the MS and ID measurements by a statistical combination or a refit of the entire track. Energy losses in the calorimeter are taken into account using parametrization and possibly calorimeter measurements. This reconstruction strategy provides the most precise measurement of the momentum and position of a muon. This is the most utilized type of muon reconstruction.

Standalone muons are defined in the range $|\eta| < 2.7$, which corresponds to the geometrical acceptance of the muon spectrometer. The track is entirely reconstructed in the MS and then extrapolated back to the beam line to determine the direction of flight and the impact parameter of the muon at the interaction point. The muon momentum measured in the MS is corrected for the parametrized energy loss of the muon in the calorimeter, to obtain the muon momentum at the interaction point. Most muon candidates of this type are in the range $2.5 < |\eta| < 2.7$, since the muon trajectory can be reconstructed in both the muon spectrometer and the inner detector in the range $|\eta| < 2.5$.

Segment-tagged muons are also restricted to $|\eta| < 2.5$ and mainly needed to identify muons with low transverse momentum, $p_T \lesssim 5$ GeV, because the deflection of these low-energy muons in the MS is so large that they do not cross two layers of muon chambers; that is the minimum required for an MS track. A track of a segment-tagged muon in the ID, extrapolated to the MS, is associated with straight track segments in the muon chambers. This provides efficiency recovery in the regions with low MS detector coverage.

The calorimeter-tagged muons are complementary to the ordinary three types of muons, important to cover the acceptance gap of the muon spectrometer at $|\eta| \sim 0$ required by services for the ID and the calorimeters. It identifies an ID track with an energy deposition in the calorimeters compatible with a minimum ionizing particle. This is used in place of ID tracks to reduce the background in the tag-and-probe method.

The current ATLAS baseline reconstruction includes two algorithms for each strategy, and each algorithm is grouped into a family. The output data intended for use in physics analysis includes two collections of muons - one for each family - in each processed event. We refer to the collections (and families) by the names of the corresponding combined algorithms: Staco [26] and Muid [45]. The Staco collection is the one used in the analysis described in this thesis. The algorithms grouped in these two families associated to all the four strategies are listed in Table 4.1.1 [26].

Each of the reconstruction methods can be individually used to reconstruct and identify muons for the analysis. We use the following algorithms from the Staco family on the $H \rightarrow ZZ^{*} \rightarrow \ell^{+}\ell^{-}\ell'^{+}\ell'^{-}$ channel: STACO for combined muons; MUONBOY for standalone muons; and MuTag for segment-tagged muons. CaloTag and CaloLR, which are developed for calorimeter-tagged muons, are used on the $H \rightarrow ZZ^{*} \rightarrow$

Table 4.1. The muon identification menus

family names	STACO	MuID
combined muons	STACO	MuID combined
stadalone muons	MUONBOY	MOORE MuID standalone
segment-tagged muons	MuTag	MuTagIMO
independent algorithms		MuGirl combined MuGirl segment-tagged
priority in merging	no overlap between STACO and MuTag/MUONBOY MuTag > MUONBOY	MuID combined > MuGirl combined > MuTagIMO > MuGirl segment-tagged > MuID standalone

$\ell^+\ell^-\ell'^+\ell'^-$ channel to reconstruct calorimeter-tagged muons.

4.1.2. Reconstruction and identification efficiency

The combination of the measurements made in the MS with the ones from the ID improves the momentum resolution in the range $6 < p_T < 100$ GeV. The matching of the muon track reconstructed independently in the ID and in the MS allows the rejection of muons from secondary interactions as well as the ones from π/K decays in flight. In order to combine the tracks reconstructed in the ID and the MS, the STACO program applies a strategy based on the statistical combination of the two independent measurements using the parameters of the reconstructed tracks and their covariance matrices. The reconstruction and combination efficiencies are presented in Figure 4.2 for the full p_T range. These results are obtained from detailed Geant4-based simulations. [36]

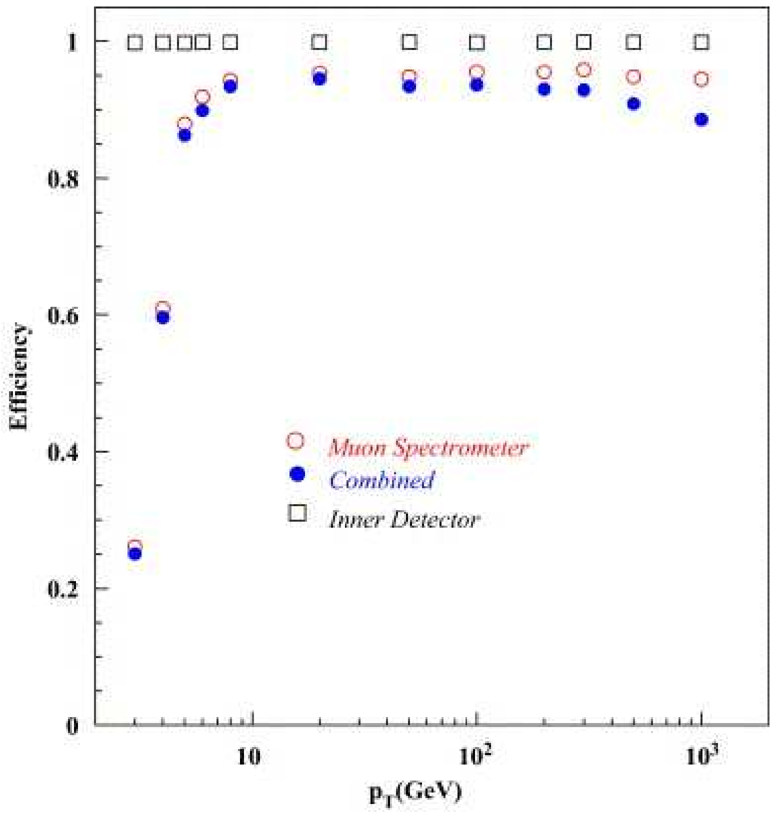

Figure 4.2. Efficiency of track reconstruction in the MS and ID, using STACO procedure, as a function of p_T. [36]

The efficiency of the muon reconstruction decreases very rapidly with decreasing p_T because accurate tracking of low p_T muons in highly inhomogeneous magnetic fields is delicate and requires a dedicated algorithm. Furthermore, as p_T decreases, the energy lost by the muons inside the calorimeters becomes comparable to their energy, especially in the barrel region. The MuTag algorithm has been developed to tag low p_T muons. The principle is to start from the ID tracks, extrapolate them to the inner layer of the MS, and try to match them with a segment reconstructed in these layers not yet associated with a combined track. Other cuts on the segment quality are applied. Figure 4.3 shows the MuTag efficiency as a function of p_T. MuTag improves muon identification up to 96% in the momentum range $5 < p_T < 100$ GeV. The MUONBOY, STACO and MuTag packages run in the official ATLAS software and their performances are determined from detailed Geant4-based simulations. [36]

Figure 4.4 shows the muon reconstruction efficiency as a function of η. The combination of all the muon reconstruction types (for combined(CB), segment-tagged(ST), and CaloTag muons) gives a uniform muon reconstruction efficiency of about 0.98 over all the detector regions. The inefficiency of the CB+ST muons at $\eta \sim 0$ is almost fully recovered by the use of CaloTag muons. The efficiencies measured in experimental and simulated data are in good agreement (within 0.5%) apart from the region at $1.5 \lesssim \eta \lesssim 2.2$. This behavior originates from a mis-modeling of the ID reconstruction efficiency that will be discussed below.

The ID muon reconstruction efficiency for $p_T > 20$ GeV as a function of η is analysed in Figure 4.5:

the left part of the figure shows an efficiency greater than 0.99, apart from the regions around $\eta = 0$ and $|\eta| = 1.7$. Figure 4.5, on the right, shows the ID muon reconstruction efficiency when only minimal ID track identification requirements (described in Ref. [27]) are applied on the muon track. The additional requirement of

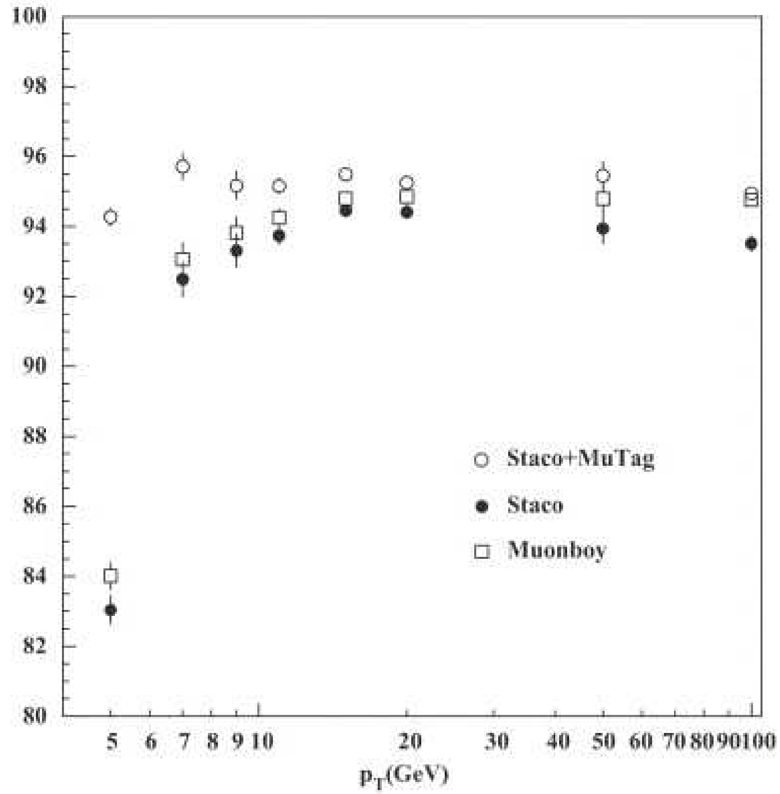

Figure 4.3. Efficiency of track reconstruction using MUONBOY, STACO and MuTag procedures, as a function of p_T. [36]

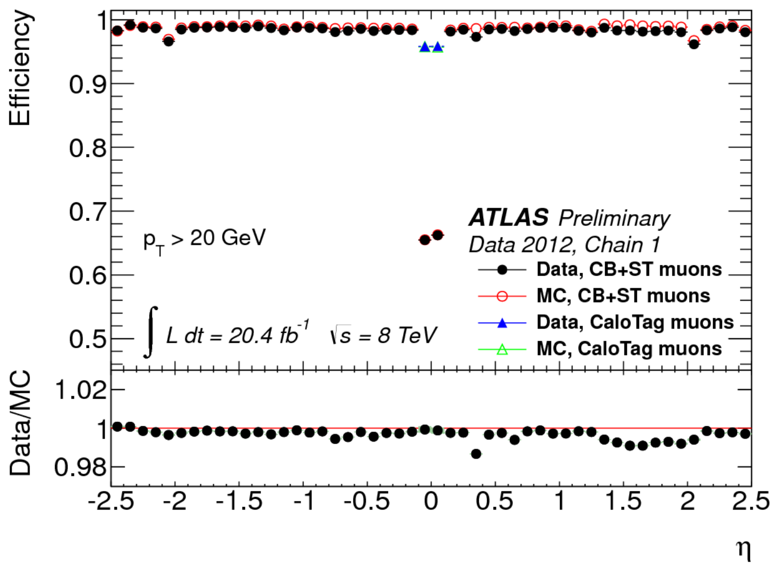

Figure 4.4. Muon reconstruction efficiency as a function of η for muons with $p_T > 20$ GeV and different muon reconstruction types. CB and ST muon types are reconstructed using the Chain 1 reconstruction algorithm. CaloTag muons are used only in the region $|\eta| < 0.1$. The panel at the bottom shows the ratio between the measured and predicted efficiencies. [27]

one hit in the innermost pixel detector layer is applied to muons passing through a sensitive area of this detector in order to ensure an accurate impact parameter measurement. The fact that not all non-operating pixel modules were treated as insensitive regions at the time of the muon reconstruction causes an inefficiency in experimental data at $1.5 < \eta < 2.2$ not modeled in simulation.

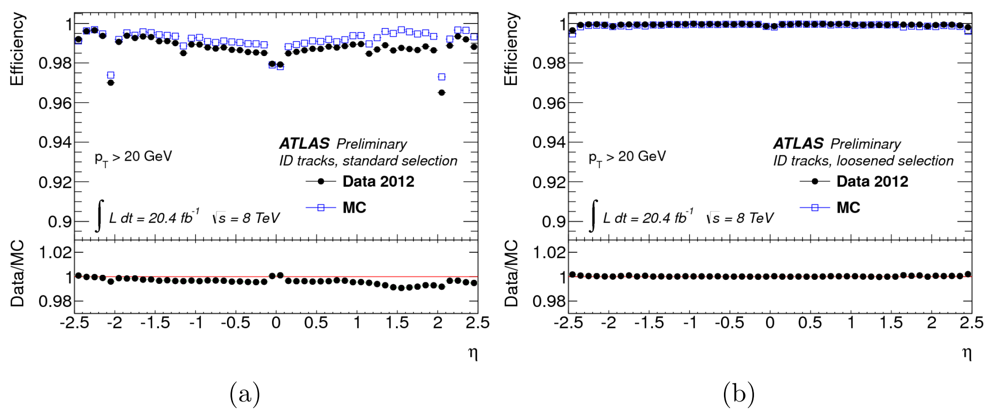

Figure 4.5. Measured ID muon reconstruction efficiency as a function of η for muons with $p_T > 20$ GeV. On the left plot the efficiency is calculated with the standard selection requirements on the hit multiplicity in the ID while the requirements are relaxed on the right plot. The panel at the bottom shows the ratio between the measured and predicted efficiencies. [27]

4.1.3. Muon resolution

The momentum resolution and scale are additional important parameters used in the evaluation of the muon reconstruction performance. Di-muon decays of the Z, J/Ψ, and γ resonances are used to determine the muon momentum resolution and scale. This allows a validation of the MC prediction for these quantities.

The p_T resolution is presented in Figure 4.6 for the full p_T range.

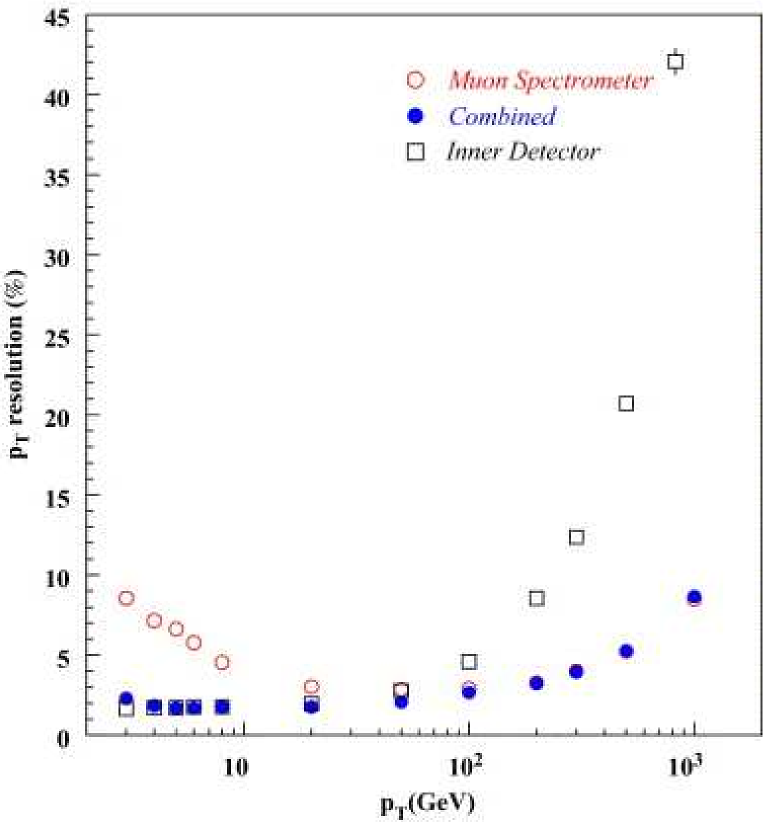

Figure 4.6. p_T resolution of track reconstruction in the MS and in the ID, using the STACO procedure, as a function of p_T. [36]

4.1.4. Muon trigger

The precise determination of the muon trigger performance of the ATLAS detector at the LHC is essential for muon-related physics analyses. The ATLAS muon trigger system has been designed to select muons in a wide momentum range with high efficiency. The selection of events with muons by the trigger system is performed in three steps. The signals from fast-response muon trigger detectors are processed by custom-built hardware to generate a Level 1 (L1) trigger. The L1 muon system has six programmable p_T thresholds to label the trigger with p_T information. In addition, the L1 trigger carries the detector position information to be investigated by the next steps. Then the HLT reconstructs tracks in the vicinity of the detector region reported by the L1 trigger. The L2 trigger performs a fast reconstruction of muons with a simple algorithm. Then the EF makes use of the offline muon reconstruction software to refine the trigger decision by utilising full detector information.

The L1 muon trigger is based on dedicated finely segmented detectors (the RPCs in the barrel and the TGCs in the end-caps, as described in detail in section 3.2.5) with a sufficient timing accuracy to provide unambiguous identification of the bunch-crossing containing the muon candidate. As shown of Figure 4.9, the RPCs are arranged in three stations.

L1 muon trigger is hardware-based. It looks for hit coincidences within different layers, and each coincidence pattern corresponds to a certain momentum threhold. HLT is software based. L2 muon trigger uses optimized algorithm to recude the execution time and EF muon trigger uses same algorithms to the offline reconstruction. The actual p_T threshold cut is defined by a hypothesis algorithm, so that the trigger efficiency for muons with nominal p_T is certain percent of the corresponding efficiency without cuts. So the actual p_T threshold is slightly lower than nominal p_T. For example, the cut in EF is 20 GeV while in L2 it is 19.33GeV for the corresponding

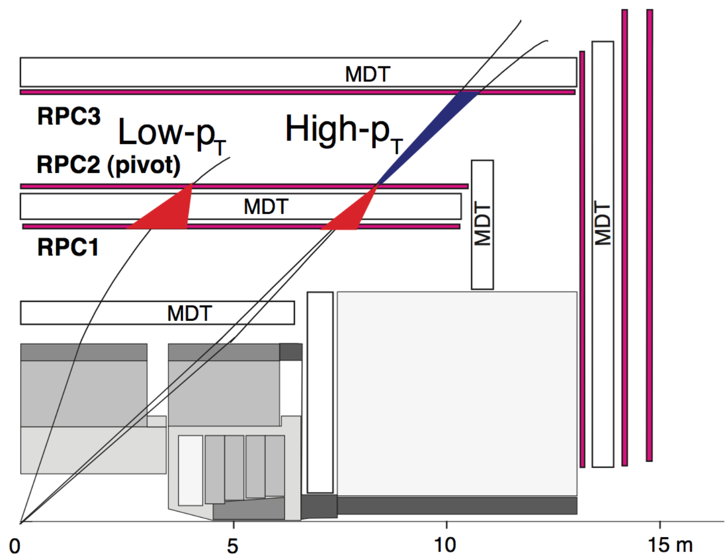

Figure 4.7. Schema of L1 muon barrel trigger. [10]

single-muon trigger.

As mentioned earlier, studies of muon trigger performance were conducted using simulated samples of single muon events generated over a large pT and angular range. L1 selection algorithms show an efficiency greater than 99% for muons with p_T above threshold. The overall acceptance (82% low-p_T, 78% high-p_T) is due exclusively to geometrical regions of the Muon Spectrometer not covered by the RPCs. Figure 4.8 shows the inefficient regions corresponding to the magnet support structures ($2.3 \leq \phi \leq 1.7$ and $1.4 \leq \phi \leq 0.9$) and the spectrometer central crack at $\eta \sim 0$, not covered by RPCs. The overall loss in geometrical acceptance due to the $\eta = 0$ crack is approximately 7% while the loss due to the support structure is about 5%. Moreover smaller inefficiency patterns are clearly visible which are due to magnetic ribs in small trigger sectors.

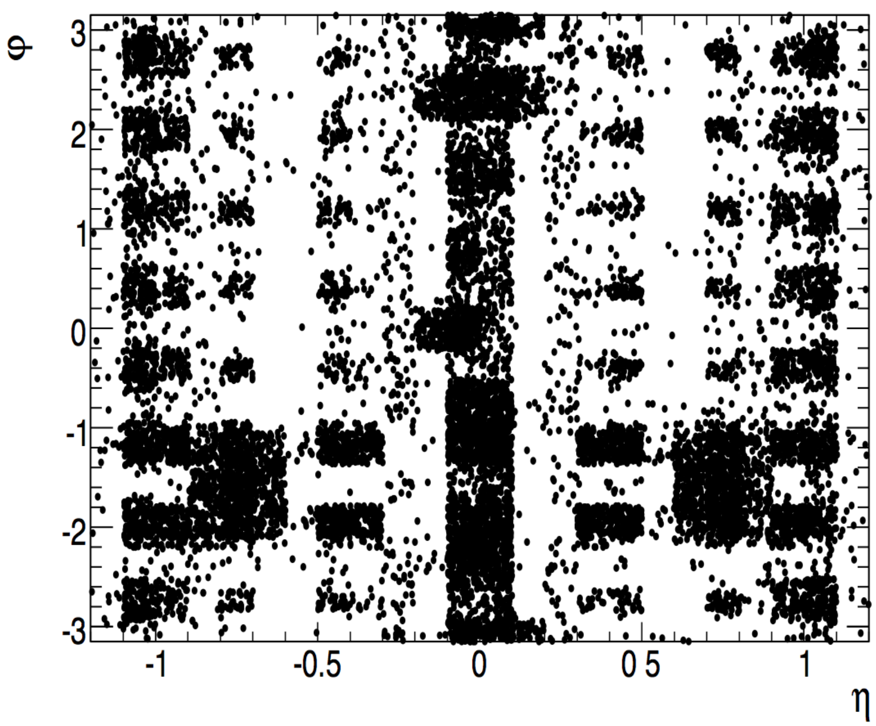

Figure 4.8. L1 geometrical acceptance in the $\eta - \phi$ plane. [26]

Figure 4.9 shows efficiency turn-on curves for high-p_T thresholds. Figure 4.10 shows L1 end-cap efficiency curves for high p_T thresholds.

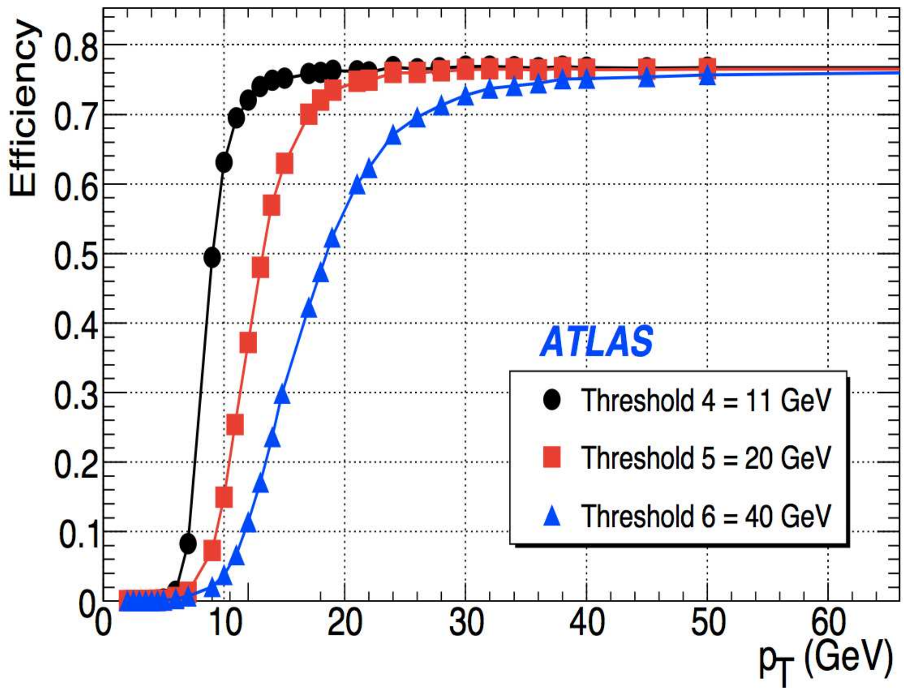

Figure 4.9. L1 barrel efficiency as function of p_T for high-p_t thresholds. [26]

Figure 4.11 shows the efficiency of the two single muon triggers, denoted mu24i_tight and mu36_tight, combined using a Boolean "OR" operation. The mu24i_tight is a single muon trigger requiring at least one isolated muon with $p_T < 24$ GeV where isolation criterion is made with inner detector tracks. The mu36_tight is a single muon trigger requiring at least one muon with $p_T > 36$ GeV without applying isolation cut. The efficiency is measured with respect to the offline reconstructed muons in the barrel region which is defined as the pseudo rapidity of the offline muon satisfies $|\eta| < 1.05$. It was measured by using Z-boson produced events with the tag-and-

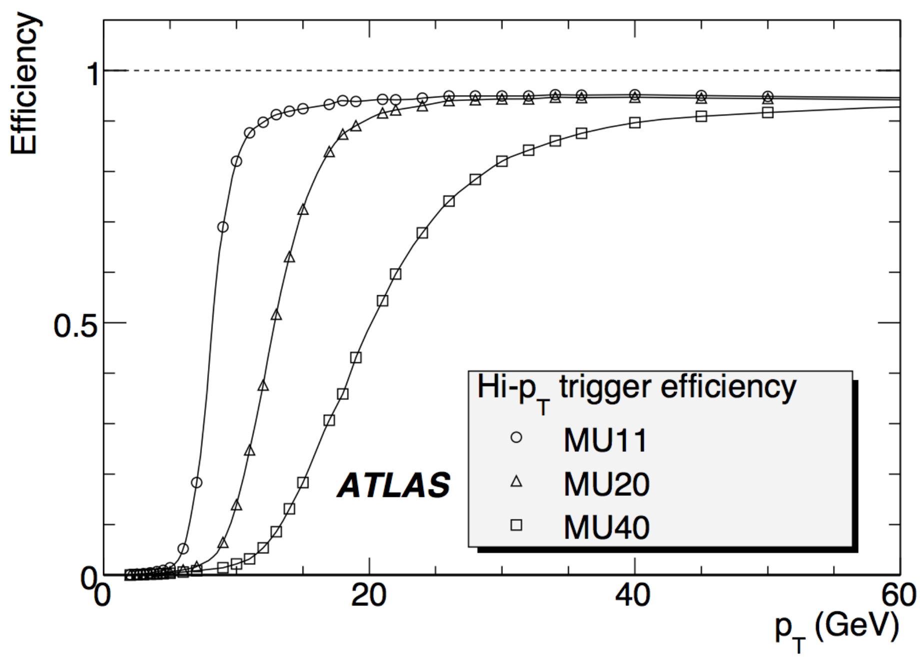

Figure 4.10. The end-cap trigger efficiency curves for high-p_T thresholds of 11, 20 and 40 GeV. [26]

probe method[1], which is exploiting well known di-muon resonances. The efficiencies are shown separately for L1 (written as Level 1), L1+L2 (written as Level 2) and L1+L2+EF (written as Event Filter) stages. The L1 threshold for these triggers is L1_MU15. It can be seen that the efficiency turn-on becomes sharper with each successive trigger level. The plateau efficiency is dominated by L1, where the HLT efficiency with respect to L1 is about 98%.

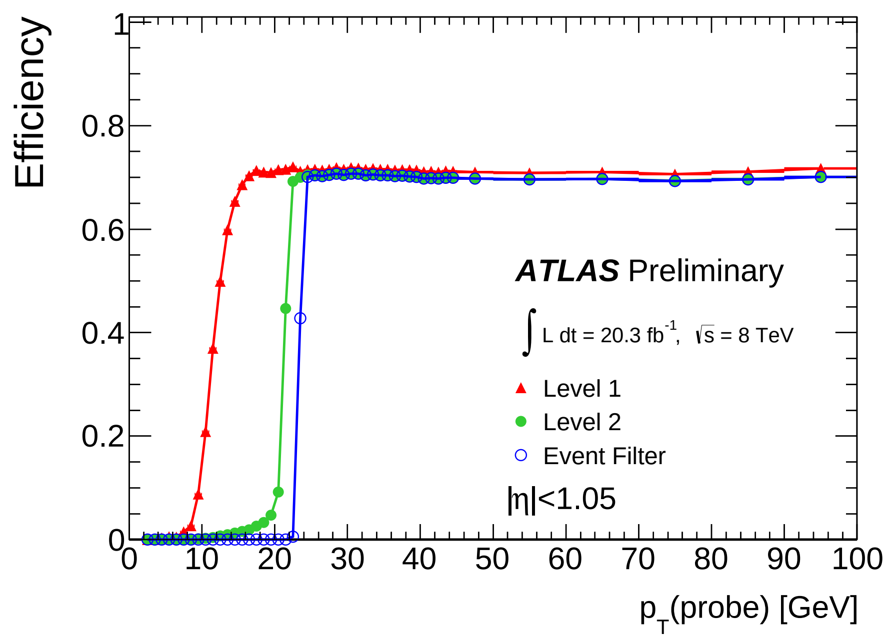

Figure 4.11. Efficiency of the primary single muon trigger separately for L1, L2, EF at barrel region in data. [1]

Figure 4.12 shows the efficiency of the two single muon triggers, mu24i_tight and mu36_tight, convolved as an OR between the two. The requirements and the written

[1] A combined muon, the tag, is required in the event. The tag is paired with a track reconstructed in the Inner Detector, the probe, giving an invariant mass close to the considered resonance mass. The fraction of reconstructed signal probes measures the muon identification efficiency.

methods are the same as barrel efficiency above.

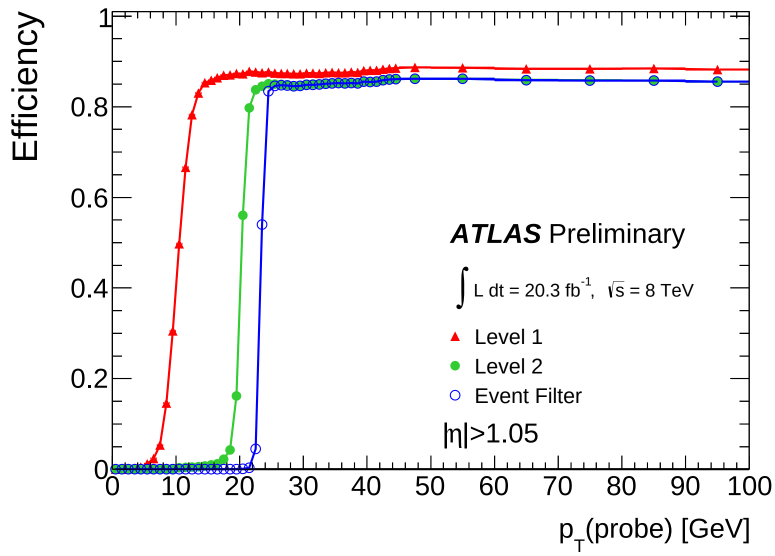

Figure 4.12. Efficiency of the primary single muon trigger separately for L1, L2, EF at endcap region in data. [1]

4.2. Electron

Electron candidates must have a well-reconstructed ID track pointing to an electromagnetic calorimeter cluster. The cluster must satisfy a set of identication criteria that require the longitudinal and transverse shower proles to be consistent with those expected for electromagnetic showers. Tracks associated with electromagnetic clusters are fitted using a Gaussian-Sum Filter [23], which allows for bremsstrahlung energy losses to be taken into account.

The electron identication in ATLAS is based on requirements on variables that provide good separation between isolated electrons and hadronic jets faking electrons. In the central region of $|\eta| < 2.47$, variables describing the longitudinal and transverse shapes of the electromagnetic showers in the calorimeters, the properties of the tracks in the inner detector, e.g. energy deposits in specific layers of tacking system, or change in the momentum from the beginning to the end of the track from bremsstrahlung, as well as the matching between tracks and energy clusters are used to discriminate against the different background sources. These variables are detailed in Table 4.2.

Electron reconstruction and identication in the 2012 dataset For the 2012 dataset a multivariate analysis (MVA) technique is employed to dene the electron identication, since it allows for simultaneous evaluation of several properties when making a selection decision. Out of the different MVA techniques, the maximum Likelihood (LH) approach has been chosen for electron identication because of its simple construction.

The electron LH makes use of signal and background probability density functions (PDFs) of the discriminating variables. Based on these PDFs, an overall probability is calculated for the object to be signal or background. The signal and background probabilities for a given electron are combined into a discriminant on which a cut is applied:

$$d_{\mathcal{L}} = \frac{\mathcal{L}_S}{\mathcal{L}_S + \mathcal{L}_B}, \qquad \mathcal{L}_S(\vec{x}) = \prod_{i=1}^{n} P_{s,i}(x_i) \tag{4.1}$$

where $\vec{x}$ is the vector of variable values and $P_{s,i}(x_i)$ is the value of the signal probability density function of the i^{th} variable evaluated at x_i. In the same way, $P_{b,i}(x_i)$ refers to the background probability function. The choice of the cut value on the discriminant determines the signal efficiency/background rejection of the Likelihood working point.

Signal and background PDFs used for the electron LH Particle Identification (PID) are obtained from data. Furthermore, variables could be added whose overlap between signal and background is too large for explicit cuts, but nonetheless have significant discriminating power. The variables counting the hits on the track are not used as PDFs in the LH, but are left as simple cuts, as every electron should have a high

Table 4.2. Definition of electron discriminating variables [22].

Type	Description	Name
Hadronic leakage	Ratio of E_T in the first layer of the hadronic calorimeter to E_T of the EM cluster (used over the range $\|\eta\| < 0.8$ and $\|\eta\| > 1.37$)	R_{Had1}
	Ratio of E_T in the hadronic calorimeter to E_T of the EM cluster (used over the range $\|\eta\| > 0.8$ and $\|\eta\| < 1.37$)	R_{Had}
Third layer of EM calorimeter	Ratio of the energy in the third layer to the total energy	f_3
Middle layer of EM calorimeter	Lateral shower width, $\sqrt{(\Sigma E_i \eta_i^2)/(\Sigma E_i) - ((\Sigma E_i \eta_i)/(\Sigma E_i))^2}$, where E_i is the energy and η_i is the pseudorapidity of cell i and the sum is calculated within a window of 3×5 cells	$W_{\eta 2}$
	Ratio of the energy in 3×3 cells over the energy in 3×7 cells centered at the electron cluster position	R_ϕ
	Ratio of the energy in 3×7 cells over the energy in 7×7 cells centered at the electron cluster position	R_η
Strip layer of EM calorimeter	Shower width, $\sqrt{(\Sigma E_i (i - i_{\text{max}})^2)(\Sigma E_i)}$, where i runs over all strips in a window of $\Delta\eta \times \Delta\phi \approx 0.0625 \times 0.2$, corresponding typically to 20 strips in η, and i_{max} is the index of the highest-energy strip	W_{stot}
	Ratio of the energy difference between the largest and second largest energy deposits in the cluster over the sum of these energies	E_{ratio}
	Ratio of the energy in the strip layer to the total energy	f_1
Track quality	Number of hits in the B-layer (discriminates against photon conversions)	n_{Blayer}
	Number of hits in the pixel detector	n_{Pixel}
	Number of total hits in the pixel and SCT detectors	n_{Si}
	Transverse impact parameter	d_0
	Significance of transverse impact parameter defined as the ratio of d_0 and its uncertainty	σ_{d_0}
	Momentum lost by the track between the perigee and the last measurement point divided by original momentum	$\Delta p/p$
TRT	Total number of hits in the TRT	n_{TRT}
	Ratio of the number of high-threshold hits to the total number of hits in the TRT	F_{HT}(rTRT)
Track–cluster matching	$\Delta\eta$ between the cluster position in the strip layer and the extrapolated track	$\Delta\eta_1$
	$\Delta\phi$ between the cluster position in the middle layer and the extrapolated track	$\Delta\phi_2$
	Defined as $\Delta\phi_2$, but the track momentum is rescaled to the cluster energy before extrapolating the track to the middle layer of the calorimeter	$\Delta\phi_{\text{Res}}$
	Ratio of the cluster energy to the track momentum	E/p
Conversions	Veto electron candidates matched to reconstructed photon conversions	!isConv

quality track to allow for a robust 4-vector measurement. A menu of selection criteria denoted by "LOOSE LH" has been chosen to define the electron identification of this analysis. This method was selected for Higgs physics because compared to other competing methods within ATLAS, it maintained the same efficiency while improving light-flavor jet rejection by a factor of 2. rejection by a factor of two. In Figure 4.13 the ratios of background efficiencies for the likelihood/cut-based menus are shown in function of η (left) and E_T (right).

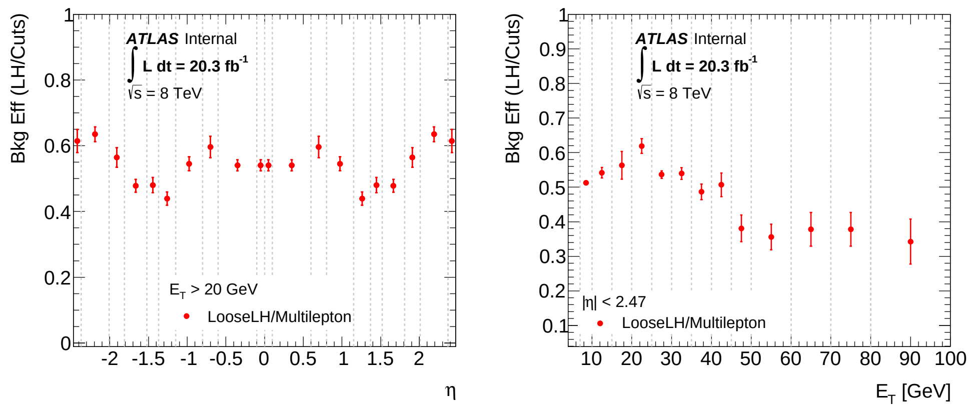

(a) (b)

Figure 4.13. Ratio of background efficiencies for the likelihood/cut-based menus.The uncertainties are statistical only. The ratio is shown vs. η (left) and vs. E_T (right). The light jet background samples is taken form data using electron supporting triggers to look at inclusive backgrounds samples in data. The efficiencies are calculated using objects in the electron container that also pass track quality requirements. To reject real electron contamination from Zs and Ws, electron objects which lie in the Z-peak or have MET$>$ 25 GeV or M$_T$ $>$ 40 GeV are rejected.For the eta plot, we use $>$ 20 GeV electrons, and for the E_T plot we use $>$ 7 GeV electrons.

Table 4.3 summarises which variables are used for the different menus of the cut-based and likelihood identification. As it is shown in Table 4.3, the LOOSE LH selection uses essentially the same variable set as for the *multilepton* cut-based. In addition, the LOOSE LH includes two variables which improve discrimination but are difficult to use in a cut-based method, namely the fraction of energy in the first sampling and R_{phi}. More details of LH construction and the PDFs can see in Ref. [13].

The electron identification in ATLAS is based on requirements on variables that provide good separation between isolated electrons and hadronic jets faking electrons. In the *central region* of $|\eta| < 2.47$, variables describing the longitudinal and transverse shapes of the electromagnetic showers in the calorimeters, the properties of the tracks in the inner detector, e.g. number of b-layer and silicon hits, signal in TRT, or change in the momentum from the beginning to the end of the track from bremsstrahlung, as well as the macthing between tracks and energy clusters are used to discriminate against the different background sources. These variables are detailed in Table 4.3.

Table 4.3. The electron identification menus [13].

	Cut-based				Likelihood		
Name	*loose*	*medium*	*tight*	*multilepton*	LOOSE	MEDIUM	VERY TIGHT
$R_{\mathrm{Had(1)}}$	✓	✓	✓	✓	✓	✓	✓
f_3		✓	✓	✓	✓	✓	✓
W_η	✓	✓	✓	✓	✓	✓	✓
R_η	✓	✓	✓	✓	✓	✓	✓
R_ϕ					✓	✓	✓
W_{stot}	✓	✓	✓	✓	✓	✓	✓
E_{ratio}	✓	✓	✓	✓	✓	✓	✓
f_1					✓	✓	✓
n_{Blayer}		✓	✓	✓	✓	✓	✓
n_{Pixel}	✓	✓	✓	✓	✓	✓	✓
n_{Si}	✓	✓	✓	✓	✓	✓	✓
d_0		✓	✓			✓	✓
σ_{d_0}						✓	✓
$Deltap/p$				✓	✓	✓	✓
n_{TRT}		✓	✓	✓	✓	✓	✓
F_{HT}		✓	✓	✓	✓	✓	✓
$\Delta\eta_1$	✓	✓	✓	✓	✓	✓	✓
$\Delta\phi_2$			✓				
$\Delta\phi_{Res}$				✓	✓	✓	✓
E/p			✓				
!isConv			✓				✓

4.2.1. $E - p$ combination for electrons

In order to improve on the energy resolution of low E_T electrons and electrons in problematic regions of the electromagnetic calorimeter, such as the "crack region" in $1.37 < |\eta| < 1.52$ where response tends to be poorer, a combination of the track momentum and the cluster energy is performed. Specifically, the combination is applied to electrons with $p_{\mathrm{T}} < 30$ GeV and $\eta < 1.52$, and which have consistent Inner Detector and cluster energy measurements, as judged by the ratio:

$$\mathrm{significance}(\mathrm{E_{Cluster}} - \mathrm{p_{Track}}) = \frac{|\mathrm{E_{Cluster}} - \mathrm{p_{Track}}|}{\sqrt{\sigma^2_{\mathrm{E_{Cluster}}} + \sigma^2_{\mathrm{p_{Track}}}}} < 5 \tag{4.2}$$

The combination method employs a maximum likelihood fit of $p_{\mathrm{T}}^{\mathrm{Track}}$ and $p_{\mathrm{T}}^{\mathrm{Cluster}}$, using probability density functions (PDFs) which are generated by fitting the $p_{\mathrm{T}}^{\mathrm{Track}}/p_{\mathrm{T}}^{\mathrm{Truth}}$ and $p_{\mathrm{T}}^{\mathrm{Cluster}}/p_{\mathrm{T}}^{\mathrm{Truth}}$ distributions with a Crystal Ball function[2] in order to take into account both the resolution gaussian core and the tails of the distributions. In Figure 4.14 some examples of the track and cluster PDFs can be found. The events used to build the PDFs come from single $e^{\pm}$ Monte Carlo samples with flat E_T spectra on $7 < E_T < 80$ GeV, with all constituent electrons required to have $\mathrm{significance}(\mathrm{E_{Cluster}} - \mathrm{p_{Track}}) < 5$.

4.2.2. Electron calibration

The electron and photon energy reconstruction together with the precise determination of the scale and resolution are fundamental ingredients for the mass measurment of the new boson discovered in 2012. To decrease and improve the electron and photon calibration, the full calibration procedure has been completely revisited exploiting the potential of multivariate techniques. The calibration procedure for electrons and photons is described in [12].

[2]The "Crystal Ball function" is a probability density function commonly used to model various lossy processes in high-energy physics.[56]

(a)

p_{T} Region	Definition
Low	$7 < p_{\mathrm{T}} < 15$ GeV
Medium	$15 < p_{\mathrm{T}} < 30$ GeV
High	$p_{\mathrm{T}} > 30$ GeV

(b)

$\|\eta\|$ Region	Definition
Central	$\|\eta\| < 0.8$
Medium	$0.8 < \|\eta\| < 1.37$
Crack	$1.37 < \|\eta\| < 1.52$
Forward	$1.37 < \|\eta\| < 2.5$

Table 4.4. Definitions of the p_{T} and $|\eta|$ regions used in this analysis.

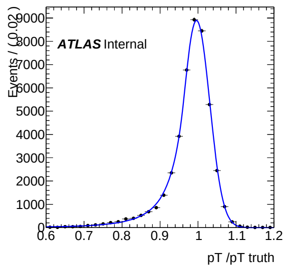

(a) Low p_{T}, central η

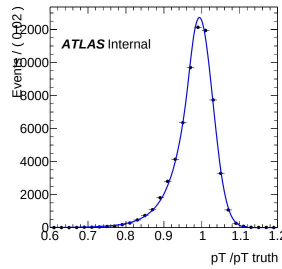

(b) Medium p_{T}, medium η

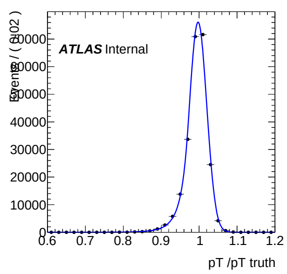

(c) High p_{T}, medium η

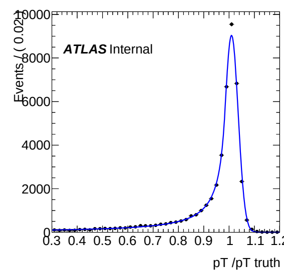

(d) Low p_{T}, central η

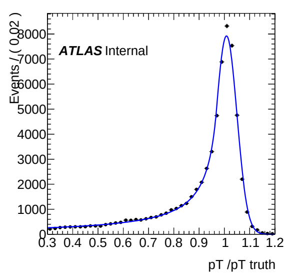

(e) Medium p_{T}, medium η

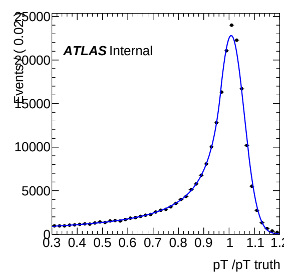

(f) High p_{T}, medium η

Figure 4.14. Crystal Ball function fits of $p_{\mathrm{T}}^{\mathrm{Cluster}}/p_{\mathrm{T}}^{\mathrm{Truth}}$ ((a), (b) and (c)) and $p_{\mathrm{T}}^{\mathrm{Track}}/p_{\mathrm{T}}^{\mathrm{Truth}}$ ((d), (e) and (f)) in various transverse momentum and pseudorapidity regions.

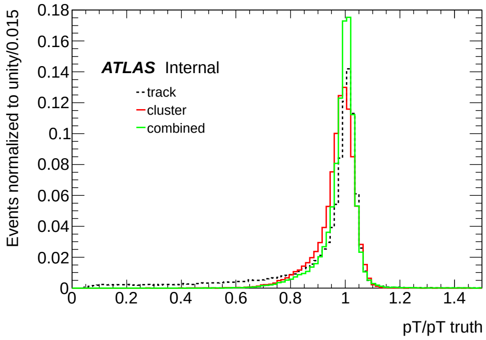

(a) Low p_{T}, central η

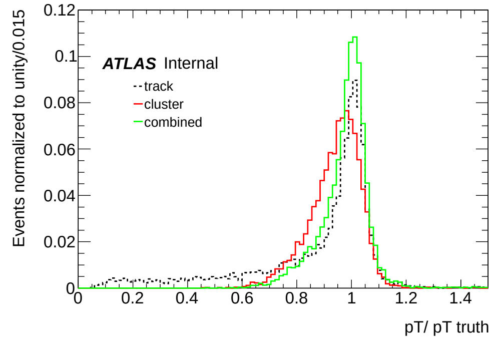

(b) Low p_{T}, medium η

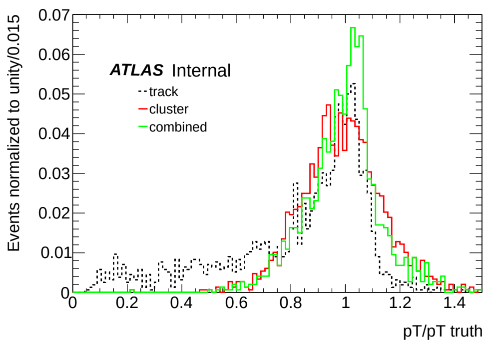

(c) Low p_{T}, crack η

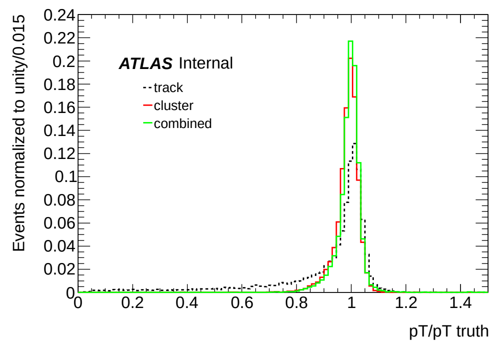

(d) Medium p_{T}, central η

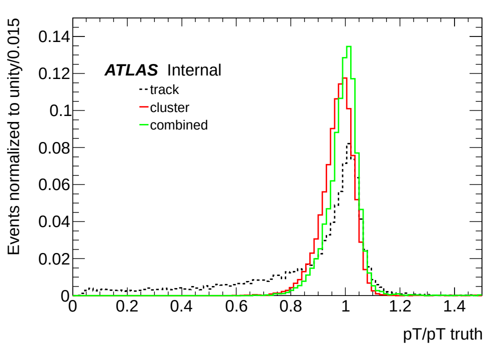

(e) Medium p_{T}, medium η

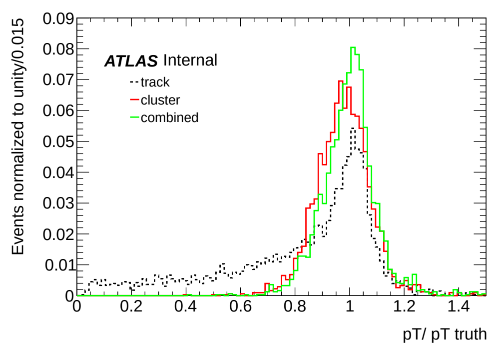

(f) Medium p_{T}, crack η

Figure 4.15. Improvement in $p_{\mathrm{T}}/p_{\mathrm{T}}^{\mathrm{Truth}}$ for Monte Carlo single electrons after the likelihood $E-p$ combination, as compared to the standard approach (E_{Cluster} only). Low and medium p_{T} ranges are shown in various η regions of the detector.

Chapter 5

Event Selection and Backgrounds Estimate

5.1. Event Selection

The data are subjected to quality requirements: if any relevant detector component is not operating correctly during a period when an event is recorded, the event is rejected. Events are required to have at least one vertex with three associated tracks with $p_T > 400$ MeV, and the primary vertex is chosen to be the reconstructed vertex with the largest track Σp_T^2. Identical requirements are applied to all four-lepton final states. For the inclusive analysis, four-lepton events are selected and classified according to their channel: 4μ, $2e2\mu$, $2\mu 2e$, $4e$. These events are subsequently categorized according to their production mechanism to provide measurements of each corresponding signal strength.

The inclusive analysis of four-lepton events were selected with single-lepton and dilepton triggers. The p_T (E_T) thresholds for single-muon (single-electron) triggers increased from 18 GeV to 24 GeV (20 GeV to 24 GeV) between the 7 TeV and 8 TeV data, in order to cope with the increasing instantaneous luminosity. The dilepton trigger thresholds for 7 TeV data are set at 10 GeV p_T for muons, 12 GeV E_T for electrons and (6,10) GeV for (muon,electron) mixed-flavor pairs. For the 8 TeV data, the thresholds were raised to 13 GeV for the dimuon trigger, to 12 GeV for the dielectron trigger and (8,12) GeV for the (muon,electron) trigger; furthermore, a dimuon trigger with different thresholds on the muon p_T, 8 and 18 GeV, was added. The trigger efficiency for events passing the final selection is above 97% in the 4μ,

$2\mu 2e$ and $2e2\mu$ channels and close to 100% in the $4e$ channel for both 7 TeV and 8 TeV data.

Higgs boson candidates are formed by selecting two same-flavor, opposite-sign lepton pairs (a lepton quadruplet) in an event. Each lepton is required to have a longitudinal impact parameter less than 10 mm with respect to the primary vertex, and muons are required to have a transverse impact parameter of less than 1 mm to reject cosmic-ray muons. The only exception is applied to standalone muons, that have no ID track. Each electron (muon) must satisfy $E_T > 7$ GeV ($p_T > 6$ GeV) and be measured in the pseudorapidity range $|\eta| < 2.47$ ($|\eta| < 2.7$). The highest-p_T lepton in the quadruplet must satisfy $p_T > 20$ GeV, and the second (third) lepton in order of p_T must satisfy $p_T > 15$ GeV ($p_T > 10$ GeV). Each event is required to have the triggering lepton(s) matched to one or two of the selected leptons.

Multiple quadruplets within a single event are possible: for four muons or four electrons there are two ways to pair the masses, and for five or more leptons there are multiple ways to choose the leptons. Quadruplet selection is done separately in each subchannel - 4μ, $2e2\mu$, $2\mu 2e$, $4e$ - keeping only a single quadruplet per channel. For each channel, the lepton pair with the mass closest to the Z boson mass is referred to as the leading dilepton and its invariant mass, m_{12}, is required to be between 50 GeV and 106 GeV. The second, subleading, pair in each channel is chosen from the remaining leptons as the pair closest in mass to the Z boson and in the range $m_{min} < m_{34} < 115$GeV, where m_{min} is 12 GeV for $m_{4\ell} < 140$ GeV, Finally, if more than one channel has a quadruplet passing the selection, the channel with the highest expected signal rate is kept, i.e. in the order - 4μ, $2e2\mu$, $2\mu 2e$, $4e$ - a ranking based on Branch Fraction efficiency.

Events with a selected quadruplet are required to have their leptons a distance $\Delta R > 0.1$ from each other if they are of the same flavor (to make sure the lepton pair is not the same lepton) and $\Delta R > 0.2$ otherwise (to make sure the lepton is not in the isolation cone of the other lepton). For 4μ and $4e$ events, if an opposite-charge same-flavor dilepton pair is found with $m_{\ell\ell}$ below 5 GeV the event is removed, which is based on the measurement sensitivity of ATLAS detector.

The Z+jets and $t\bar{t}$ background contributions are further reduced by applying impact parameter requirements as well as track- and calorimeter-based isolation requirements to the leptons. The details can be checked with the cut flow in Ref. [24]. The transverse impact parameter significance, defined as the impact parameter in the transverse plane divided by its uncertainty, $|d_0|/\sigma_{d_0}$, for all muons (electrons) is required to be lower than 3.5 (6.5) to suppress the faked leptons. The normalized track isolation discriminant, defined as the sum of the transverse momenta of tracks, inside a cone of size $\Delta R = 0.2$ around the lepton also to suppress faked lepton, excluding the lepton track, divided by the lepton p_T, is required to be smaller than 0.15, which is determined by the optimization study.

The relative calorimetric isolation for electrons in the 2012 data set is computed as the sum of the cluster transverse energies E_T, in the electromagnetic and hadronic calorimeters, with a reconstructed barycenter inside a cone of size $\Delta R = 0.2$ around the candidate electron cluster, divided by the electron E_T. The electron relative calorimetric isolation is required to be smaller than 0.2 to suppress fake leptons. The cells within 0.125×0.175 in $\eta \times \phi$ around the electron barycenter are excluded. The pile-up and underlying event contribution to the calorimeter isolation is subtracted event-by-event. The calorimetric isolation of electrons in the 2011 data set is cell-based (electromagnetic and hadronic calorimeters) rather than cluster-based, and the calorimeter isolation relative to the electron E_T requirement is 0.3 instead of 0.2. In the case of muons, the relative calorimetric isolation discriminant is defined as the sum, ΣE_T, of the calorimeter cells above 3.4σ, where σ is the quadrature sum of the expected electronic and pileup noise, inside a cone of size $\Delta R < 0.2$ around the muon direction, divided by the muon p_T. Muons are required to have a relative calorimetric isolation less than 0.3 (0.15 in case of standalone muons). For both the track- and calorimeter-based isolations any contributions arising from other leptons of the quadruplet are subtracted.

As discussed in Chapter 4, a search is performed for FSR photons arising from any of the lepton candidates in the final quadruplet, and at most one FSR photon candidate is added to the 4ℓ system. The FSR correction is applied only to the leading dilepton, and priority is given to collinear photons associated with the leading dimuon. The correction is applied if $66 < m_{\mu\mu} < 89$ GeV and $m_{\mu\mu\gamma} < 100$ GeV. If the collinear-photon search fails then the non-collinear FSR photon with the highest E_T is added, provided it satisfies the following requirements: $m_{\ell\ell} < 81$ GeV and $m_{\ell\ell\gamma} < 100$ GeV. The expected fraction of collinear (non-collinear) corrected events is 4% (1%).

For the 7 TeV data, the combined signal reconstruction and selection efficiency for $m_H = 125$ GeV is 39% for the 4μ channel, 25% for the $2e2\mu/2\mu2e$ channels and 17% for the $4e$ channel. The improvements in the electron reconstruction and identification for the 8 TeV data lead to increases in these efficiencies by 23% for the channels with electrons, bringing their efficiencies to 27% for the $2e2\mu/2\mu2e$ channels and 20% for the $4e$ channel.

After the FSR correction, the lepton four-momentum of the leading dilepton are recomputed by means of a Z-mass-constrained kinematic fit. The fit uses a Breit-Wigner Z line shape and a single Gaussian to model the lepton momentum response function with the Gaussian σ set to the expected resolution for each lepton. Figure 5.1 shows the invariant mass distributions of $Z \to \mu^+\mu^-(\gamma)$ events in data before collinear and nonconllinear FSR correction with after collinear and noncollinear FSR correction. The Z-mass constraint improves the $m_{4\ell}$ resolution by about 15%. More

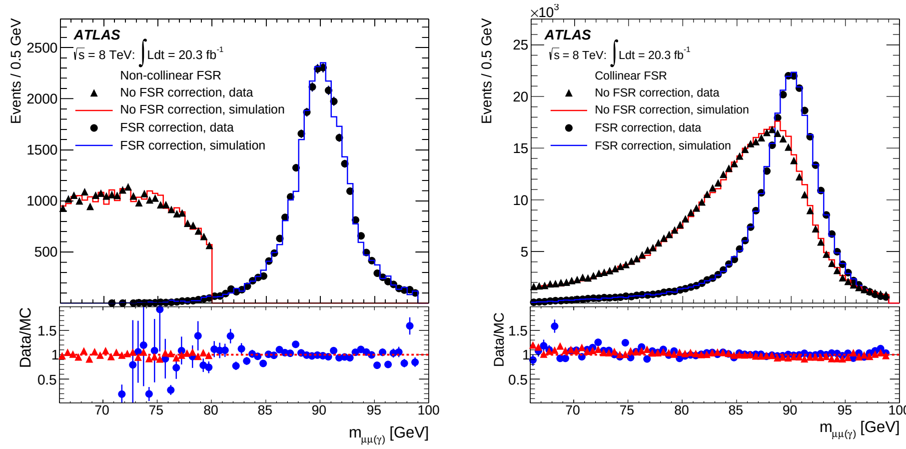

Figure 5.1. (a) The invariant mass distributions of $Z \to \mu^+\mu^-(\gamma)$ events in data before collinear FSR correction (filled triangles) and after collinear FSR correction (filled circles) (b) The invariant mass distributions of $Z \to \mu^+\mu^-(\gamma)$ events with a noncollinear FSR photon. The prediction of the simulation is shown before correction (red histogram) and after correction (blue histogram).[15]

complex momentum response functions were compared to the single Gaussian and found to have only minimal improvement for the $m_{4\ell}$ resolution. Events satisfying the above criteria are considered candidate signal events for the inclusive analysis, defining a signal region independent of the value of $m_{4\ell}$.

5.2. Background Estimate

The rate of the ZZ^* background is estimated using simulation normalized to the SM cross section as described in Sec. 5.2.2, while the rate and composition of the reducible $\ell\ell$+jets and $t\bar{t}$ background processes are evaluated with data-driven methods (not based on simulation). The composition of the reducible backgrounds depends (all leptons in the 4ℓ are prompt leptons) on the flavor of the subleading dilepton pair, and different approaches are taken for the $\ell\ell + \mu\mu$ and the $\ell\ell + ee$ final states. These two cases are discussed in Secs. 5.2.3 and 5.2.4, respectively, and the yields for all reducible backgrounds in the signal region are summarized in Tables. Finally, the small contribution from the WZ reducible background is estimated from simulation. The background estimation was described in detail in public ATLAS Collaboration notes [25].

5.2.1. Backgrounds Introduction

The Feyman diagram of the irreducible background (one or more leptons in the 4ℓ are non-prompt leptons) ZZ^* is shown in Figure 5.2 (a), the reducible background $\ell\ell$+jets is shown in Figure 5.2 (b), and the reducible background $t\bar{t}$ is shown in Figure 5.2 (c). In the next sections, I descibe the relevant details of how they are assessed.

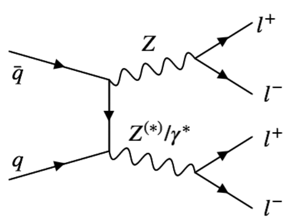

(a)

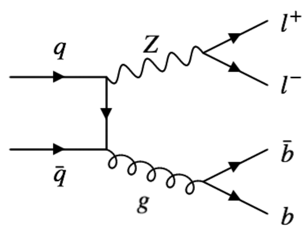

(b)

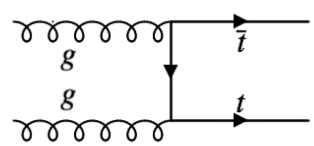

(c)

Figure 5.2. Feyman diagrams of main Higgs to four leptons backgrounds. (a) Irreducible background ZZ^*; (b) Reducible background $\ell\ell$+jets; (c) Reducible background $t\bar{t}$

5.2.2. ZZ^* Background

The ZZ^* continuum background is modeled using a MC generator called "Powheg-Box" for quark-antiquark annihilation and "GG2ZZ" for gluon fusion [48]. The PDF+α_s and QCD scale uncertainties are parameterized as functions of $m_{4\ell}$ as recommended in Ref. [20, 25]. For the ZZ^* background at $m_{4\ell} = 125$ GeV, the quark-initiated (gluon-initiated) processes have a QCD scale uncertainty of $\pm5\%$ ($\pm25\%$), and $\pm4\%$ ($\pm8\%$) for the PDF and α_s uncertainties, respectively. A tag-and-probe method, described in detail in Ref. [2], is employed to measure the reconstruction efficiencies[1] of all muon types within the acceptance of the ID ($|\eta| < 2.5$)

5.2.3. Background $\ell\ell + \mu\mu$

"Reducible backgrounds" are those without a real ZZ pair. The $\ell\ell+\mu\mu$ reducible background arises from Z+jets and $t\bar{t}$ processes, where the $Z+$ jets contribution has a $Zb\bar{b}$ heavy-flavor quark component in which the heavy-flavor quarks decay semileptonically, and a component arising from $Z+$ light-flavor jets with subsequent π/K in-flight decays. These both yield leptons, not all from Z bosons. The number of background events from $Z+$ jets and $t\bar{t}$ production is estimated from an unbinned maximum likelihood fit, performed simultaneously to four orthogonal control regions, each of them providing information on one or more of the background components. The fit results are expressed in terms of yields in a reference control region, defined by applying the analysis event selection except for the isolation and impact parameter requirements to the subleading dilepton pair. The reference control region is also used for the validation of the estimates. Finally, the background estimates in the reference control region are extrapolated to the signal region. These steps are detailed below.

[1] Efficiencies determined with the tag-and-probe method, and with an alternate method based on MC truth, were found to agree within statistical uncertainty [11]. This also shows that any possible correlations between the tag and the probe muons are negligible.

The control regions used in the maximum likelihood fit are designed to minimize contamination from the Higgs boson signal and the ZZ^* background. The four control regions are:

1. a) Inverted requirement on impact parameter significance. Candidates are selected following the analysis event selection, but 1) without applying the isolation requirement to the muons of the subleading dilepton and 2) requiring that at least one of the two muons fails the impact parameter significance requirement. As a result, this control region is enriched in $Zb\bar{b}$ and $t\bar{t}$ events.

2. b) Inverted requirement on isolation. Candidates are selected following the analysis event selection, but requiring that at least one of the muons of the subleading dilepton fails the isolation requirement. As a result, this control region is enriched in $Z+$ light-flavor-jet events (π/K in-flight decays) and $t\bar{t}$ events.

3. c) $e\mu$ leading dilepton ($e\mu + \mu\mu$). Candidates are selected following the analysis event selection, but requiring the leading dilepton to be an electron-muon pair. This violates charged lepton flavor constraction in the Standard Model, and so is a pure background. Moreover, the isolation and impact parameter requirements are not applied to the muons of the subleading dilepton, which are also allowed to be same or opposite charge sign. Events containing a Z-boson candidate decaying into e^+e^- or $\mu^+\mu^-$ pairs are removed with a requirement on the mass. This control region is dominated by $t\bar{t}$ events.

4. d) Same-sign subleading dilepton. The analysis event selection is applied, but for the subleading dilepton neither isolation nor impact parameter significance requirements are applied and the leptons are required to have the same charge sign (SS). This same-sign control region is not dominated by a specific background; all the reducible backgrounds have a significant contribution.

The expected composition for each control region is shown in Table 5.2.3. The uncertainties on the relative yields between the control regions and the reference control region are introduced in the maximum likelihood fit as nuisance parameters. The residual contribution from ZZ^* and the contribution from WZ production, where contrary to the $Z+$ jets and $t\bar{t}$ backgrounds only one of the leptons in the subleading dilepton is expected to be a non-isolated background-like muon, are estimated for each control region from simulation.

Table 5.1. Expected contribution of the $\ell\ell + \mu\mu$ background sources in each of the control regions.

	Control region			
Background	Inverted d_0	Inverted isolation	$e\mu + \mu\mu$	$same - sign$
$Zb\bar{b}$	$32.8 \pm 0.5\%$	$26.5 \pm 1.2\%$	$0.3 \pm 1.2\%$	$30.6 \pm 0.7\%$
Z+light-flavor jets	$9.2 \pm 1.3\%$	$39.3 \pm 2.6\%$	$0.0 \pm 0.8\%$	$16.9 \pm 1.6\%$
$t\bar{t}$	$58.0 \pm 0.9\%$	$34.2 \pm 1.6\%$	$99.7 \pm 1.0\%$	$52.5 \pm 1.1\%$

In all the control regions the observable is the mass of the leading dilepton, m_{12}, which peaks at the Z mass for the resonant (Z+jets) component and has a broad distribution for the non-resonant ($t\bar{t}$) component. For the $t\bar{t}$ component the m_{12} distribution is modeled by a second-order Chebyshev polynomial[2], while for the $Z+$ jets component it is modeled using a convolution of a Breit-Wigner distribution with a Crystal Ball function. The shape parameters are derived from simulation. In the combined fit, the shape parameters are constrained to be the same in each of the control regions, and are allowed to fluctuate within the uncertainties obtained from

[2]The Chebyshev differential equation is written as $(1-x^2)\frac{d^2y}{dx^2} - x\frac{dy}{dx} + n^2y = 0 \quad n = 0, 1, 2, 3, ...,$ general solution is $y = A\mathrm{T}_n(x) + B\mathrm{U}_n(x) \quad |x| < 1$, where $\mathrm{T}_n(x)$ and $\mathrm{U}_n(x)$ are defined as first- and second-order Chebyshev polynomials of degree n, respectively.

simulation. The results of the combined fit in the four control regions are shown in Figure 5.3, along with the individual background components, while the event yields in the reference control region are summarized in Table 5.2.3. As a validation of the fit method, the maximum likelihood fit is applied to the individual control regions yielding estimates compatible to those of the combined fit; these are also summarized in Table 5.2.3.

Table 5.2. Data driven $\ell\ell+\mu\mu$ background estimates for the $\sqrt{s} = 7$ TeV and $\sqrt{s} = 8$ TeV data, expressed as yields in the reference control region, for the combined fit and fits to the individual control regions. In the individual control regions only the total Z+jets contribution can be determined, while the $e\mu + \mu\mu$ control region is only sensitive to the $t\bar{t}$ background. The statistical uncertainties are also shown.

Reducible background yields for 4μ and $2e2\mu$ in reference control region				
Control region	$Zb\bar{b}$	Z+light-flavor jets	Total Z+jets	$t\bar{t}$
Combined fit	159 ± 20	49 ± 10	208 ± 22	210 ± 12
Inverted impact parameter			206 ± 18	208 ± 23
Inverted isolation			210 ± 21	201 ± 24
$e\mu + \mu\mu$			-	201 ± 12
Same-sign dilepton			198 ± 20	196 ± 22

The estimated yields in the reference control region are extrapolated to the signal region by multiplying each background component by the probability of satisfying the isolation and impact parameter significance requirements, estimated from the relevant simulated sample. The systematic uncertainty in these transfer factors, stemming mostly from the size of the simulated data sample, is 6% for $Zb\bar{b}$, 60% for $Z+$ light-flavor jets and 16% for $t\bar{t}$. Furthermore, these simulation-based efficiencies are validated with data using muons accompanying $Z \rightarrow \ell\ell$ candidates, where the

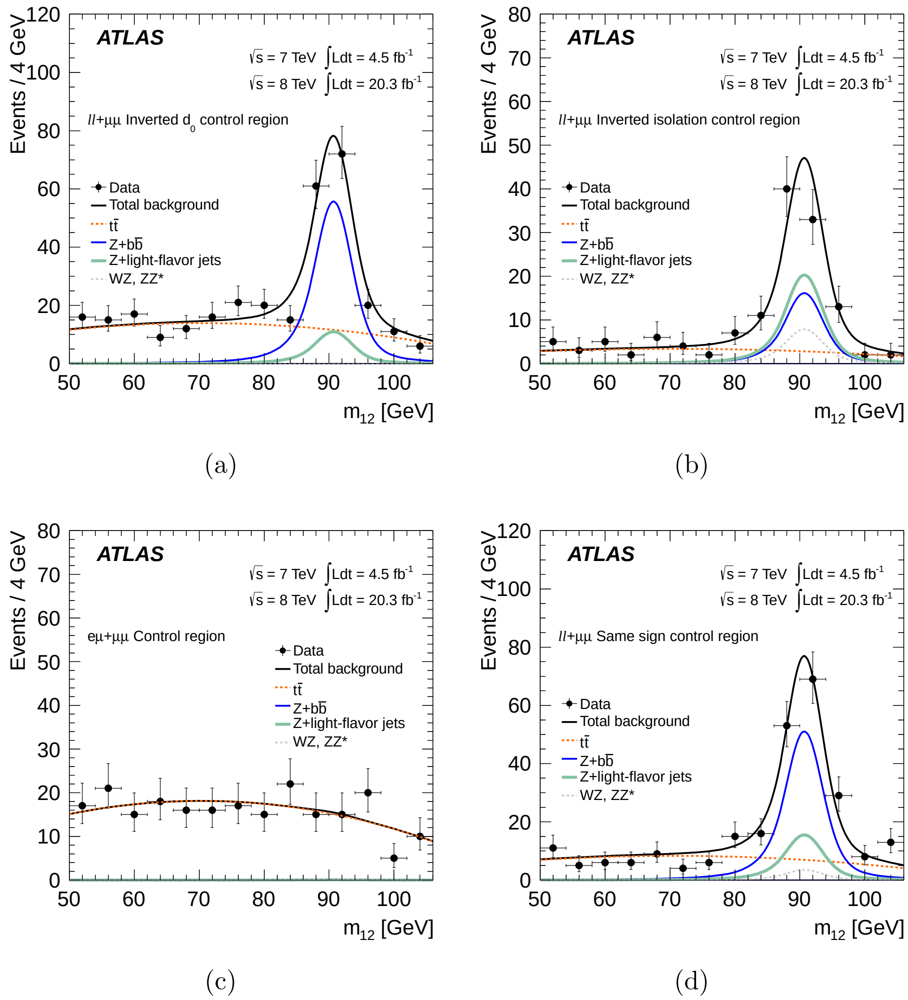

Figure 5.3. The observed m_{12} distributions (filled circles) and the results of the maximum likelihood fit are presented for the four control regions: (a) inverted requirement on impact parameter significance, (b) inverted requirement on isolation, (c) $e\mu$ leading dilepton, where the backgrounds besides $t\bar{t}$ are small and not visible, and (d) same-sign subleading dilepton. The fit results are shown for the total background (black line) as well as the individual components: $Z+$ jets decomposed into $Z + b\bar{b}$ (blue line) and Z+light-flavor jets (green line), $t\bar{t}$ (dashed red line), and the combined WZ and ZZ (dashed gray line), where the WZ and ZZ contributions are estimated from simulation.

leptons composing the Z boson candidate are required to satisfy isolation and impact parameter criteria. Events with four leptons, or with an opposite-sign dimuon with mass less than 5 GeV are excluded. Based on the data/simulation agreement of the efficiencies in this control region an additional systematic uncertainty of 1.6% is added. Figure 5.4 shows the relative difference between the ID and MS p_T measurements for combined muons for a subset of the $Z + X$ control region where the X represents a single combined muon. The contribution from π/K in-flight decays is clearly visible (the bump right to the peak on the plot) and well-described by the simulation.

The reducible background estimates in the signal region are given in Table 5.2.3, separately for the $\sqrt{s} = 7$ TeV and 8 TeV data. The uncertainties are separated into statistical and systematic contributions, where in the latter the transfer factor uncertainty and the fit systematic uncertainties are included.

5.2.4. Background $\ell\ell + ee$

The background for subleading electron pairs arises from jets misidentified as electrons. The background is classified into three distinct sources: light-flavor jets (f), photon conversions (γ) and heavy-flavor semileptonic decays (q), which are identified exactly in simulated background events. In addition, corresponding data control regions are defined which are enriched in events associated with each of these sources, thus allowing data-driven classification of reconstructed events into matching categories. For the background estimation, two types of control regions are defined:

1. the first, denoted as $3\ell + X$, in which the identification requirements for the lower-pT electron of the subleading pair are relaxed;
2. the second, denoted as $\ell\ell + XX$, comes in two variants: one in which the identification requirements for both electrons of the subleading pair are relaxed,

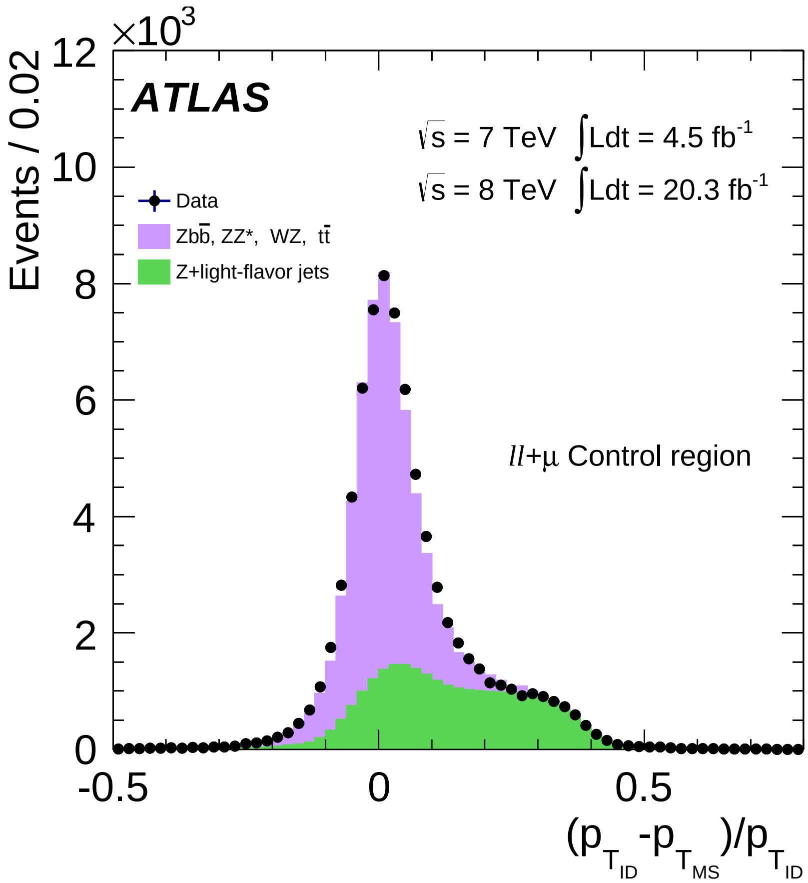

Figure 5.4. The distribution of the difference between the transverse momentum measured in the ID and in the MS normalized to the ID measurement, $(p_{T_{ID}} p_{T_{MS}})/p_{T_{ID}}$, for combined muons accompanying a $Z \to \ell\ell$ candidate. The data (filled circles) are compared to the background simulation (filled histograms) which has the Z+light-flavor background shown separately to distinguish the contribution from π/K in-flight decays. The additional muon is selected to be a combined muon with $p_T > 6$ GeV, which fulfills the δR requirement for the lepton separation of the analysis and in the case of $Z(\to \mu^+\mu^-)+\mu$ final state, the opposite sign pairs are required to have $m_{\mu^+\mu^-} > 5$ GeV to remove J/Ψ decays.

Table 5.3. Estimates for the $\ell\ell + \mu\mu$ background in the signal region for the full m_{4l} mass range for the $\sqrt{s} = 7$ TeV and $\sqrt{s} = 8$ TeV data. The Z+jets and $t\bar{t}$ background estimates are data-driven and the WZ contribution is from simulation. The decomposition of the Z+jets background in terms of the $Zb\bar{b}$ and the Z+light-flavor-jets contributions is also provided.

Background	4μ	$2e2\mu$
	$\sqrt{s} = 7$ TeV	
Z+jets	0.42 ± 0.21(stat)± 0.08(syst)	0.29 ± 0.14(stat)± 0.05(syst)
$t\bar{t}$	0.081 ± 0.016(stat)± 0.021(syst)	0.056 ± 0.011(stat)± 0.015(syst)
WZ expectation	0.08 ± 0.05	0.19 ± 0.10
	Z+jets decomposition	
$Zb\bar{b}$	0.36 ± 0.19(stat)± 0.07(syst)	0.25 ± 0.13(stat)± 0.05(syst)
Z+light-flavor jets	0.06 ± 0.08(stat)± 0.04(syst)	0.04 ± 0.06(stat)± 0.02(syst)
	$\sqrt{s} = 8$ TeV	
Z+jets	2.11 ± 0.46(stat)± 0.43(syst)	2.58 ± 0.39(stat)± 0.43(syst)
$t\bar{t}$	0.51 ± 0.03(stat)± 0.09(syst)	0.48 ± 0.03(stat)± 0.08(syst)
WZ expectation	0.42 ± 0.07	0.44 ± 0.06
	Z+jets decomposition	
$Zb\bar{b}$	2.30 ± 0.26(stat)± 0.14(syst)	2.01 ± 0.23(stat)± 0.13(syst)
Z+lingt-flavor jets	0.18 ± 0.38(stat)± 0.41(syst)	0.57 ± 0.31(stat)± 0.41(syst)

and another in which an inverted selection is applied to the subleading pair.

In both cases, the leading pair satisfies the complete event selection. The final background estimate is obtained from the $3\ell + X$ region, while the estimates from the $\ell\ell + XX$ region are used as cross-checks.

The efficiencies needed to extrapolate the different background sources from the control regions into the signal region are obtained separately for each of the f, γ, q background sources, in p_T and η bins, from simulation. These simulation-based efficiencies are corrected to correspond to the efficiency measured in data using a third type of control region, denoted as $Z+X$, enhanced for each X component. The $Z + X$ control region has a leading lepton pair, compatible with the decay of a Z boson, passing the full event selection and an additional object (X) that satisfies the relaxed identification for the specific control region to be extrapolated. The $Z + X$ data sample is significantly larger than the background control data samples. For all of the methods, the extrapolation from the background control region, $3\ell + X$ or $\ell\ell + XX$, to the signal region cannot be done directly with the efficiencies from the $Z + X$ data control region due to differences in the relative compositions of f, γ, q for the X of the two control regions. In the following, the q contribution in the simulation is increased by a factor of 1.4 to match the data.

5.2.4.1. Background estimation from $3\ell + X$

This method uses the $3\ell+X$ data control region with one loosely identified lepton for normalization. The control region is then fit using templates derived from simulation to determine the composition in terms of the three background sources f, γ, q, and these components are extrapolated individually to the signal region using the efficiency from the $Z + X$ control region.

The background estimation from the $3\ell+X$ region uses data that has quadruplets built as for the full analysis, with the exception that the full selection is applied to only the three highest-p_T leptons. Relaxed requirements are applied to the lowest-p_T electron: only a track with a minimum number of silicon hits that matches a cluster is required and the electron identification and isolation/impact parameter significance selection criteria are not applied. In addition, the subleading electron pair is required to have the same sign for both charges (SS) to minimize the contribution from the ZZ^* background. A residual ZZ^* component with a magnitude of 5% of the background estimate survives the SS selection and is subtracted to get the final estimate.

By requiring only a single electron with relaxed selection, the composition of the control region is simplified when compared with the other $\ell\ell+XX$ control regions, and the yields of the different background components can be extracted with a two-dimensional fit. Two variables, the number of hits in the innermost layer of the pixel detector ($n_{hits}^{B-layer}$) and the ratio of the number of high-threshold to low-threshold TRT hits (r_{TRT}), allow the separation of the f, γ and q components, since most photons convert after the innermost pixel layer, and hadrons faking electrons have a lower r_{TRT} compared to conversions and heavy-flavor electrons. Templates for the fit are taken from the $Z+X$ simulation after applying corrections from data.

The results of the fit are shown in Figure 5.5, for the $2\mu 2e$ and $4e$ channels combined. The *sPlot* method [50] is used to unfold the contributions from the different background sources as a function of electron p_T. The background estimates for the f, γ and q components in the control region, averaged over the $2\mu 2e$ and $4e$ channels, are summarized in Table 5.2.4.1.

To extrapolate the f, γ and q components from the $3\ell+X$ control region to the signal region, the efficiency for the different components to satisfy all selection criteria

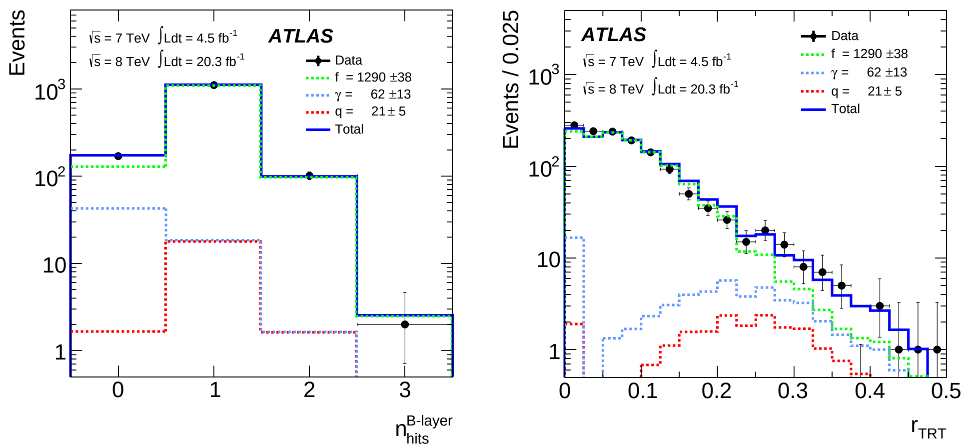

Figure 5.5. The results of a simultaneous fit to (a) $n_{hits}^{B-layer}$, the number of hits in the innermost pixel layer, and (b) r_{TRT}, the ratio of the number of high-threshold to low-threshold TRT hits, for the background components in the $3l + X$ control region. The fit is performed separately for the $2\mu 2e$ and $4e$ channels and summed together in the present plots. The data are represented by the filled circles. The sources of background electrons are denoted as: light-flavor jets faking an electron (f, green dashed histogram), photon conversions (γ, blue dashed histogram) and electrons from heavy-flavor quark semileptonic decays (q, red dashed histogram). The total background is given by the solid blue histogram.

Table 5.4. The fit results for the $3l+X$ control region, the extrapolation factors and the signal region yields for the reducible $\ell\ell$ + ee background. The second column gives the fit yield of each component in the $3l+X$ control region. The corresponding extrapolation efficiency and signal region yield are in the next two columns. The background values represent the sum of the $2\mu 2e$ and $4e$ channels. The uncertainties are the combination of the statistical and systematic uncertainties.

$2\mu 2e$ and $4e$		$\sqrt{s}=7$ TeV data	
Type	Fit yield in CR	Extrapolation factor	Yield in SR
f	391 ± 29	0.010 ± 0.001	3.9 ± 0.9
γ	19 ± 9	0.10 ± 0.02	2.0 ± 1.0
q	5.1 ± 1.0	0.100.03	0.510.15
$2\mu 2e$ and $4e$		$\sqrt{s}=8$ TeV data	
Type	Fit yield in CR	Extrapolation factor	Yield in SR
f	894 ± 44	0.0034 ± 0.0004	3.1 ± 1.0
γ	48 ± 15	0.024 ± 0.004	1.1 ± 0.6
q	18.3 ± 3.6	0.10 ± 0.02	1.8 ± 0.5

is obtained from the $Z + X$ simulation. As previously mentioned, the simulation efficiency for each component is corrected by comparing with data using the $Z + X$ control region with an adjusted selection to enrich it for each specific component. For the f component, the simulation efficiency is corrected by a factor between 1.6 and 2.5, rising with increasing p_T. The simulation is found to model well the efficiency of the γ component, to within approximately 10%. For the q component, the efficiency is found to be modeled well by simulation, but there is an additional correction, obtained from simulation, to estimate the number of background opposite-sign (OS) events from the number of SS events, which is $OS/SS \sim 1.7$. The systematic uncertainty is dominated by these simulation efficiency corrections, corresponding to 30%, 20%, 25% uncertainties for f, γ, q, respectively. The extrapolation efficiency and signal yields are also given in Table 5.2.4.1. After removing the residual ZZ^* background ($\sim$ 5%), the final results for the $2\mu 2e$ and $4e$ reducible backgrounds are given in Table 5.2.4.1.

5.2.4.2. Background estimation from the $\ell\ell + XX$ region using the transfer-factor method

The transfer-factor method starts from the $\ell\ell$+XX control region in data with two leptons with inverted selection requirements. Using the predicted sample composition from simulation, two approaches are taken to obtain transfer factors: one using the $Z + X$ simulation corrected by data, and the other using the $Z + X$ data control region that is enriched to obtain a q component matching that of the $\ell\ell$+XX control region.

The $\ell\ell + XX$ data control region has relaxed electron likelihood identification on the X pair and requires each X to fail one selection among the full electron identification, isolation and impact parameter significance selections, leading to a sample of around 700 events for each of the $2\mu + XX$ and $2e + XX$ channels. The

Table 5.5. Summary of the $\ell\ell + ee$ data-driven background estimates for the $\sqrt{s}$ = 7 TeV and $\sqrt{s}$ = 8 TeV data for the full $m_{4\ell}$ mass range. OS (SS) stands for opposite (same) sign lepton pairs. The "†" symbol indicates the estimates used for the background normalization; the other estimates are used as cross-checks. The first uncertainty is statistical, while the second is systematic. The SS data full analysis is limited to the region with $m_{4\ell}$ below 160 GeV to avoid a ZZ contribution; this region contains 70% of the expected background.

Method	$\sqrt{s} = 7$ TeV data	$\sqrt{s} = 8$ TeV data
	$2\mu 2e$	
$3\ell + X$†	$2.9 \pm 0.5 \pm 0.5$	$2.91 \pm 0.33 \pm 0.60$
$\ell\ell + XX$ Transfer Factor	$2.24 \pm 0.34 \pm 1.06$	$2.52 \pm 0.10 \pm 0.90$
$\ell\ell + XX$ Transfer Factor b-enriched	$2.8 \pm 0.5 \pm 0.8$	$3.17 \pm 0.17 \pm 0.91$
$\ell\ell + XX$ Recotruth	$2.79 \pm 0.36 \pm 1.05$	$2.9 \pm 0.3 \pm 0.3$
$2\mu 2e$ SS data full analysis	1	2
	$4e$	
$3\ell + X$†	$3.3 \pm 0.5 \pm 0.5$	$2.88 \pm 0.28 \pm 0.54$
$\ell\ell + XX$ Transfer Factor	$2.05 \pm 0.31 \pm 0.93$	$2.45 \pm 0.10 \pm 0.89$
$\ell\ell + XX$ Transfer Factor b-enriched	$3.4 \pm 0.9 \pm 0.8$	$2.89 \pm 0.18 \pm 0.75$
$\ell\ell + XX$ Recotruth	$2.61 \pm 0.35 \pm 0.91$	$2.8 \pm 0.3 \pm 0.3$
$4e$ SS data full analysis	2	2

inverted selection removes most of the ZZ^* background from the control region as well as the Higgs signal. The main challenge is to correctly estimate the extrapolation efficiency, or transfer factor, from the $\ell\ell+XX$ control region to the signal region using the $Z+X$ sample, since the background composition of f, γ and q is different for the $Z+X$ and $\ell\ell+XX$ control regions and each of their extrapolation efficiencies is significantly different.

In order to aid in the understanding of the control region composition and to improve the uncertainty on the estimate of the extrapolation to the signal region, each X is assigned to one of two reconstruction categories: electron-like (E) or fake-like (F), for both data and simulation. For the E category, a selection is applied to enhance the electron content, and the remaining X fall into the F category. For the $\ell\ell+XX$ control region, the composition of X in terms of the background source is balanced between fakes (f) and electrons (γ,q) for the E category corresponding to component fractions of 50% f, 20% γ and, 30% q, and is dominated by fakes for the F category with 92% f, 5% γ and 3% q.

The two approaches taken to estimate the background from the $\ell\ell+XX$ data control region differ in the way they estimate the extrapolation to the signal region with $Z+X$ events. Both approaches separate XX into the four reconstruction categories: EE, EF, FE and FF. The first approach uses the $Z+X$ simulation to determine the transfer factors for X in bins of p_T and η, where the extrapolation efficiency of each background component of the $\ell\ell+XX$ simulation is combined according to the composition seen in the $\ell\ell+XX$ simulation. In addition, the simulation extrapolation efficiency is corrected to agree with data as previously described in Section 5.2.4.1. For the background estimate, the transfer factors are applied to the $\ell\ell+XX$ data control region, accounting for the inverted selection. The result is corrected by subtracting a small residual ZZ^* contribution, and including a WZ contribution that is removed by the inverted selection on the XX; both are estimated with simulation. The background estimate with the transfer-factor method is given in Table 5.2.4.1.

The second approach differs in the manner in which the background composition of the $Z+X$ control region is brought into agreement with the $\ell\ell+XX$ control region. The most important difference lies in the heavy-flavor component fraction, which is three times larger in the $\ell\ell+XX$ control region and has a significantly larger transfer factor than either the f or γ backgrounds. This approach modifies the composition of the $Z+X$ data control region by requiring a b-jet in each event. By tuning the selection of a multivariate b-tagger, the q and f composition of the $Z+X$ control region can be brought into agreement with that of the $ll+XX$ control region to the level of 5-10%, as seen with simulation. The transfer factors are extracted from the $Z+X$ data control region and applied in bins of p_T and η as for the other approach, and the systematic uncertainty is estimated in part by varying the operating point used for the multivariate b-tagger. Finally, the WZ contribution is accounted for with simulation, as previously. The background estimate from the transfer factors based on b-enriched samples is given in Table 5.2.4.1.

Other method e.g. Reco-truth unfolding method please see Appedix A.4.

5.2.4.3. Summary of reducible background estimates for $\ell\ell+ee$

The summary of the reducible backgrounds for the $\ell\ell+ee$ final states is given for the full mass region in Table 5.2.4.1. In addition to the previously discussed methods, the results are presented for the full analysis applied to $\ell\ell+ee$ events in data where the subleading ee pair is required to have the same-sign charge, and $m_{4\ell}$ is required to be below 160 GeV to avoid a ZZ contribution; the region with $m_{4\ell} < 160$ GeV contains 70% of the expected reducible backgrounds. Although limited in statistical precision, this agrees well with the other estimates.

5.2.5. Shape of the reducible background contributions

The $m_{4\ell}$ distributions of the reducible backgrounds are required for the normalization and shape of these backgrounds in the mass fit region, discussed below. The shape of the distribution for the $\ell\ell+\mu\mu$ background is taken from simulation and the uncertainty comes from varying the track isolation and impact parameter significance selections. The corresponding distribution for the $\ell\ell+ee$ background comes from the $3\ell+X$ sample, after reweighting with the transfer factor to match the kinematics of the signal region. The uncertainty in the $\ell\ell+ee$ background shape is taken as the difference between the shapes obtained from the control regions of the two other methods: transfer factor and recotruth. The estimates in the $120 < m_{4\ell} < 130$ GeV mass window are provided in Table **??**. Figure 5.6 presents the m_{12} and m_{34} distributions for the $\ell\ell+\mu\mu$ and $\ell\ell+ee$ control regions where the full selection has been applied except for subleading lepton impact parameter significance and isolation requirements, which are not applied. Good agreement is seen between the data and the sum of the various background estimates. The shape of the background in the $m_{4\ell}$ distribution extrapolated to the signal region can be seen in Figure **??**.

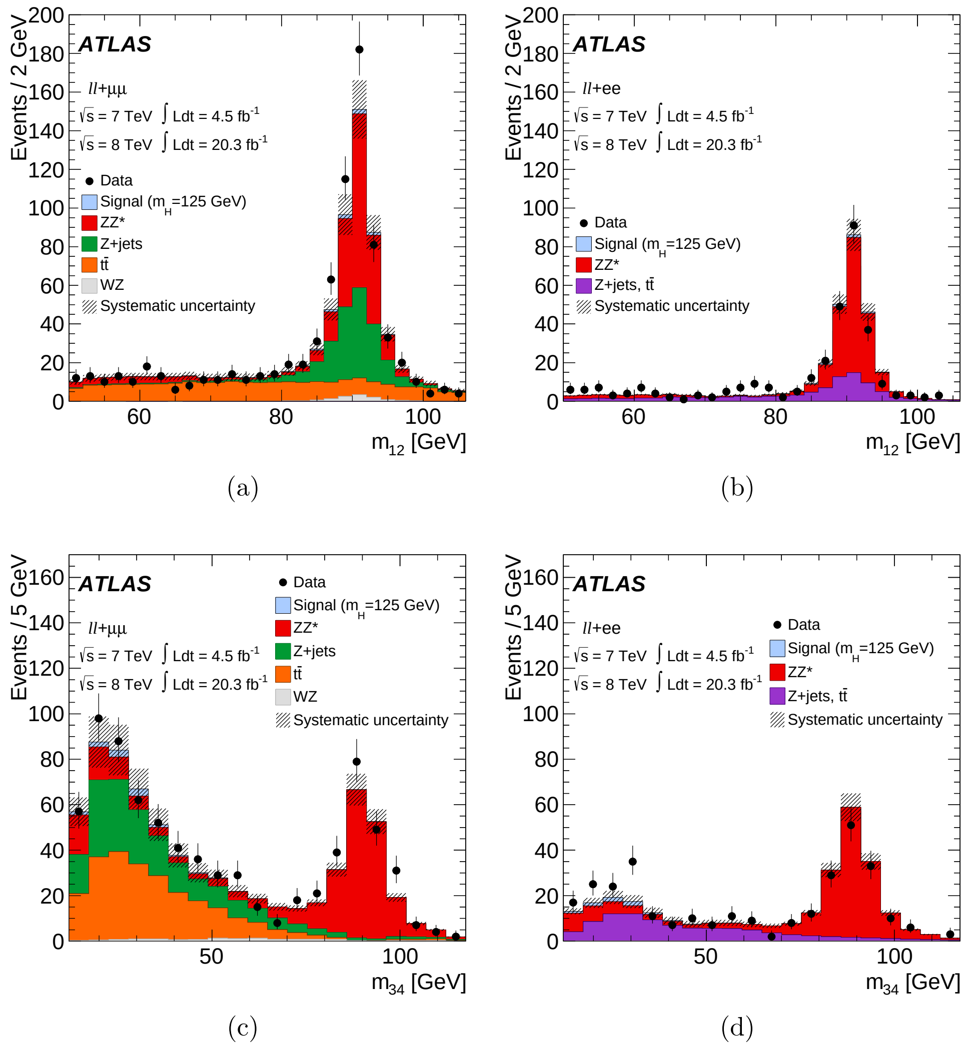

Figure 5.6. Invariant mass distributions of the lepton pairs in the control sample defined by a Z boson candidate and an additional same-flavor lepton pair, including all signal and background contributions, for the $\sqrt{s}$ = 7 TeV and $\sqrt{s}$ = 8 TeV datasets. The sample is divided according to the flavor of the additional lepton pair. In (a) and (c) the m_{12} and m_{34} distributions are presented for $\ell\ell + \mu^+\mu$ events, where $\ell\ell$ is $\mu^+\mu$ or e^+e. In (b) and (d) the m_{12} and m_34 distributions are presented for $\ell\ell + e^+e$ events. The data are shown as filled circles and the different backgrounds as filled histograms with the total background systematic uncertainty represented by the hatched areas. The kinematic selection of the analysis is applied. Isolation and impact parameter significance requirements are applied to the first lepton pair only. The simulation is normalized to the data-driven background estimates.

Chapter 6

Production Rate and Mass of a New Heavy Boson

As discused in previous chapters, the Higgs boson is expected to decay to four leptons, $H \to ZZ^* \to 4\ell$, where $\ell = e$ or μ. This channel provides good sensitivity for the measurement of the Higgs boson properties due to its high signal-to-background ratio, which (based on simulation) is about 2 for each of the four final states: $\mu^+\mu^-\mu^+\mu^-(4\mu)$, $e^+e^-\mu^+\mu^-(2e2\mu)$, $\mu^+\mu{-}e^+e^-(2\mu 2e)$, and $e^+e^-e^+e^-(4e)$, where the first lepton pair is defined to be the one with the dilepton invariant mass closest to the Z boson mass. The largest background in this search comes from continuum $(Z^{(*)}/\gamma^*)(Z^{(*)}/\gamma^*)$ production, referred to as ZZ^* hereafter. For the four-lepton events with an invariant mass, $m_{4\ell}$, below about 160 GeV, there are also important background contributions from Z+jets and $t\bar{t}$ production with two prompt leptons, where the additional charged lepton candidates arise from decays of hadrons with b- or c-quark content, from photon conversions or from misidentification of jets.

6.1. Signal and background yield

The number of observed candidate events for each of the four decay channels in a mass window of 120-130 GeV as well as the signal and background expectations are presented in Table 6.1. The signal and ZZ^* background expectations are normalized to the SM expectation while the reducible background is normalized to the data-driven estimate described in Chapter 5. Three events in the mass range $120 < m_{4\ell} < 130$ GeV are corrected for FSR: one 4μ event and one $2\mu 2e$ are corrected for non-collinear FSR, and one $2\mu 2e$ event is corrected for collinear FSR. In the full mass spectrum, there are 8 (2) events corrected for collinear (non-collinear) FSR, in good agreement with the expected number of 11 events.

The expected $m_{4\ell}$ distribution for the backgrounds and the signal hypothesis are compared with the combined $\sqrt{s} = 7$ TeV and $\sqrt{s} = 8$ TeV data in Figure 6.1(a) for the $m_{4\ell}$ range 80-170 GeV, and in Figure 6.1(b) for the invariant mass range 80-600 GeV. In Figure 6.1 one observes the single $Z \rightarrow 4\ell$ resonance[14], the threshold of the ZZ production above 180 GeV and a narrow peak around 125 GeV. Figure 6.2 shows the distribution of the m_{12} versus m_{34} invariant masses, as well as their projections, for the candidates with $m_{4\ell}$ within 120-130 GeV. The $Z-$mass constrained kinematic fit is not applied for these distributions. The Higgs signal is shown for $m_H = 125$ GeV with a value of $\mu = 1.51$, corresponding to the combined μ[1] measurement for the $H \rightarrow ZZ^* \rightarrow 4\ell$ final state, scaled to this mass by the expected variation in the SM Higgs boson cross section times branching ratio.

6.2. Background ZZ^*

The distribution of the BDT_{ZZ*} output[2] versus $m_{4\ell}$ is shown in Figure 6.3(a) for the reconstructed candidates with $m_{4\ell}$ within the fitted mass range 110-140 GeV. An excess of events with $\mathrm{high} - \mathrm{BDT}_{ZZ*}$ output is present for values of $m_{4\ell}$ close to 125 GeV, compatible with the Higgs signal hypothesis at that mass. The compatibility of the data with the expectations shown in Figure 6.3(a) is checked using pseudo-experiments generated according to the expected two-dimensional distribution and good agreement is found. Figure 6.3(b) shows the distribution of the BDT_{ZZ*} output for the candidates in the $m_{4\ell}$ range 120-130 GeV compared with signal and back-

[1]The global signal strength factor μ is the parameter of interest which scales the total number of signal events predicted by the Standard Model. This factor is defined such that $\mu = 0$ corresponds to the background-only hypothesis and $\mu = 1$ corresponds to the SM Higgs boson signal in addition to the background.

[2]BDT_{ZZ*} output is BDT training output

Table 6.1. The number of events expected and observed for a $m_H = 125$ GeV hypothesis for the four-lepton final states in a window of $120 < m_{4\ell} < 130$GeV. The second column shows the number of expected signal events for the full mass range, without a selection on $m_{4\ell}$. The other columns show for the 120130 GeV mass range the number of expected signal events, the number of expected ZZ^* and reducible background events, the signal-to-background ratio (S/B), together with the number of observed events, for 4.5 fb^{-1} at $\sqrt{s} = 7$ TeV and 20.3 fb^{-1} at $\sqrt{s} = 8$ TeV as well as for the combined sample.

Final state	Sginal full mass range	Signal	$ZZ*$	Z+jets,$t\bar{t}$	S/B	Expected	Observed
			$\sqrt{s} = 7$ TeV				
4μ	1.00 ± 0.10	0.91 ± 0.09	0.46 ± 0.02	0.10 ± 0.04	1.7	1.47 ± 0.10	2
$2e2\mu$	0.66 ± 0.06	0.58 ± 0.06	0.32 ± 0.02	0.09 ± 0.03	1.5	0.99 ± 0.07	2
$2\mu2e$	0.50 ± 0.05	0.44 ± 0.04	0.21 ± 0.01	0.36 ± 0.08	0.8	1.01 ± 0.09	1
$4e$	0.46 ± 0.05	0.39 ± 0.04	0.19 ± 0.01	0.40 ± 0.09	0.7	0.98 ± 0.10	1
Total	2.62 ± 0.26	2.32 ± 0.23	1.17 ± 0.06	0.96 ± 0.18	1.1	4.45 ± 0.30	6
			$\sqrt{s} = 8$ TeV				
4μ	5.80 ± 0.57	5.28 ± 0.52	2.36 ± 0.12	0.69 ± 0.13	1.7	8.33 ± 0.6	12
$2e2\mu$	3.92 ± 0.39	3.45 ± 0.34	1.67 ± 0.08	0.60 ± 0.10	1.5	5.72 ± 0.37	7
$2\mu2e$	3.06 ± 0.31	2.71 ± 0.28	1.17 ± 0.07	0.36 ± 0.08	1.8	4.23 ± 0.30	5
$4e$	2.79 ± 0.29	2.38 ± 0.25	1.03 ± 0.07	0.35 ± 0.07	1.7	3.77 ± 0.27	7
Total	15.6 ± 1.6	13.8 ± 1.4	6.24 ± 0.34	2.00 ± 0.28	1.7	22.1 ± 1.5	31
			$\sqrt{s} = 7$ TeV and $\sqrt{s} = 8$ TeV				
4μ	6.80 ± 0.67	6.20 ± 0.61	2.82 ± 0.14	0.79 ± 0.13	1.7	9.81 ± 0.64	14
$2e2\mu$	4.58 ± 0.45	4.04 ± 0.40	1.99 ± 0.10	0.69 ± 0.11	1.5	6.72 ± 0.42	9
$2\mu2e$	3.56 ± 0.36	3.15 ± 0.32	1.38 ± 0.08	0.72 ± 0.12	1.5	5.24 ± 0.35	6
$4e$	3.25 ± 0.34	2.77 ± 0.29	1.22 ± 0.29	0.76 ± 0.11	1.4	4.75 ± 0.32	8
Total	18.2 ± 1.8	16.2 ± 1.6	7.41 ± 0.40	2.95 ± 0.33	1.6	26.5 ± 1.7	37

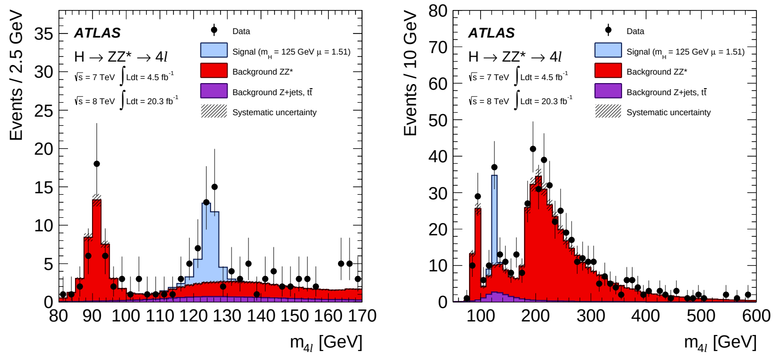

(a) (b)

Figure 6.1. The distribution of the four-lepton invariant mass, $m_{4\ell}$, for the selected candidates (filled circles) compared to the expected signal and background contributions (filled histograms) for the combined $\sqrt{s} = 7$ TeV and $\sqrt{s} = 8$ TeV data for the mass ranges: (a) 80-170 GeV, and (b) 80-600 GeV. The signal expectation shown is for a mass hypothesis of $m_H = 125$ GeV and normalized to $\mu = 1.51$ (see text). The expected backgrounds are shown separately for the ZZ^* (red histogram), and the reducible Z+jets and $t\bar{t}$ backgrounds (violet histogram); the systematic uncertainty associated to the total background contribution is represented by the hatched areas.

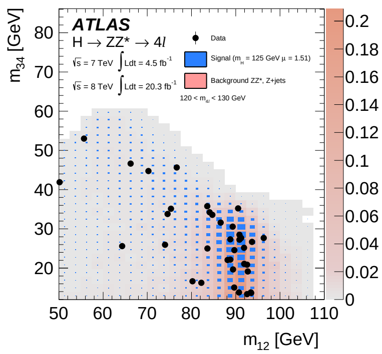

(a)

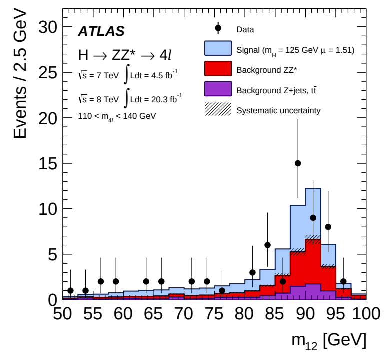

(b)

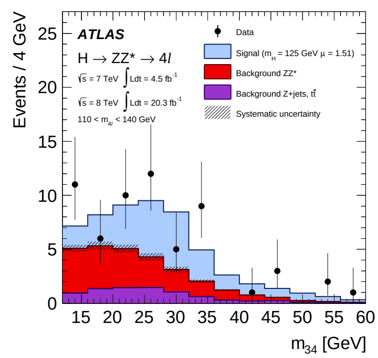

(c)

Figure 6.2. Distributions of data (filled circles) and the expected signal and backgrounds events in (a) the m_{34} m_{12} plane with the requirement of $m_{4\ell}$ in 120130 GeV. The projected distributions for (b) m_{12} and (c) m_{34} are shown for $m_{4\ell}$ in 110140 GeV, the fit range. The signal contribution is shown for $m_H = 125$ GeV and normalized to $\mu = 1.51$ (see text) as blue histograms in (b) and (c). The expected background contributions, ZZ^* (red histogram) and Z+jets plus $t\bar{t}$ (violet histogram), are shown in (b) and (c); the systematic uncertainty associated to the total background contribution is represented by the hatched areas. The expected distributions of the Higgs signal (blue) and total background (red) are superimposed in (a), where the box size (signal) and color shading (background) represent the relative density. In every case, the combination of the 7 TeV and 8 TeV results is shown.

ground expectations. In Figure 6.3(c) the distribution of the invariant mass of the four leptons is presented for candidates satisfying the requirement that the value of the BDT_{ZZ*} output be greater than zero, which maximizes the expected significance for a SM Higgs boson with a mass of about 125 GeV.

The local p_0-value[51][3] of the observed signal, representing the significance of the excess relative to the background-only hypothesis, is obtained with the asymptotic approximation [29] using the 2D fit without any selection on BDT_{ZZ*} and is shown as a function of m_H in Figure 6.4. The local p_0-value at the measured mass for this channel, 124.51 GeV (see below), is 8.2 standard deviations. At the value of the Higgs boson mass, $m_H = 125.36$ GeV, obtained from the combination of the $H \rightarrow ZZ^* \rightarrow 4\ell$ and $H \rightarrow \gamma\gamma$ mass measurements [7], the local p_0-value decreases to 8.1 standard deviations. Signal strength μ is defined as the measured signal cross section divided by predicted signal cross section. The expected observed significance for $\mu = 1$ at these two masses is 5.8 and 6.2 standard deviations, respectively.

6.3. Mass and signal strength

The measured Higgs boson mass obtained with the baseline 2D method is $m_H = 124.51 \pm 0.52$ GeV [7]. The signal strength at this value for m_H is

$$\mu = 1.66 \begin{array}{c} +0.39 \\ -0.34 \end{array} (\mathrm{stat}) \begin{array}{c} +0.21 \\ -0.14 \end{array} (\mathrm{syst}). \tag{6.1}$$

The other methods of previous section, 1D and pre-event resolution, yield similar results for the Higgs boson mass [7]. Figure 6.5(a) shows the best fit values of μ and m_H as well as the profile likelihood ratio contours in the (m_H,μ) plane corresponding to the 68% and 95% confidence level intervals. Finally, the best fit value for m_H

[3]The p_0-value gives the probability that the experimental results observed can be caused by background only. The local p_0-value is the probability of the background fluctuating into the observed signal configuration with Higgs mass around 125 GeV.

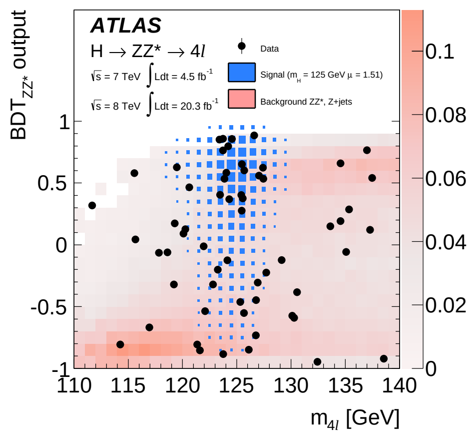

(a)

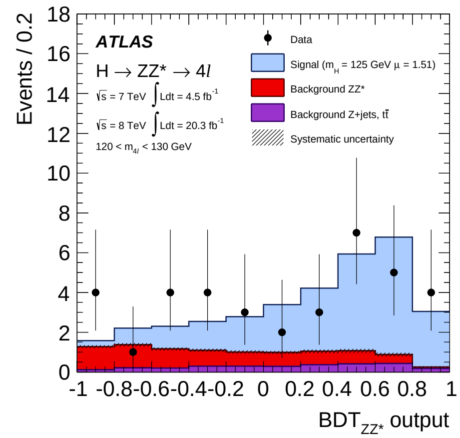

(b)

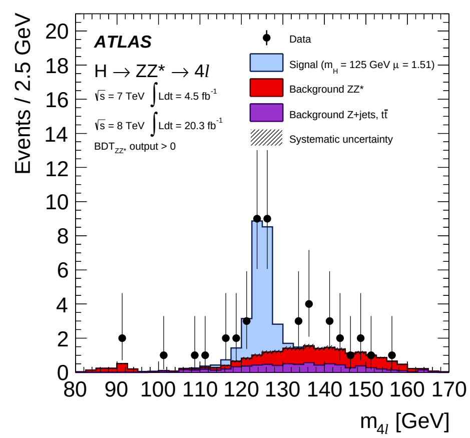

(c)

Figure 6.3. Distributions of data (filled circles) and the expected signal and background events in (a) the BDT$_{ZZ^*}$ $m_{4\ell}$ plane, (b) BDT$_{ZZ^*}$ with the restriction $120 < m_{4\ell} < 130$ GeV, and (c) $m_{4\ell}$ with the additional requirement that the BDT$_{ZZ^*}$ is positive. The expected Higgs signal contribution is shown for $m_H = 125$ GeV and normalized to $\mu = 1.51$ (see text) as blue histograms in (b) and (c). The expected background contributions, ZZ^* (red histogram) and Z+jets plus $t\bar{t}$(violet histogram), are shown in (b) and (c); the systematic uncertainty associated to the total background contribution is represented by the hatched areas. The expected distributions of the Higgs signal (blue) and total background (red) are superimposed in (a), where the box size (signal) and color shading (background) represent the relative density. In every case, the combination of the 7 TeV and 8 TeV results is shown.

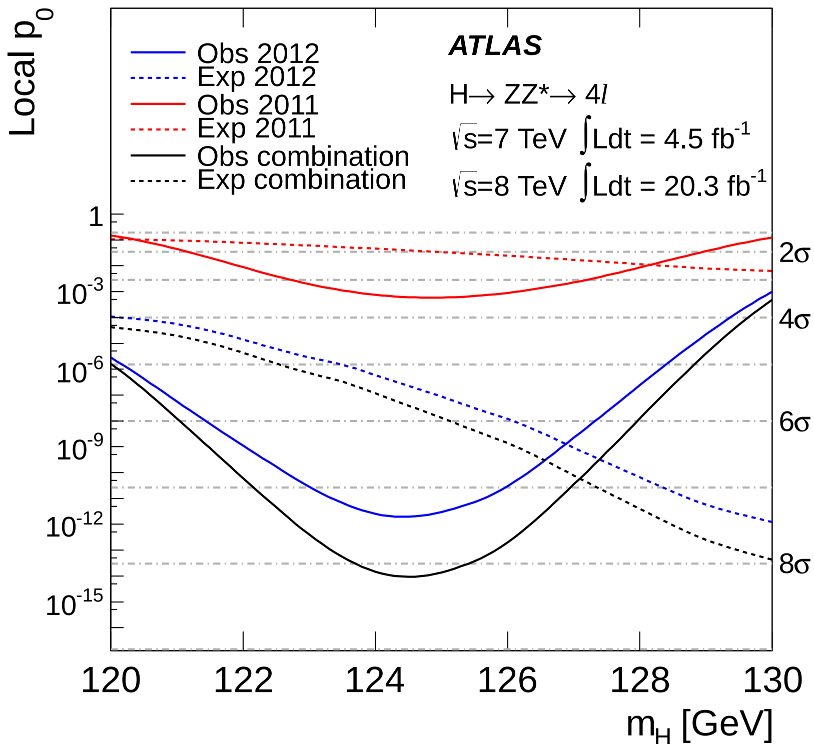

(a)

Figure 6.4. The observed local p_0-value for the combination of the 2011 and 2012 data sets (solid black line) as a function of m_H; the individual results for $\sqrt{s} = 7$TeV and 8TeV are shown separately as red and blue solid lines, respectively, The dashed curves show the expected median of the local p_0 for the signal hypothesis with signal strength $\mu = 1$, when evaluated at the corresponding m_H. The horizontal dot-dashed lines indicate the p_0 values corresponding to local significances of 1-8σ.

obtained using the model developed for the categorized analysis, is within 90 MeV of the value found with the inclusive 2D method.

At the combined ATLAS measured value of the Higgs boson mass, $m_H = 125.36$ GeV, the signal strength is found to be

$$\mu = 1.50 {}^{+0.35}_{-0.31} (\text{stat}) {}^{+0.19}_{-0.13} (\text{syst}). \tag{6.2}$$

The scan of the profile likelihood, $-2\ln\Lambda(\mu)$, can be used to get 1σ by the maximum value -1, as a function of the inclusive signal strength μ for each one of the four channels separately, as well as for their combination, is shown in Figure 6.5(b).

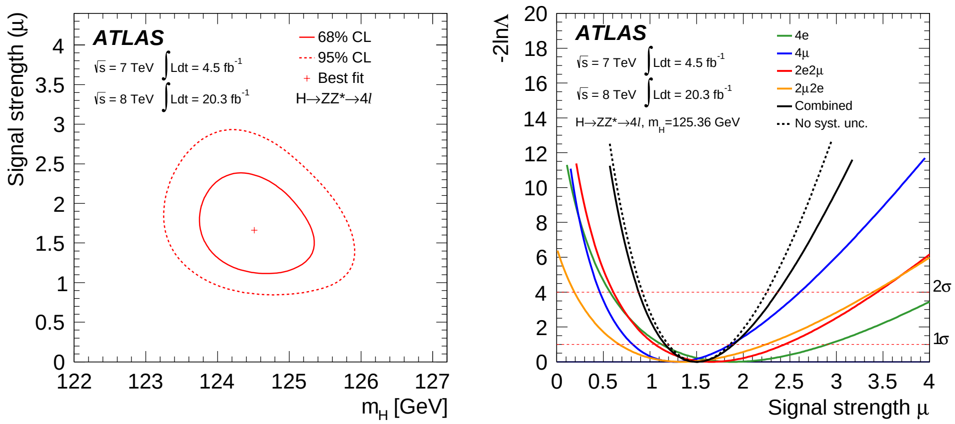

(a) (b)

Figure 6.5. (a) The 68% and 95% confidence level (CL) contours in the μ m_H plane for the inclusive analysis. (b) The profile likelihood as a function of the inclusive signal strength μ for the individual channels ($4e$, green line; 4μ, blue line; $2e2\mu$, red line; $2\mu2e$, yellow line) as well as for their combination (black lines); the scan for the combination of all channels is shown both with (solid line) and without (dashed line) systematic uncertainties. The value of m_H is fixed to 125.36 GeV while all the other nuisance parameters are profiled in the fit. In every case, the combination of the 7TeV and 8TeV results is shown.

Chapter 7

Spin-Parity Quantum Number Measurement of the New Boson

To establish the consistency of the new boson with the Higgs hypothesis, the spin-parity quantum numbers have to be measured. In this chapter, I will discuss the steps and methods of the measurement.

7.1. Modeling spin and parity states

In the current analysis the production and decay angles are defined in the following way:

- θ_1 and θ_2 are the angles between negative final state leptons and the direction of flight of their respective Z-bosons. The 4-vectors of leptons are calculated in the rest frame of the corresponding parent Z-bosons.
- ϕ is the angle between the decay planes of the four final state leptons expressed in the rest frame of the four-lepton system (X)
- ϕ_1 is the angle defined between the decay plane of the first lepton pair and a plane defined by the vector of Z_1 in the rest frame of the four-lepton system (X) and the positive direction of the collision axis.
- θ^* is the production angle of Z_1 defined in the rest frame of the four-lepton system (X) .

A general sketch illustrating these definitions is given in Fig. 7.1.

In this study, CP-even and CP-odd resonances with spins 0 and 2 (J^{CP} equal to 0^+, 0^+_h, 0^-, 2^+_m, where subscripts h and m denote beyond-standard (scalar with

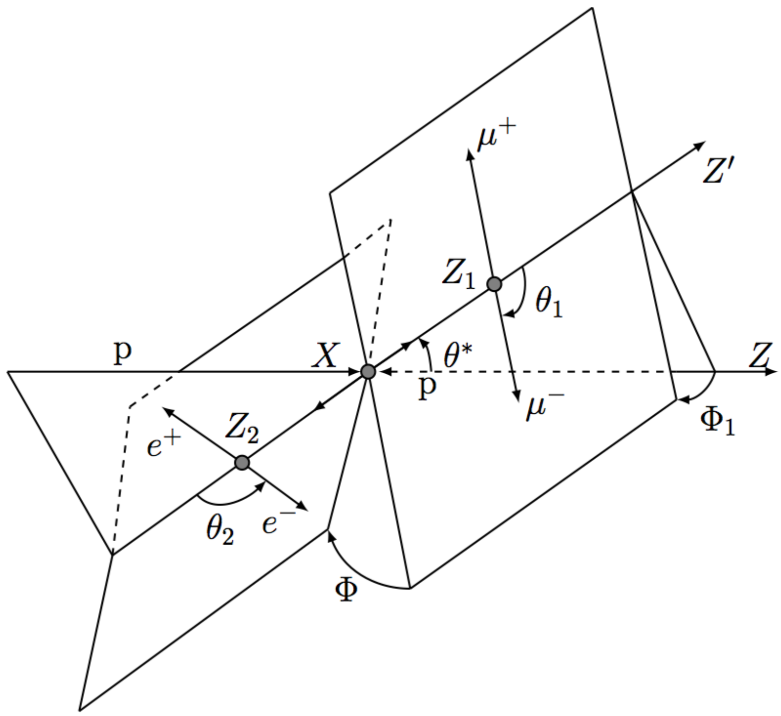

Figure 7.1. Definitions of production and decay angles in $X \to ZZ^{(*)} \to 4l$ decay [34].

higher-dimension operators) and minimal assumptions on the couplings, respectively) are considered[34, 35]. Spin-0 states with CP mixtures are also studied.

In hypothesis testing, the spin and parity hypotheses are tested in pairs. In each individual test, the likelihood of one model is compared relative to the likelihood of another model. In order to confirm that the observed resonance best matches the predictions corresponding to a SM Higgs boson (the null hypothesis) the goal of the analysis is to determine the level of exclusion of other well-motivated spin and parity hypotheses in favor of the 0^+ state. This is the first priority of the study. In the case such an exclusion is not found, a deeper look should be given to the alternate spin and parity state.

While the properties of spin-0 states are relatively well-defined [34], those of a spin-2 resonance are largely model-dependent. In the current study we address the most popular model for the latter spin hypothesis. The following sections contain more details on the information introduced here.

7.1.1. Scattering Amplitudes

For a generic Higgs-like resonance of spin zero, the scattering amplitude describing its interaction with the two Z bosons is composed of two terms:

$$A(X \to V_1 V_2) = v^{-1}[g_1 M_V^2 \varepsilon_1^* \varepsilon_2^* + g_2 f_{\mu\nu}^{*(1)} f^{*(2)\mu\nu} + g_3 f^{*(1)\mu\nu} f_{\mu\alpha}^{*(2)} \tfrac{q_\nu q^\alpha}{\Lambda^2} + g_4 f_{\mu\nu}^{*(1)} \tilde{f}^{*(2)\mu\nu}]. \tag{7.1}$$

Here, X represents the Higgs-like resonance, $V_{1,2}$ the two Z bosons, and the $g_{1,\ldots,4}$ are the effective coupling constants. The $f^{*(i)\mu\nu}$ denote the components of the field strength tensor of a gauge boson with momentum q_i. Λ is the scale at which physics beyond the Standard Model could appear. A SM Higgs is expected to have $g_1 = 1$ and all other coupling constants $g_{i\neq 1} = 0$, whereas a pseudo-scalar Higgs would have $g_4 = 1$. The model parameters used in the current analysis are shown in Table 7.1.1.

The most general amplitude of the decay of a spin-2 particle to two identical vector bosons contains 10 different terms and 10 effective coupling constants $g_{1,\ldots,10}$, which are in general complex numbers [34, 18]:

$$\begin{aligned}
&A(X \to V_1 V_2) = \Lambda^{-1} \Big[2 g_1 X_{\mu\nu} f^{*(1)\mu\alpha} f_\alpha^{*(2)\nu} \\
&+ 2 g_2 X_{\mu\nu} \frac{q_\alpha q_\beta}{\Lambda^2} f^{*(1)\mu\alpha} f^{*(2)\nu\beta} + g_3 \frac{\tilde{q}^\beta \tilde{q}^\alpha}{\Lambda^2} X_{\beta\nu} \left(f^{*(1)\mu\nu} f_{\mu\alpha}^{*(2)} + f^{*(2)\mu\nu} f_{\mu\alpha}^{*(1)} \right) \\
&+ g_4 \frac{\tilde{q}^\mu \tilde{q}^\nu}{\Lambda^2} X_{\mu\nu} f^{*(1)\alpha\beta} f_{\alpha\beta}^{*(2)} + m_V^2 X_{\mu\nu} \left(2 g_5 \epsilon_1^{*\mu} \epsilon_2^{*\nu} + 2 g_6 \frac{\tilde{q}^\mu q_\alpha}{\Lambda^2} (\epsilon_1^{*\nu} \epsilon_2^{*\alpha} - \epsilon_1^{*\alpha} \epsilon_2^{*\nu}) + g_7 \frac{\tilde{q}^\mu \tilde{q}^\nu}{\Lambda^2} (\epsilon_1^* \epsilon_2^*) \right) \\
&+ g_8 \frac{\tilde{q}^\mu \tilde{q}^\nu}{\Lambda^2} X_{\mu\nu} f^{*(1)\alpha\beta} \tilde{f}_{\alpha\beta}^{*(2)} + m_V^2 X_{\mu\alpha} \tilde{q}^\alpha \epsilon_{\mu\nu\rho\sigma} \left(g_9 \frac{q^\sigma}{\Lambda^2} \epsilon_1^{*\nu} \epsilon_2^{*\rho} + g_{10} \frac{q^\rho \tilde{q}^\sigma}{\Lambda^4} (\epsilon_1^{*\nu} (q \epsilon_2^*) + \epsilon_2^{*\nu} (q \epsilon_1^*)) \right) \Big] .
\end{aligned} \tag{7.2}$$

Here q, q_1 and q_2 denote the 4-momenta of the X particle and of vector bosons, respectively, and $\tilde{q} = q_1 - q_2$. m_V is the on-shell mass of a gauge boson, v is the vacuum expectation value and ϵ_X is the polarization vector of X. The field-strength tensor of the gauge boson with momentum q_i and polarization vector ϵ_i and the conjugate tensor are given by

$$f^{(i)\mu\nu} = \epsilon_i^\mu q_i^\nu - \epsilon_i^\nu q_i^\mu \qquad , \qquad \tilde{f}_{\mu\nu}^{(i)} = \epsilon_{\mu\nu\alpha\beta} \epsilon_i^\alpha q_i^\beta . \tag{7.3}$$

The X resonance wave function is given by a symmetric traceless tensor $X_{\mu\nu}$. The coupling constants $g_{1..7}$ correspond to the decay of a 2^+ particle and $g_{8..10}$ to the decay of a 2^- particle. In addition, both groups can contribute to the same amplitude, and CP-mixing is possible.

The number of allowed spin-2 states is therefore very large, and one cannot address all possibilities in a single study with current statistics. The highest priority is to exclude first the minimal spin-2 model, corresponding to the lowest dimension operators.

The coupling parameters used in the analysis are shown for each spin hypothesis in Table 7.1.1. For the spin-2 state, the minimal choice follows that discussed in Refs. [34, 18].

Table 7.1. Choice of coupling parameters for the spin-0 and spin-2 models considered in the current analysis [18].

J^P	Production configuration	Decay configuration	Comments
0^+	$gg \to X$:	$g_1 = 1$ $g_2 = g_3 = g_4 = 0$	SM Higgs-like scalar
0_h^+	$gg \to X$:	$g_1 = 0$ $g_2 = 1$ $g_3 = g_4 = 0$	scalar with higher-dimension operators
0^-	$gg \to X$:	$g_4 = 1$ $g_1 = g_2 = g_3 = 0$	pseudo-scalar
2_m^+	$gg/qq \to X$:	$g_1 = g_5 = 1$	Graviton-like tensor with minimal couplings

7.2. Matrix element

Following the notation in Refs. [18, 35], the generic scattering amplitude of a spin-0 Higgs boson H decaying to vector bosons is given by:

$$A(H \to V_1V_2) = \upsilon^{-1}\left(g_1 m_V^2 \epsilon_1^* \epsilon_2^* + g_2 f_{\mu\nu}^{*(1)} f^{*(2),\mu\nu} + g_3 f^{*(1),\mu\nu} f_{\mu\alpha}^{*(2)} \frac{q_\nu q^\alpha}{\Lambda^2} + g_4 f_{\mu\nu}^{*(1)} \tilde{f}^{*(2),\mu\nu}\right) \tag{7.4}$$

where υ is the vacuum expectation value of the Higgs field, and $f^{(i),\mu\nu}$ ($\tilde{f}^{(i)}_{\mu\nu}$) denotes the (conjugate) field strength tensor for boson V_i with polarization vector ϵ_i, four-momentum q_i, and mass m_V. The form factors g_i are generically complex, and vary depending on the CP properties of H. The invariant amplitude of the Standard Model (SM) Higgs is described by Eq. 7.4 when $g_1 = 1$ and $g_i \approx 0$ for $i \neq 1$. A CP-odd component corresponds to a non-zero value of g_4. Measuring all form factors would fully specify the CP structure of the particle.

It is convenient to use the following parameterization[35] (the details will be discussed below),

$$\begin{aligned} f_{g4} &= \frac{\sigma_4|g_4|^2}{\sigma_1|g_1|^2+\sigma_2|g_2|^2+\sigma_4|g_4|^2}, \qquad \phi_{g4} = \arg\left(\frac{g_4}{g_1}\right) \\ f_{g2} &= \frac{\sigma_2|g_2|^2}{\sigma_1|g_1|^2+\sigma_2|g_2|^2+\sigma_4|g_4|^2}, \qquad \phi_{g2} = \arg\left(\frac{g_2}{g_1}\right) \end{aligned} \tag{7.5}$$

where σ_i is the predicted $H \to ZZ^*$ cross-section with $g_i = 1$, and $g_j = 0$ for $j \neq i$. The contribution from g_3 to the scattering amplitude is expected to be negligibly small for a SM Higgs boson (0^+), and well as for other hypotheses such as 0^- and 0^+_h. It is therefore assumed to be zero in the above parameterization. The parameter f_{g4} roughly corresponds to the fraction of the observed CP-odd component. It is equivalent to the parameter f_{a3}, studied in Ref. [35], under the assumption that $g_2 = g_3 = 0$.

The couplings g_1, g_2 and g_3 correspond to the interaction with the CP-even and g_4 to the interaction with the CP-odd boson respectively. The term corresponding to g_3 is expected to be small [16] and thus set to zero in this study and excluded from the following discussion. The coupling notation g_1, g_2 and g_4 is used throughout the rest of this note.

Similarly to the (f_{a_i}, ϕ_{a_i}) parametrisation proposed in the Ref. [35], the (f_{g_i}, ϕ_{g_i}) parametrisation introduced in the Ref. [35] is used:

$$f_{g_i} = \frac{|g_i|^2 \sigma_i}{|g_1|^2\sigma_1 + |g_2|^2\sigma_2 + |g_4|^2\sigma_4}; \quad \phi_{g_i} = \arg\left(\frac{g_i}{g_1}\right). \tag{7.6}$$

In the current analysis g_2 and g_4 are measured separately, assuming the simultaneous presence of only g_1 and of the coupling under study, this corresponds to set $g_2 = 0$ ($g_4 = 0$) in the expression of f_{g_4} (f_{g_2}) in (Eq. 7.6).

It should be noted that with these assumptions the f_{g_4} is equivalent to the f_{a_3} and thus the direct comparison of respective experimental limits is possible.

7.3. Monte Carlo simulations

The JHU[1] v4.2.1 generator has been used to simulate the decay of a SM Higgs boson with a mass of 125.5 GeV for the spin and parity states considered in this analysis at $\sqrt{s} = 7$ TeV and $\sqrt{s} = 8$ TeV. The Pythia8 MC generator is employed for the inital-state and final-state radiation, as well as the parton showers. Validation studies of the JHU Monte Carlo samples have been performed[35].

The POWHEG next-to-leading-order (NLO) generator is chosen as reference here, since it provides to date the best prediction for a Standard Model Higgs p_T spectrum, being in very good agreement with the next-to-next-to-leading logarithmic (NNLL)+NLO prediction by H_QT [19, 30]. In Appendix A.3 the results of a comparison of the JHU and POWHEG relevant kinematic distributions for a Higgs of spin parity 0^+ are provided.

This comparison is performed at the generator level after the Pythia8 parton showering is applied, using a JHU $gg \to Z^{(*)}Z^{(*)} \to 4l$ sample. Good agreement between the distributions in two generators is found except for the transverse momentum of

[1]JHU generator is a MC generator based on the Ref. [35]

the Higgs, where a discrepancy is observed, as expected since JHU only simulates the leading-order terms in the process.

While the mismodeling of the transverse momenta by the JHU generator does not directly affect the parity-dependent observables, it may have an impact on the event selection. In order to correct for this effect, the hard process parton interaction generating the resonance boson is obtained with the POWHEG generator, using the AU2_CTEQ6L1 parton density functions and later decayed with JHU.

A generator-level cut of 100 GeV $< m_{4\ell} <$ 150 GeV is applied to the simulation output. The ATLAS detector effects of energy and momentum scale and resolution, and efficiencies for lepton trigger, reconstruction, and identification, are modeled using full simulation. Tables in Appendix A.2 show the list of MC samples for different signal hypotheses and models of final state interference, respectively, used in this analysis.

A common set of Monte Carlo samples is used for both analyses, with a fixed $m_H = 125.5$ GeV while scanning anomalous higgs couplings, as presented this note. The production is only performed for one set of tensor couplings: $g_1 = 1$, $g_2 = 1 + i$, $g_4 = 1 + i$. All other configurations of couplings are obtained by reweighting the base sample at generator level using ratios of the corresponding matrix elements (ME) calculated at LO. For this calculation, the JHUGen.v4.2.1 ME [34] is used. The reweighting procedure is validated against independently produced samples to ensure that the distributions of the CP-sensitive final state observables and of their correlations are reproduced correctly. The corresponding configurations of tensor couplings are reported in Table 7.2.

Standard Model Higgs boson		
$g_1 = 1$	$g_2 = 0$	$g_4 = 0$
Anomalous coupling samples		
$g_1 = 1$	$g_2 = 1$	$g_4 = 1$
$g_1 = 1$	$g_2 = 1 + i$	$g_4 = 0$
$g_1 = 1$	$g_2 = 0$	$g_4 = 2 + 2i$

Table 7.2. Choice of tensor couplings configurations used for reweighting tests.

7.4. Re-weighting validation

The weights used to reweight the base sample to the target one are obtained using JHU.v4.2.1, where final state interference is included. The MEs of both the base and target configurations are calculated by providing as input to JHU the four-vectors of the final-state leptons, and their ratio, $ME_{target}/ME_{\text{base}}$, is used to weight each event of the base sample. To make sure that the method produces reliable distributions, the reweighted distribution of final state observables were compared to those from MC samples generated at the reweighted target value. Examples of such tests can be found in Figs. 7.2, 7.3, 7.4 and 7.5, which show tests for the Standard Model and coupling sets ($g_1 = 1$, $g_2 = 1$, $g_4 = 1$), ($g_1 = 1$, $g_2 = 1 + i$, $g_4 = 0$) and ($g_1 = 1$, $g_2 =$, $g_4 = 2 + 2i$) respectively. The distributions show the four final states merged, after detector simulation and analysis cuts. It is seen that, within statistical uncertanties, there is good agreement.

7.5. Measured observables and parameters

The observables sensitive to the underlying spin and parity are the masses of the two Z bosons, along with two production angles (θ^*, ϕ_1), and three decay angles (ϕ, θ_1, θ_2) [18]. Through the rest of this section, the intermediate Z bosons will be labeled Z_1 and Z_2, where the index 1 is assigned to the Z whose observed mass is the closest to the nominal PDG value. Their respective masses will be denoted m_{12} and m_{34} and the corresponding final state lepton pairs labeled the "first" and the "second" respectively. In the low-mass region ($m_H < 180$ GeV), the shapes of m_{12} and m_{34} become sensitive to spin and parity.

In the case of a spin-zero boson, the production cross section does not depend on the production angles θ^* and ϕ_1. Here different parities can be distinguished by studying the decay angles ϕ, θ_1, and θ_2 and Z boson masses m_{12} and m_{34}. The

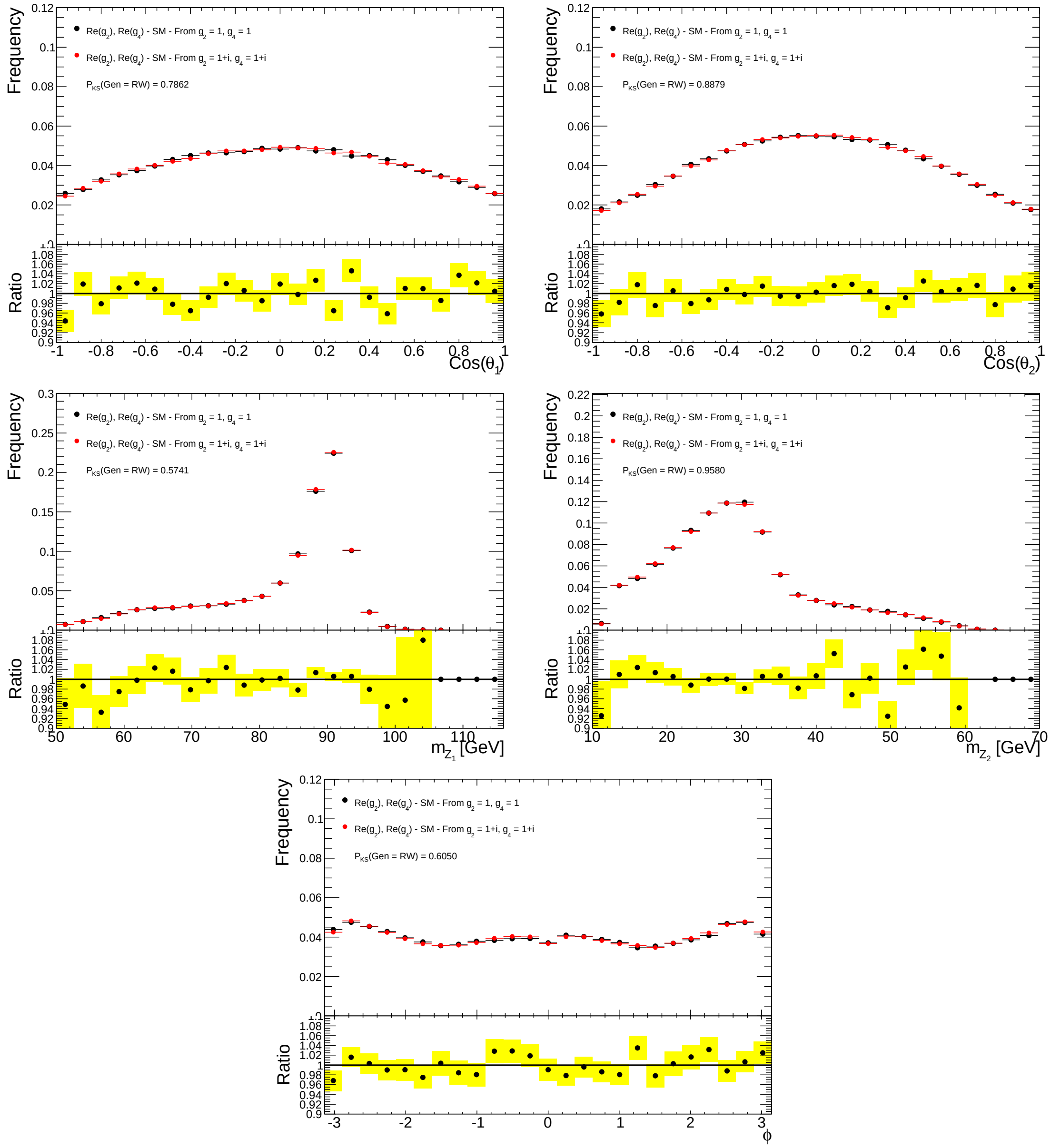

Figure 7.2. Standard Model final state observables. The figures contain in order: $\cos(\theta_1)$, $\cos(\theta_2)$, m_{Z1}, m_{Z2}, Φ, and are evaluated after full detector simulation and selection. The red distributions are reweighted from the sample with couplings $g_1 = 1$, $g_2 = 1+i$, $g_4 = 1+i$ while the black distributions are reweighted from $g_1 = 1$, $g_2 = 1$, $g_4 = 1$.

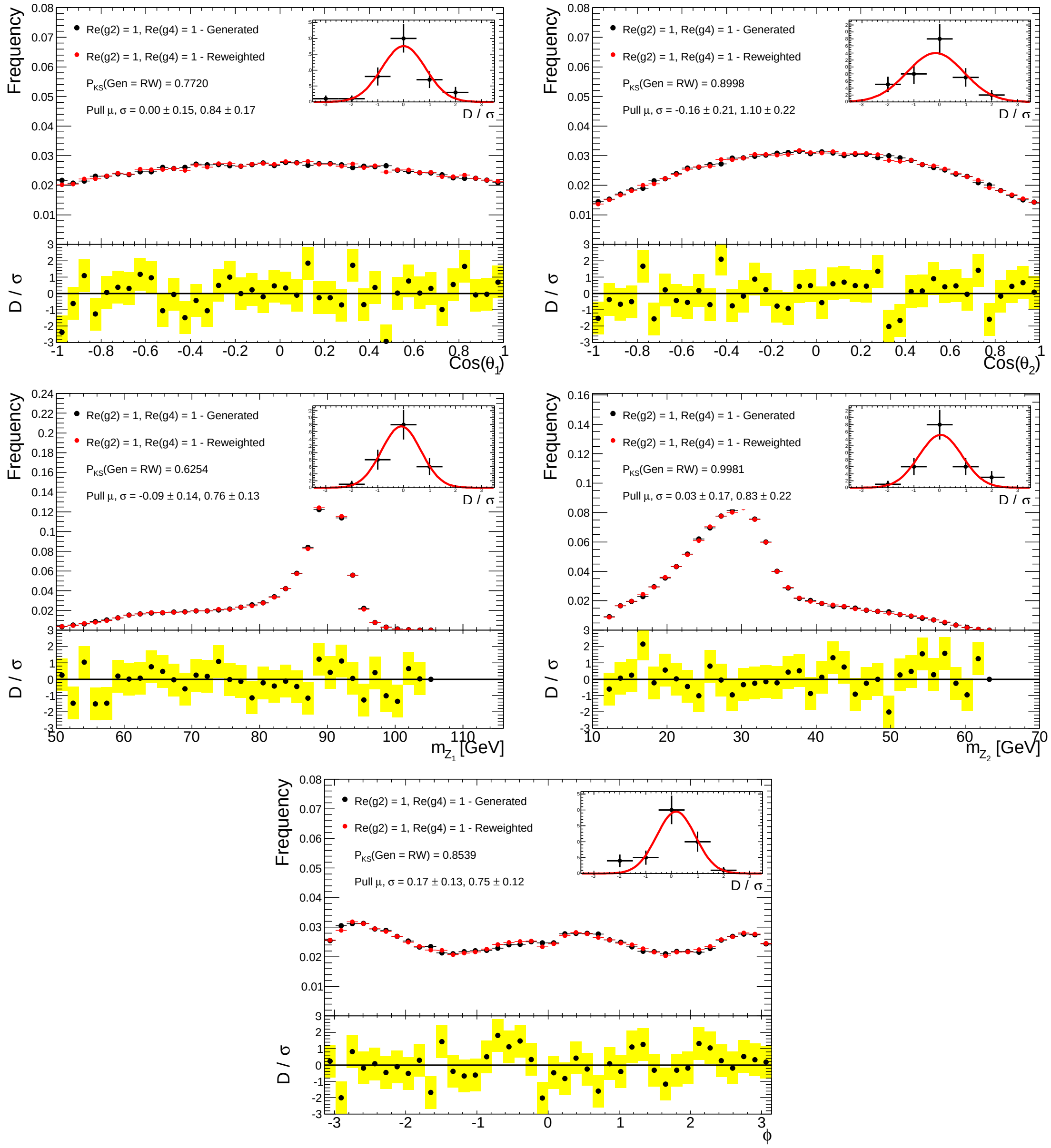

Figure 7.3. Reweighted (red) and directly-generated (black) final state observables. The figures show in order: $\cos(\theta_1)$, $\cos(\theta_2)$, m_{Z1}, m_{Z2}, Φ. The distributions shown correspond to the set of couplings: $g_1 = 1$, $g_2 = 1$, $g_4 = 1$ and are evaluated after full detector simulation and selection; the inset plots show the corresponding distributions for the frequency.

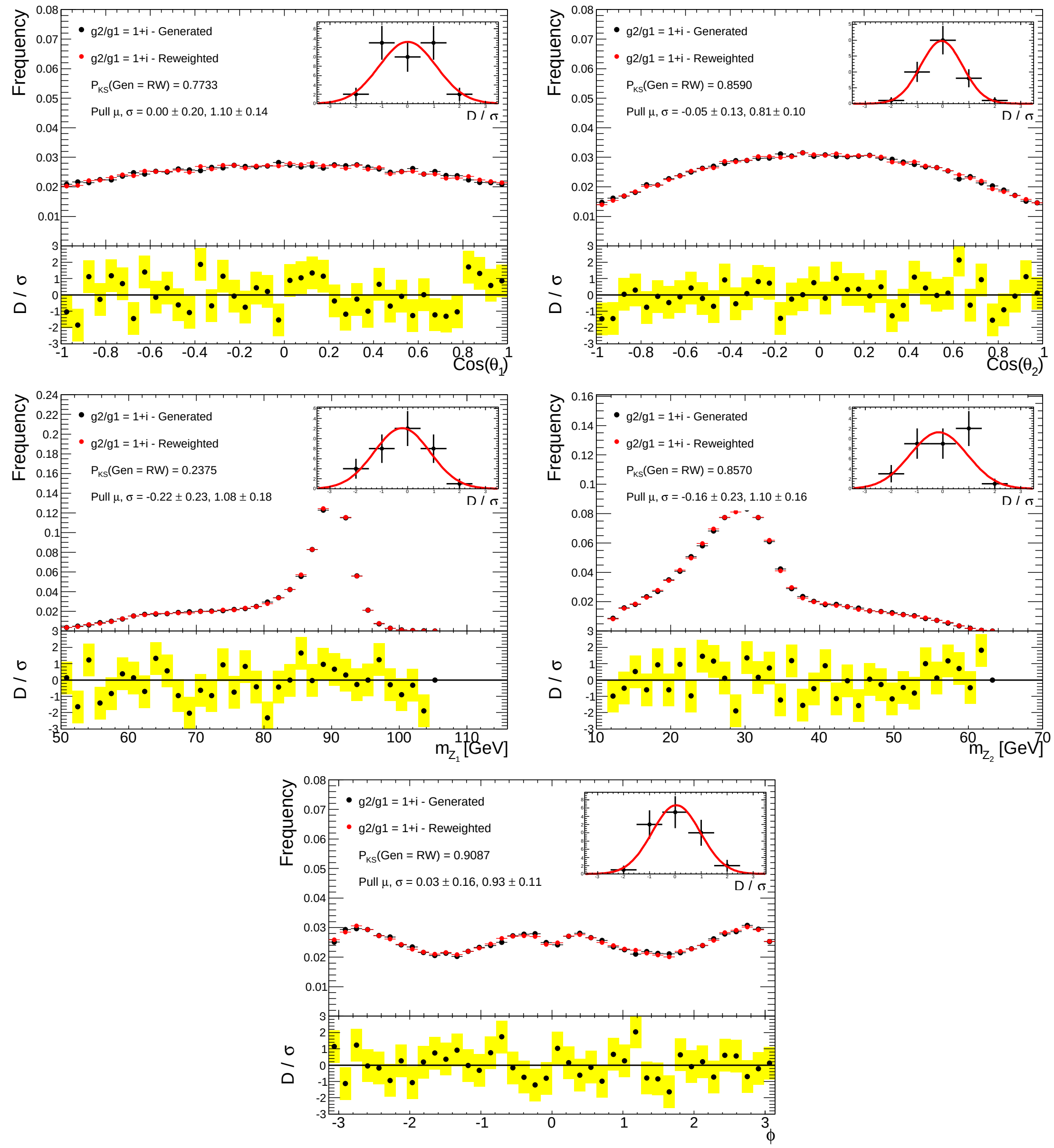

Figure 7.4. Reweighted (red) and directly-generated (black) final state observables. The figures show in order: $\cos(\theta_1)$, $\cos(\theta_2)$, m_{Z1}, m_{Z2}, Φ. The distributions shown correspond to the set of couplings: $g_1 = 1$, $g_2 = 1+i$, $g_4 = 0$ and are evaluated after full detector simulation and selection; the inset plots show the corresponding distributions for the frequency.

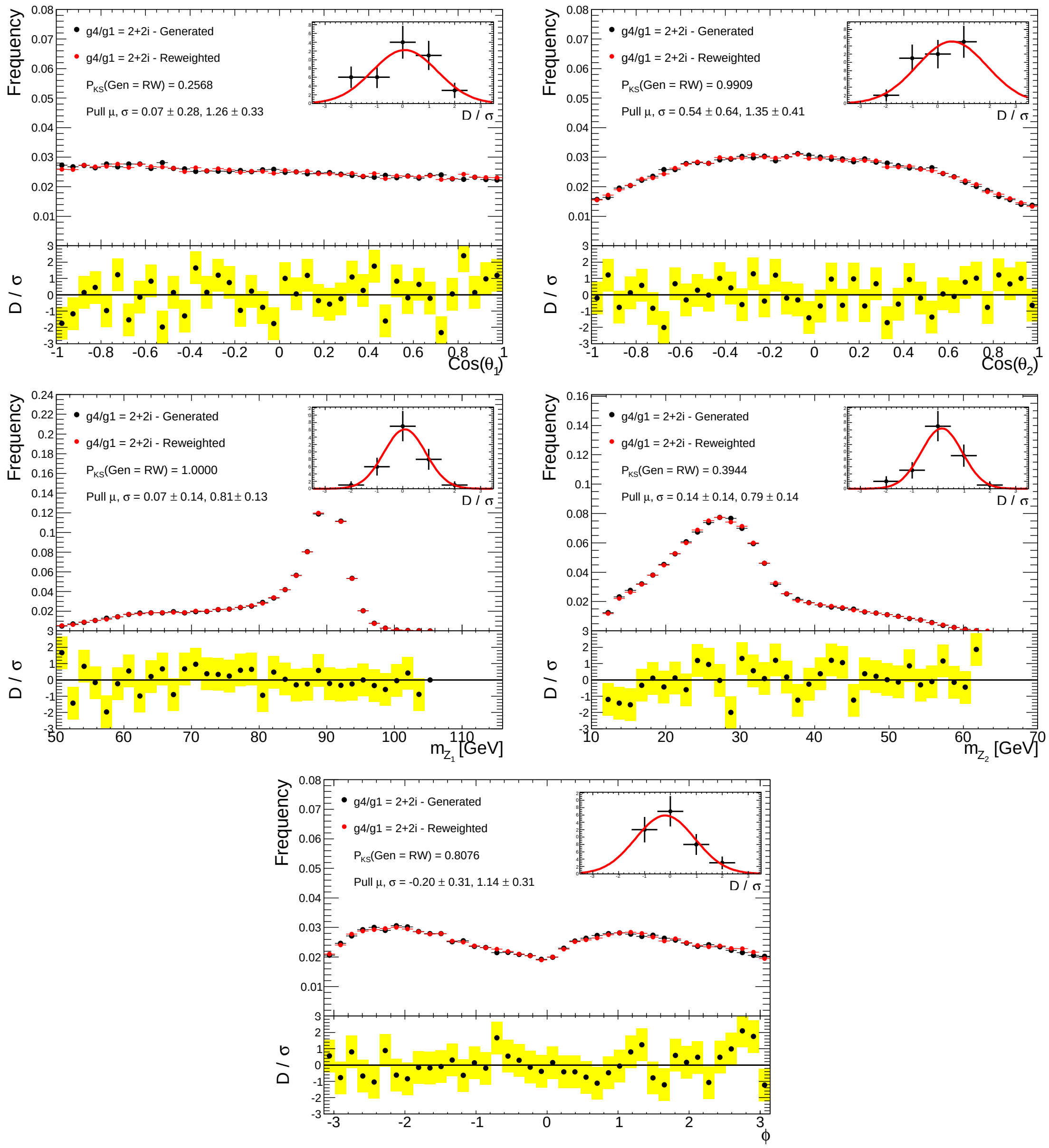

Figure 7.5. Reweighted (red) and directly-generated (black) final state observables. The figures show in order: $\cos(\theta_1)$, $\cos(\theta_2)$, m_{Z1}, m_{Z2}, Φ. The distributions shown correspond to the set of couplings: $g_1 = 1$, $g_2 = 0$, $g_4 = 2 + 2i$ and are evaluated after full detector simulation and selection; the inset plots show the corresponding distributions for the frequency.

production angles are important when discriminating between particles of different spin.

As outlined above, the production angles are defined in the four-lepton rest frame. It can be seen that the transverse momentum of the four-lepton system may introduce uncertainties in their determination. For a system with significant transverse momentum, the axes of colliding partons in the four-lepton rest frame will not be collinear. To compensate for this effect, it is common to express production angles in the Collins-Soper frame [28], placing the z-axis half way between the axes of two Z bosons. The benefit from introducing the Collins-Soper frame was studied and found to be negligible within the signal region considered and our pressent statistics.

The invariant amplitude describing the interaction of a spin-0 particle and two spin-one gauge bosons can be presented through the polarization vectors of the gauge bosons ϵ_1 and ϵ_2:

$$A(H \to VV) \sim (a_1 M_H^2 g_{\mu\nu} + a_2 (q_1 + q_2)_\mu (q_1 + q_2)_\nu + a_3 \epsilon_{\mu\nu\alpha\beta} q_1^\alpha q_2^\beta) \epsilon_1^{*\mu} \epsilon_2^{*\nu}. \qquad (7.7)$$

Here q_1 and q_2 are the four-momenta of the gauge bosons. Two out of the three couplings (a_1, a_2 and a_3) can in general be complex numbers. The couplings a_1 and a_2 describe the tree-level and loop-induced interaction of a CP-even particle with two gauge bosons. The a_3 coupling is responsible for the interaction of a CP-odd particle. The CP-conserving tree-level Standard Model is given by $a_1 = 1$ and $a_{2,3} = 0$. CP violation in the Higgs sector can be generated requiring the simultaneous presence of a_3 and either a_1 or a_2. The observation of a statistically significant non-zero a_2 in HZZ decay would demonstrate the presence of higher-order loop processes beyond those predicted by the Standard Model.

The first experimental constraint on the contribution of the a_3 coupling was published in the Ref. [43]. In this analysis a parametrization where three independent tensor couplings are represented by two cross section fractions f_{a_3} and f_{a_2} and two phases ϕ_{a_3} and ϕ_{a_2} was used. The corresponding definitions were:

$$f_{a_i} = \frac{|a_i|^2\sigma_i}{|a_1|^2\sigma_1 + |a_i|^2\sigma_i}; \quad \phi_{a_i} = \arg\left(\frac{a_i}{a_1}\right), \tag{7.8}$$

where σ_i are the effective cross sections of the process corresponding to $a_i = 1$ and $a_{j\neq i} = 0$. The experimental limit on the CP-odd cross section fraction f_{a_3} was set.

Because they involve the ratio of cross sections, the quantities f_{a_i} are not sensitive to possible interference between various parts of the decay amplitude (see Eq. 7.7). Measurements of ϕ_{a_i} would provide information about the complex structure of couplings.

An alternative approach to study the tensor structure of the amplitude (7.7) is to measure the couplings a_1, a_2 and a_3, or their ratios. This approach is free of the assumptions on the size of the interference effects and its results can be expressed in (f_{a_i}, ϕ_{a_i}) parametrization at any moment.

Another form of the amplitude (see Eq. 7.7) can be found in Refs. [34, 18]. Here four couplings $g_{1..4}$ are introduced with the following momentum-dependent relation to $a_{1..3}$:

$$a_1 = g_1\frac{m_V^2}{m_H^2} + \frac{s}{m_H^2}\left(2g_2 + g_3\frac{s}{\Lambda^2}\right) \quad a_2 = -\left(2g_2 + g_3\frac{s}{\Lambda^2}\right) \quad a_3 = -2g_4, \tag{7.9}$$

where m_V is the mass of the gauge boson, $s = q_1 q_2$ and Λ is the new physics scale. The couplings g_1, g_2 and g_3 correspond to the interaction with the CP-even and g_4 to the interaction with the CP-odd boson respectively. The coupling notation g_1, g_2 and g_4 is used throughout the rest of this note.

The $(f_{a_2}, f_{a_3}, \phi a_2, \phi a_3)$ parametrization is equivalent to $(f_{g_2}, f_{g_4}, \arg(g_2/g_1), \arg(g_4/g_2))$ proposed in Ref. [35], assuming $g_3 = 0$, $g_2 = 0$ for the measurement of g_4 and $g_4 = 0$ for the measurement of the g_2. The $(f_{a_2}, f_{a_3}, \phi_{a_2}, \phi_{a_3})$ parameter space is adopted in the current study for consistency with previously published results.

7.6. Final state interference

The interference in final states with same-flavor leptons is modeled in the JHU generator and checked with the MadGraph generator. The Prophecy4f generator[2] is also used as a systematic check, with the difference with respect to JHU being assigned as a systematic uncertainty.

[2]Prophecy4f is a Monte Carlo event generator for precise simulations of the Higgs-boson decay $H \to WW/ZZ \to 4f$, supporting leptonic, semileptonic, and four-quark final states. Both electroweak and QCD corrections are included.

Chapter 8

Hypothesis Testing

In this chapter, a description is given of the two approaches adopted to discriminant between pairs of different spin-parity states. First the characteristics are described that are common to the two analyses, beyond the material discussed in Chapter 5. First, I discuss the spin and parity discriminating variables, and then the statistical treatment used for hypotheses testing. Then the BDT and $\mathrm{J^p} - \mathrm{MELA}$ discriminants will be described. Finally, I will describe the evaluation of the systematic uncertainties and the expected hypothesis separation as estimated from MC simulation.

8.1. Spin-parity discriminating variables

Presented in the Figs. 8.1, 8.2 and 8.3 are the distributions of spin and parity sensitive observables (see Sec. 7.5) in the signal mass range selected by the main analysis (115 GeV $\leq m_{4\ell} \leq$ 130 GeV) for 8 TeV dataset. The signal contribution is shown for both 0^+, 0^-, 0_h^+ and 2_m^+ hypotheses.

8.2. Statistical treatment

In the hypothesis testing analysis, pairs of different spin and parity models are assessed against each other. A maximal likelihood fit is performed on the events falling in the signal mass region. The likelihood model for any given J^p hypothesis is of the form:

$$\mathcal{L}(J^p, \mu, \theta) = \prod_{j}^{\mathrm{N_{chan}}} \prod_{i}^{\mathrm{N_{bin}}} P(N_{i,j} | \mu_j \cdot S_{i,j}^{(j^p)}(\theta) + B_{i,j}(\theta)) \ , \tag{8.1}$$

where P denotes a Poissonian distribution evaluated at the observed $N_{i,j}$ events in observable bin i, final state j (depending on flavor of four leptons), with corresponding expectation value. The $S_{i,j}$ ($B_{i,j}$) value describes the signal (background) probability density function evaluated in observable bin i, final state j, scaled by the integral number of signal (background) events. The background is a sum of the ZZ^* continuum and reducible backgrounds. The nuisance parameter μ, the signal strength, has been emphasized out of the remaining set, θ. In the maximal likelihood fit the signal strength is allowed to float, modifying the signal normalisation. Note that the background normalisations, contained in the nuisance parameter set θ, are considered as free parameters of the fit.

The remaining systematic uncertainties, symbolised by θ, are described below. Complimentary approaches have been used in the construction of signal and background observables that effectively discriminants different spin and parity hypotheses.

The log-ratio of profiled likelihoods is used as the test statistic. It is defined as follows, using as an example the hypothesis test of $J^p = 0^+$ and $J^p = 0^-$:

$$q = \ln \frac{\mathcal{L}(J^p = 0^+, \hat{\hat{\mu}}_{0^+}, \hat{\hat{\theta}}_{0^+})}{\mathcal{L}(J^p = 0^-, \hat{\hat{\mu}}_{0^-}, \hat{\hat{\theta}}_{0^-})} \tag{8.2}$$

where all nuisance parameters have been fitted to maximize the likelihoods, which means that the -2ln$\,\Lambda(\mu)$ is at the maximum value. The test statistic for all other hypotheses have been constructed in a similar manner.

The systematic uncertainties are allowed to modify signal and background expectations under the hypothesis that they can be modeled as Gaussian convoluted with the nominal likelihood function. A large ensemble of Monte Carlo pseudo experiments (at least 5 million) is used to estimate the expected test statistic distribution under the different hypothesis tested. The p_0 value for any hypothesis follows directly as the tail integral of the distribution starting at the (pseudo)data test statistic value.

Expectations for different signal models are calculated by using the median value of test statistic distributions.

8.3. Boosted Decision Tree (BDT)

8.3.1. BDT Training

For each hypothesis test, two BDTs were used. One was optimised to separate the two J^p hypotheses under study and one served as a background discriminant optimised to separate a Standard Model Higgs Boson ($J^p = 0^+$) from the ZZ continuum background. A single background discriminant was used for all hypothesis tests. It was found that the two discriminants are weakly correlated in all cases. Taking this into consideration, it was determined that using more complex approaches for non-SM hypotheses would not change the result in any noticeable way. The final state observables used for the angular and kinematic BDT discriminants are as follows:

- 0^+ vs. 0^- and 0^+ vs. 0^+_h separation: m_{12}, m_{34}, $\cos(\theta_1)$, $\cos(\theta_2)$, ϕ;
- 0^+ vs. 2^+_m separation: m_{12}, m_{34}, $\cos(\theta_1)$, $\cos(\theta_2)$, ϕ, $\cos(\theta^*)$, ϕ_1;
- 0^+ vs. ZZ^* separation: m_{4l}, p_{T-4l}, η_{4l}, Kinematic Discriminant (KD)

where m_{4l}, p_{T-4l}, and η_{4l} are the mass, transverse momentum, and pseudorapidity respectively of the four-lepton system.

The final-state observables that the BDTs are trained on are summarised in Table 8.2. The distributions used in the different trainings are seen in Figs. 8.1, 8.2 and 8.3. The separation between states arises mainly due to correlations between parameters that cannot be effectively utilized by simple cuts. Only events falling in the signal mass region 115–130 GeV were used.

The training was performed using the TMVA toolkit for multivariate analysis [39]. Other types of multivariate approaches have been tested, like the Neural Network

[38] and Fisher Linear Discriminant [55]. The BDT approach was found to give the optimal result as it is able to describe the non-linear correlations between the final state observables without introducing significant overtraining[1].

The J^p discriminating BDTs are constructed from between 200 and 800 trees, each having a maximal depth of 3. The background discriminant was trained with between 300 and 900 trees with a maximal depth of 3 to 5. In all cases the BDTs where optimised using gradient boosting and bagging resampling as described in [39]. A detailed description of the setup can be found in Tab. 8.1. All configurations are chosen to give the maximal separation without being overtrained.

Table 8.1. Table of parameters used for the BDT training. The definitions of the options can be found in Table 22, 23 and 24 of [39]. The names are translated as follows: $\mathrm{N_{Trees}}$: NTrees, Shrink.: Shrinkage, MNP: NodePurityLimit, S/B: SigToBkgFraction, BSF: BaggedSampleFraction, $\mathrm{N_{Cuts}}$: nCuts, Max depth: MaxDepth. All the forest of trees are moreover boosted using bagging resampling.

Separated Hypotheses	$\mathrm{N_{Trees}}$	Shrink.	MNP	S/B	BSF	$\mathrm{N_{Cuts}}$	Max depth
$J^p = 0^+,\ 0^-$	200	0.10	0.5	1	0.6	20	3
$J^p = 0^+,\ 0^+_h$	800	0.03	0.6	1	0.8	20	3
$J^p = 0^+,\ 2^+_m$	200	0.10	0.5	1	0.6	20	3
$J^p = 0^+$, ZZ-continuum							
4e	300	0.03	0.6	1.5	0.6	20	3
4μ	900	0.05	0.6	1.5	0.6	20	5
$2e2\mu$	300	0.03	0.6	1.5	0.6	20	3
$2\mu 2e$	300	0.02	0.6	1.5	0.6	20	3

For each separation the MC samples of the two hypothesis were divided into two of equal size whose entries were chosen at random. The BDT training was performed on one of the partitions, called the "training sample." To ensure that the

[1]Overtraining occurs when a classifier models signal/background differences that are specific to the particular training sample used statistical fluctuations

discriminant training did not optimise differences caused by statistical fluctuations, the resulting shape was compared to the second half of the data sample. To evaluate the effect of overtraining the resulting ROC[2] integral was computed for both test and training sample. For each separation it was found that the difference was 1% or below, Tab. 8.2. Examples of test and training sample distributions are shown in Fig. 8.4 and 8.5.

Table 8.2. BDT summary table. The columns show in consecutive order: the two models for any training, the final state observables used as training parameters and the resulting ROC integral for the sample the training has been performed on and a statistical independent sample of equal size and the difference between the two. The ROC has been defined in such a way that a integral of 0.5 indicates no separation, and 1.0 indicates perfect separation. The differences indicate the size magnitude of overtraining and is seen to be at most at the percent level.

Separated Hypotheses	Training parameter	$\int$ ROC$_{\text{Train}}$	$\int$ ROC$_{\text{Test}}$	Difference
	$\sqrt{s} = 8$ TeV			
$J^p = 0^+,\ 0^-$	$\cos(\theta_1)$, $\cos(\theta_2)$, m_1, m_2, Φ	0.681	0.677	0.6 %
$J^p = 0^+,\ 0^+_h$	$\cos(\theta_1)$, $\cos(\theta_2)$, m_1, m_2, Φ	0.630	0.624	1.0 %
$J^p = 0^+,\ 2^+_m$	$\cos(\theta_1)$, $\cos(\theta_2)$, m_1, m_2, Φ, $\cos(\theta^*)$, Φ_1	0.629	0.622	1.1 %
$J^p = 0^+$, ZZ-continuum	m_{4l}, p_{T-4l}, η_{4l}, KD	-	-	-
4e		0.887	0.884	0.3 %
4μ		0.891	0.886	0.6 %
$2e2\mu$		0.887	0.884	0.3 %
$2\mu2e$		0.885	0.882	0.3 %
	$\sqrt{s} = 7$ TeV			
$J^p = 0^+,\ 0^-$	$\cos(\theta_1)$, $\cos(\theta_2)$, m_1, m_2, Φ	0.683	0.680	0.4%
$J^p = 0^+,\ 0^+_h$	$\cos(\theta_1)$, $\cos(\theta_2)$, m_1, m_2, Φ	0.629	0.628	0.2%
$J^p = 0^+,\ 2^+_m$	$\cos(\theta_1)$, $\cos(\theta_2)$, m_1, m_2, Φ, $\cos(\theta^*)$, Φ_1	0.627	0.625	0.3%
$J^p = 0^+$, ZZ-continuum	m_{4l}, p_{T-4l}, η_{4l}, KD	-	-	-
4e		0.878	0.875	0.3%
4μ		0.890	0.881	0.1%
$2e2\mu$		0.876	0.878	0.2%
$2\mu2e$		0.873	0.876	0.3%

[2]ROC stands for "receiver operating characteristic", which shows the signal efficiency versus background.

The various discriminant distributions separating the different hypotheses, $J^p = 0^+$ vs. $J^p = 0^-$, $J^p = 0^+$ vs. $J^p = 0^+_h$, and $J^p = 0^+$ vs. ZZ^*-continuum, are shown in Figure. 8.4 and 8.5.

8.3.2. PDF construction

For any given signal model and background, the discriminant separating the two spin-parity states and the background discriminant is correlated to some degree. It is therefore necessary to construct two-dimensional pdfs that are able to describe any non-trivial correlation to its full degree.

For each hypothesis test, the discriminant distributions of the hypotheses and background separating BDT from simulated data were described with a two-dimensional histogram of suitable binning (40×40 bins). By construction, the BDT values are confined to the range [-1, 1]. Populating a histogram of 1600 bins with simulated data would require an unreasonably large amount of statistics.

To counter the effects of statistical fluctuations, smoothed pdfs are derived from the histograms with a Gaussian Multivariate Kernel Density Estimation (KDE) using the RooNDKeysPDFs package[3]. The multivariate KDE is done with a adaptive bandwidth. It was found that a bandwith scale (ρ) of 0.35 gave the optimal description. The same procedure is done for signal, ZZ*-continuum and reducible background processes.

All data are divided into the four final states $4e$, 4μ, $2e2\mu$, and $2\mu 2e$ prior to having corresponding parent's distribution estimated with the KDE method. The KDE is afterwards projected into the final histogram. As an example, the hypothesis test

[3]RooNDKeysPDFs is function method of RooFit[53]

separating the positive and negative spin-0 parity states will thus be based on four pdfs for each of the $J^p = 0^+$, $J^p = 0^-$, ZZ* background, and reducible background process types each of which has been created twice to describe both the 7 TeV and 8 TeV distributions. These all exist in versions reflecting systematic changes, described below.

An example of the KDE approach is presented in Fig. 8.6. Here the $J^p = 0^+ \rightarrow 2e2\mu$, $J^p = 2^+_m \rightarrow 2e2\mu$, and $ZZ^* \rightarrow 2e2\mu$ are filled in to a histogram that are subsequently smoothed. To validate this approach the pull distribution from comparing the original histogram to the resulting KDE-pdf using the histogram statistical errors have been produced. It is seen that there is good agreement between the distributions.

8.3.3. Backgrounds

As with the signal processes, the background distributions are estimated in the signal mass region 115-130 GeV. The backgrounds are divided into two categories:

- The irreducible ZZ^* background continuum. The shape and normalisation is taken from Monte Carlo created with the PowHeg generator.
- The sum of reducible backgrounds, based on data-driven estimates from control regions.

Being data-driven, the size of the reducible background sample is problematic. Like the signal and ZZ* samples, 2D distributions are estimated with the KDE approach described above.

8.3.4. Systematic uncertainties

The majority of the systematic uncertainties in the BDT spin and parity analysis are equivalent to those in the main analysis. Uncertainties related to theoretical predictions, background normalisations, and integrated luminosity are believed to be the same as in the main analysis since the two analyses share common selection and, to some degree, Monte Carlo. A detailed description of systematic uncertanties can be found in [9].

In addition to this systematic effects will affect the BDT discriminant shape. The systematic effects are described by either generating a dedicated Monte Carlo sample or assigning a set of event weights to the nominal sample, both corresponding to a single systematic change. The procedure of filling two dimensional histograms and performing a KDE estimation, described above, is repeated for each systematic change separately. The shapes corresponding to systematic changes are finally added to the likelihood model before each fit. The model is allowed to vary, under a Gaussian constraint by interpolating between the different systematic changes.

The systematic changes related to the BDT discriminant that are not shared with the common analysis is described below:

BDT over-training Finite statistics in the BDT training may potentially have an impact on the MVA output. In fact the MVA can learn statistical fluctuations from the training sample that can be absent or different in the testing sample.

In order to assess the magnitude of this effect, the expected separations between spin and parity hypotheses were compared for the case when the shapes of the BDT response for the combined training and test sample were used (as in the analysis) and for when these samples were used seperately. No difference was observed.

This is also confirmed by the insignificant difference in ROC integrals presented in Table 8.2.

Mass resolution and mis-modelling (alpha_ATLAS_Higgs_mass) Mass resolution and mis-modelling of the reconstructed Higgs boson mass has been taken as an additional source of systematic uncertainty. It is worth noting that the four lepton mass is the strongest separating parameter used in the background discriminant. The mass and the background discriminant are therefore strongly correlated. A shift of 500 MeV in the signal four lepton mass is applied to take this uncertainty into account. The change in observable distributions were found to influence the results while potential changes in the signal yield was found to have insignificant impact. Only distribution changes were considered for the final estimates.

Smoothing procedure (alpha_ATLAS_rho_signal, alpha_ATLAS_rho_Redbkg, alpha_ATLAS_rho_ZZ) It is likely that different choices of bandwith used in the kernel density estimation would have resulted in equally valid descriptions while at the same time showing slight shape differences. To estimate the uncertainty introduced by the kernel density estimation smoothing the bandwith was changed from the nominal 0.35 to 0.30 and 0.40. The same procedure was applied to signal, ZZ*-continuum and reducible background shapes, using a rho value of 0.35 for each. A seperate nuisance parameter was used for each case.

The effect of each nuisance parameter was subsequently estimated. This was done by calculating the log profiled likelihood ratio between the $J^p = 0^+$, $J^p = 0^-$ when all nuisance parameters where included and when a single one was shifted 1 standard deviation in either side. Assuming asymptotic behavior the log ratio value can be converted into a significance. The difference in signifance when including all nuisance parameters and when shifting was used as a measure of relevance of each systematic uncertainty.

It is of great interest to rank these systematic uncertainties, both because it is important to demonstrate that the impact follows expectations, but also any irrelevant parameters can be discarded. It should be noted that the computing time for the final significance is strongly dependent on the number of nuisance parameters.

A threshold of 0.45% was chosen as to where a parameter was relevant for the analysis.

8.3.5. Summary of BDT strategy

- At the first stage of the analysis, the full event selection is applied on all the Monte Carlo samples for different spin and parities and to the ZZ background samples simulated in the region 100 GeV $< m_{4\ell} <$ 150 GeV. The observables sensitive to the spin and parity of the underlying resonance which were discussed in the beginning of this note are reconstructed for all the samples in the signal region: 115 GeV $< m_{4\ell} <$ 130 GeV. The obtained set of observables is used to train a set of the BDT discriminants. A single background discriminant, used for all hypothesis tests, is constructed to discriminate the ZZ* background continuum. An J^p discriminant is trained to distinguish between one pair of spin and parity states. Discriminants to distinguish $J^p = 0^+$ from $J^p = 0^-, 0_h^+$ and 2_m^+ where constructed. The distributions of values of J^p discriminants applied to the signal and background samples are later used to compare to the observed data as described below.

- At the second stage, the simulated signal and background distributions for the angular and kinematic discriminants are described using a two-dimensional histogram. This way all non-trivial correlations can be taken into account. The histograms are subsequently described using a Gaussian KDE to reduce the influence of statistical fluctuations. The procedure is done separately for all 4 final states considered in the present analysis: $4e$, 4μ, $2e2\mu$ and $2\mu2e$. A separate histogram was created for each systematic uncertainty.

- In the final stage, pairs of signal hypotheses are compared to each other. A large set of pseudo-experiments were performed, with a maximal likelihood fit done separately for each of the two signal models. The profile log likelihood ratio was used as a test statistic. The distribution of the test statistic was produced for each of the two hypothesis. An Asimov data set was created for each of the two hypotheses. The expected exclusion, under the assumption of a signal model, was obtained from the tail integral of the test statistic distribution. Finally the same procedure is repeated on data.

8.3.6. Expected exclusion (μ=1)

Presented in Table 8.3 are the p-values (probabilities) of expected exclusion for various signal hypothesis with 8 TeV data. The table present both exclusion of $J^p = 0^-, 0_h^+$ and 2_m^+ assuming a Standard Model Higgs (alt columns) and exclusion of a Standard Model Higgs under the alternative models (Null columns). The probabilities are labeled p_0, and the values are also quoted in the corresponding number of Gaussian sigmas. The MC toy distributions the numbers are derived from are found in Fig. 8.7. In Tables 8.4 and 8.5 are the corresponding numbers for the 7 TeV and 7+8TeV-combined datasets respectively. In the latter case only the expected exclusion of the non Standard Model are presented.

Similar results are reported for 7 TeV only and 7 TeV, 8 TeV combined in Tab. 8.4 and Tab. 8.5 respectively. The results quoted are obtained using the profile log likelihood ratio as the test statistic. The separations shown are evaluated assuming the signal strength parameter μ=1. The corresponding results for the 7+8 TeV combined dataset, calculated not assuming a common signal strengh can be found in Table **??**, where it is seen that the effect is neglible.

The study was repeated assuming a signal strength of $\mu = 1.44$ in agreement with what was observed in data by the dedicated analysis [8].

8.3.7. Expected separation significance (μ=1) for the spin 2 samples with non-universal couplings

Table 8.3. The expected exclusion for 8 TeV only of different alternative spin and parity models for the BDT analysis. The exclusions are given in terms of p-values and corresponding number of Gaussian sigmas. The 'alt' numbers reported are where a Standard Model Higgs $J^p = 0^+$ is assumed and the alternative model is excluded. The 'Null' numbers assume a alternative model and excludes the Standard Model Higgs hypothesis. The stated values take into account all the systematic uncertanties that are evaluated to be significant (impact $\geq 0.45\%$). The numbers in parenthesis indicate the values when not taking systematic uncertainties into account. The impact of including all significanct nuisance parameters is 3.8%, 7.0% and 5.0% for excluding $J^p = 0^-$, $J^p = 0^+_h$ and $J^p = 2^+_m$ respectively. The values are derived from MC toy distributions and as such have a related statistical uncertainty. The statistical uncertainty on the significances corresponds to 0.01 sigma and equvalently is of the size of the last reported digit of the p-values.

$\sqrt{s} = 8$ TeV

Separated Hypotheses (Alt, Null)	p_0-Alt	σ-Alt	p_0-Null	σ-Null
$J^p = 0^-,\ 0^+$	0.0107 (0.0085)	2.30 (2.39)	0.0147 (0.0103)	2.18 (2.31)
$J^p = 0^+_h,\ 0^+$	0.0425 (0.0318)	1.72 (1.85)	0.0508 (0.0394)	1.64 (1.76)
$J^p = 2^+_m,\ 0^+$	0.0292 (0.0231)	1.89 (1.99)	0.0451 (0.0367)	1.69 (1.79)

Table 8.4. The expected exclusion for 7 TeV-only of different alternative spin and parity models for the BDT analysis. The exclusions are given in terms of p-values and corresponding number of Gaussian sigmas. The 'alt' numbers reported are where a Standard Model Higgs $J^p = 0^+$ is assumed and the alternative model is excluded. The stated values take into account the all systematic uncertanties that are evaluated to be significant (impact $\geq 0.45\%$). The numbers in parenthesis indicate the values when not taking systematic uncertainties into account. The values are derived from MC toy distributions and as such have a related statistical uncertainty. The statistical uncertainty on the significances corresponds to 0.01 sigma (0.02 $J^p = 0^-,\ 0^+$ w.o syst.) and equvalently is of the size of the last reported digit of the p-values.

$\sqrt{s} = 7$ TeV

Separated Hypotheses (Alt, Null)	p_0-Alt	σ-Alt
$J^p = 0^-,\ 0^+$	0.136 (0.126)	1.10 (1.15)
$J^p = 0^+_h,\ 0^+$	0.185 (0.177)	0.90 (0.93)
$J^p = 2^+_m,\ 0^+$	0.170 (0.158)	0.95 (1.00)

Table 8.5. The expected exclusion for 7 and 8 TeV-combined of different alternative spin and parity models for the BDT analysis. The exclusions are given in terms of p-values and corresponding number of Gaussian sigmas. The 'alt' numbers reported are where a Standard Model Higgs $J^p = 0^+$ is assumed and the alternative model is excluded. The stated values take into account the all systematic uncertanties that are evaluated to be significant (impact $\geq 0.45\%$). The numbers in parenthesis indicate the values when not taking systematic uncertainties into account. The values are derived from MC toy distributions and as such have a related statistical uncertainty. The statistical uncertainty on the significances corresponds to at most 0.04 sigma and equvalently is of the size of the last reported digit of the p-values.

$\sqrt{\mathrm{s}} = 7 + 8$ TeV

Separated Hypotheses (Alt, Null)	p_0-Alt	σ-Alt
$J^p = 0^-,\ 0^+$	0.0083 (0.0067)	2.40 (2.47)
$J^p = 0_h^+,\ 0^+$	0.038 (0.030)	1.77 (1.89)
$J^p = 2_m^+,\ 0^+$	0.0141 (0.024)	1.98 (2.19)

In the case of the spin-two studies, hypothesis testing is performed for two benchmark models with two cutoffs on the 4 leptons transverse momentum (p_{T4l}) of 125 GeV and 300 GeV:

- low quark fraction sample with $k_g = 1$ and $k_q = 0$
- low gluon fraction sample with $k_g = 0.5$ and $k_q = 1$

where k_g and k_q are scale factors applied to the Higgs boson coupling to gluons and quarks respectively, which correspond to deviations from the SM Higgs coupling. The expected significance and p_0 corresponding to the exclusion of the spin 2 samples with non univarsal coupling at the $8TeV$ are reported in Table 8.6. The Table 8.6 presents the exclusion of the considered hypothesis assuming a Standard Model Higgs. The exclusions are given in terms of p-values and corresponding number of Gaussian sigmas. The expected exclusion of the non Standard Model are presented. The stated values take into account the all systematic uncertanties that are evaluated to be significant (impact $\geq 0.45\%$). The values are derived from MC toy distributions and as such have a related statistical uncertainty. In Tables 8.7 and 8.8 are the corresponding numbers for the 7 TeV and 7+8TeV-combined datasets respectively.

Table 8.6. The expected exclusion for 8 TeV only of different alternative spin and parity models for the BDT analysis. The exclusions are given in terms of p-values and corresponding number of Gaussian sigmas. The 'alt' numbers reported are where a Standard Model Higgs $J^p = 0^+$ is assumed and the alternative model is excluded. The stated values take into account the all systematic uncertanties that are evaluated to be significant (impact $\geq 0.45\%$). The numbers in parenthesis indicate the values when not taking systematic uncertainties into account. The values are derived from MC toy distributions and as such have a related statistical uncertainty.

$\sqrt{s} = 8$ TeV

Separated Hypotheses	p_0-Alt	σ-Alt
$J^p = 2^+\ k_g = 0.5\ k_q = 1\ p_{T4l} < 125\ GeV,\ 0^+$	0.071 ± 0.001	1.47 ± 0.01
$J^p = 2^+\ k_g = 0.5\ k_q = 1\ p_{T4l} < 300\ GeV,\ 0^+$	0.059 ± 0.001	1.56 ± 0.01
$J^p = 2^+\ k_g = 1\ k_q = 0\ p_{T4l} < 125\ GeV,\ 0^+$	0.066 ± 0.001	1.51 ± 0.01
$J^p = 2^+\ k_g = 1\ k_q = 0\ p_{T4l} < 300\ GeV,\ 0^+$	0.050 ± 0.001	1.64 ± 0.01

Table 8.7. The expected exclusion for 7 TeV only of different alternative spin and parity models for the BDT analysis. The exclusions are given in terms of p-values and corresponding number of Gaussian sigmas. The 'alt' numbers reported are where a Standard Model Higgs $J^p = 0^+$ is assumed and the alternative model is excluded. The stated values take into account the all systematic uncertainties that are evaluated to be significant (impact $\geq 0.45\%$). The numbers in parenthesis indicate the values when not taking systematic uncertainties into account. The values are derived from MC toy distributions and as such have a related statistical uncertainty.

$\sqrt{\mathrm{s}} = 7$ TeV

Separated Hypotheses	p_0-Alt	σ-Alt
$J^p = 2^+\ k_g = 0.5\ k_q = 1\ p_{T4l} < 125\ GeV,\ 0^+$	0.213 ± 0.002	0.80 ± 0.01
$J^p = 2^+\ k_g = 0.5\ k_q = 1\ p_{T4l} < 300\ GeV,\ 0^+$	0.208 ± 0.002	0.81 ± 0.01
$J^p = 2^+\ k_g = 1\ k_q = 0\ p_{T4l} < 125\ GeV,\ 0^+$	0.213 ± 0.002	0.80 ± 0.01
$J^p = 2^+\ k_g = 1\ k_q = 0\ p_{T4l} < 300\ GeV,\ 0^+$	0.208 ± 0.002	0.81 ± 0.01

Table 8.8. The expected exclusion for 7+8 TeV only of different alternative spin and parity models for the BDT analysis. The exclusions are given in terms of p-values and corresponding number of Gaussian sigmas. The 'alt' numbers reported are where a Standard Model Higgs $J^p = 0^+$ is assumed and the alternative model is excluded. The stated values take into account the all systematic uncertainties that are evaluated to be significant (impact $\geq 0.45\%$). The numbers in parenthesis indicate the values when not taking systematic uncertainties into account. The values are derived from MC toy distributions and as such have a related statistical uncertainty.

$\sqrt{\mathrm{s}} = 7 + 8$ TeV

Separated Hypotheses	p_0-Alt	σ-Alt
$J^p = 2^+\ k_g = 0.5\ k_q = 1\ p_{T4l} < 125\ GeV,\ 0^+$	0.059 ± 0.001	1.56 ± 0.01
$J^p = 2^+\ k_g = 0.5\ k_q = 1\ p_{T4l} < 300\ GeV,\ 0^+$	0.047 ± 0.001	1.68 ± 0.01
$J^p = 2^+\ k_g = 1\ k_q = 0\ p_{T4l} < 125\ GeV,\ 0^+$	0.055 ± 0.001	1.60 ± 0.01
$J^p = 2^+\ k_g = 1\ k_q = 0\ p_{T4l} < 300\ GeV,\ 0^+$	0.042 ± 0.001	1.73 ± 0.01

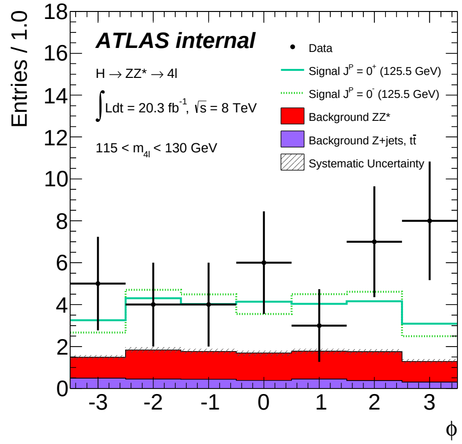

(a)

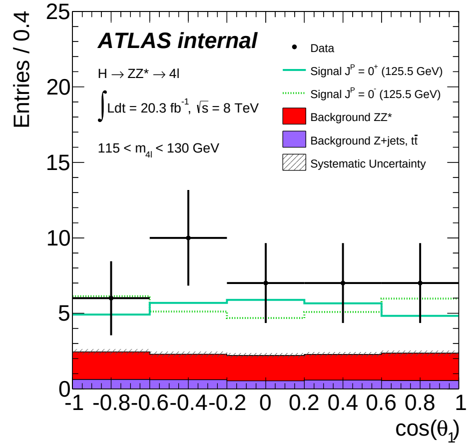

(b)

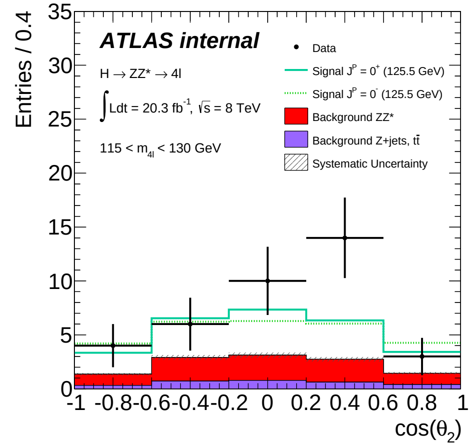

(c)

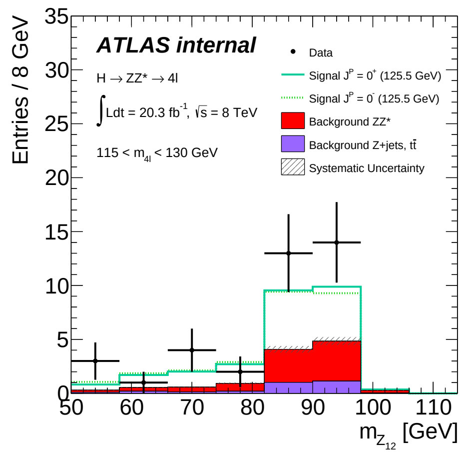

(d)

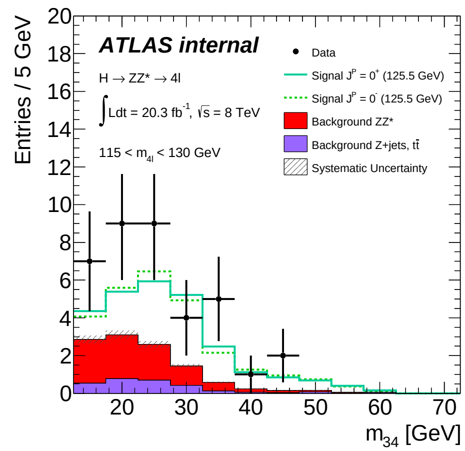

(e)

Figure 8.1. Distributions of spin and parity sensitive observables for events selected by the main analysis in the signal mass range: 115GeV $\leq m_{4\ell} \leq$ 130GeV. The expected contributions from the signal (0^+ and 0^-) and irreducible ZZ background are shown, normalized to the expected number of events for the luminosity of the data sample. The contributions from reducible non-ZZ backgrounds, which are derived using data and normalized to the luminosity of the data sample, are also shown. (a) ϕ, (b) $\cos\theta_1$,(c) $\cos\theta_2$, (d) m_{12}, (e) m_{34}.

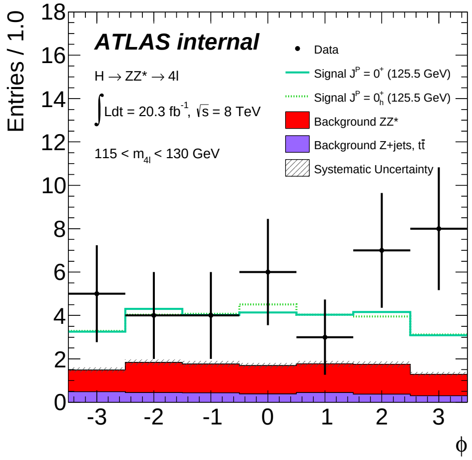

(a)

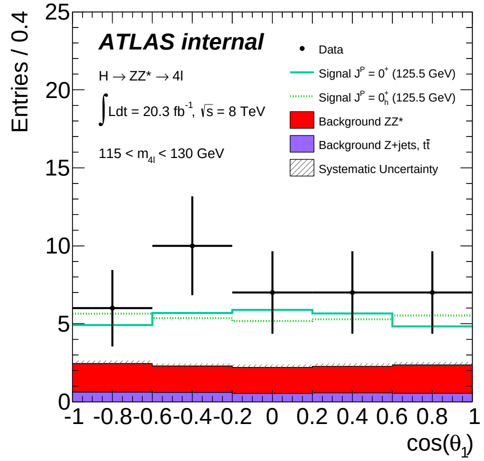

(b)

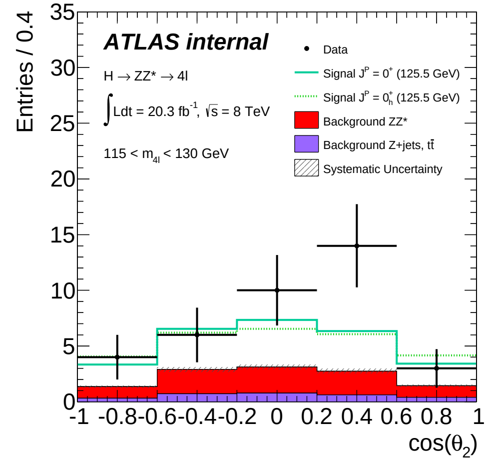

(c)

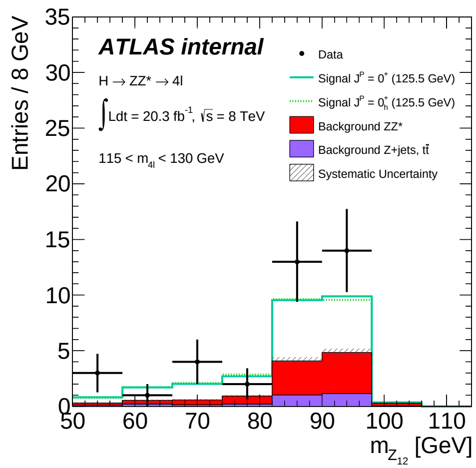

(d)

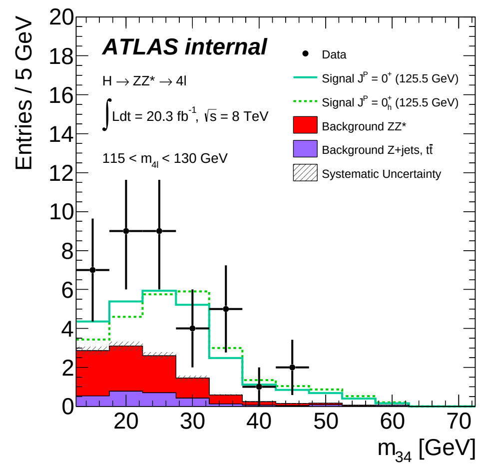

(e)

Figure 8.2. Distributions of spin and parity sensitive observables for events selected by the main analysis in the signal mass range: $115\text{GeV} \leq m_{4\ell} \leq 130\text{GeV}$. The expected contributions from the signal (0^+ and 0_h^+) and irreducible ZZ background are shown, normalized to the expected number of events for the luminosity of the data sample. The contributions from reducible non-ZZ backgrounds, which are derived using data and normalized to the luminosity of the data sample, are also shown. (a) ϕ, (b) $\cos\theta_1$,(c) $\cos\theta_2$, (d) m_{12}, (e) m_{34}.

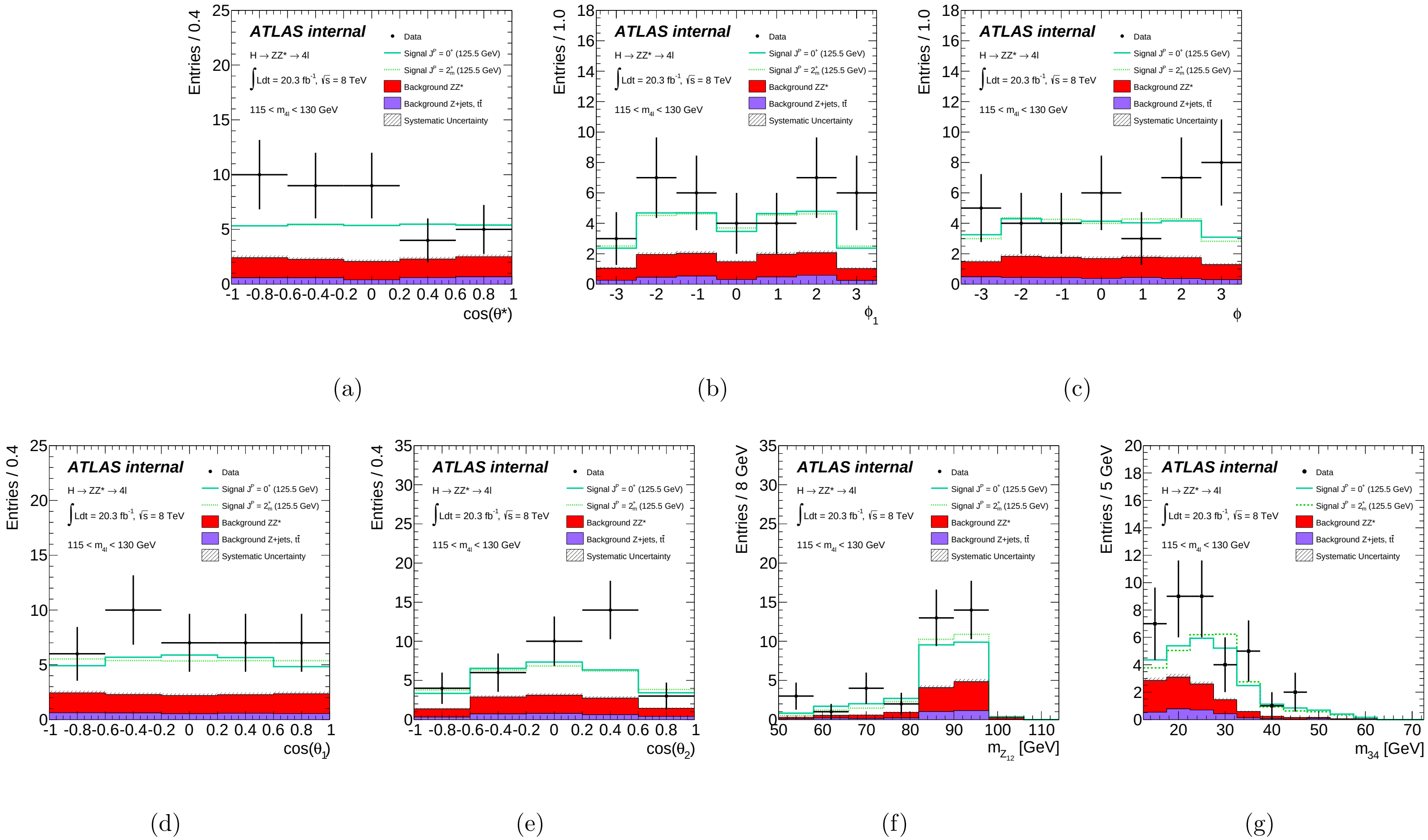

Figure 8.3. Distributions of spin and parity sensitive observables forevents selected by the main analysis in the signal mass range: $115\text{GeV} \leq m_{4\ell} \leq 130\text{GeV}$. The expected contributions from the signal (0^+ and 2^+_m) and irreducible ZZ background are shown, normalized to the expected number of events for the luminosity of the data sample. The contributions from reducible non-ZZ backgrounds, which are derived using data and normalized to the luminosity of the data sample, are also shown. (a) $\cos\theta^*$, (b) ϕ_1, (c) ϕ, (d) $\cos\theta_1$,(e) $\cos\theta_2$, (f) m_{12}, (g) m_{34}.

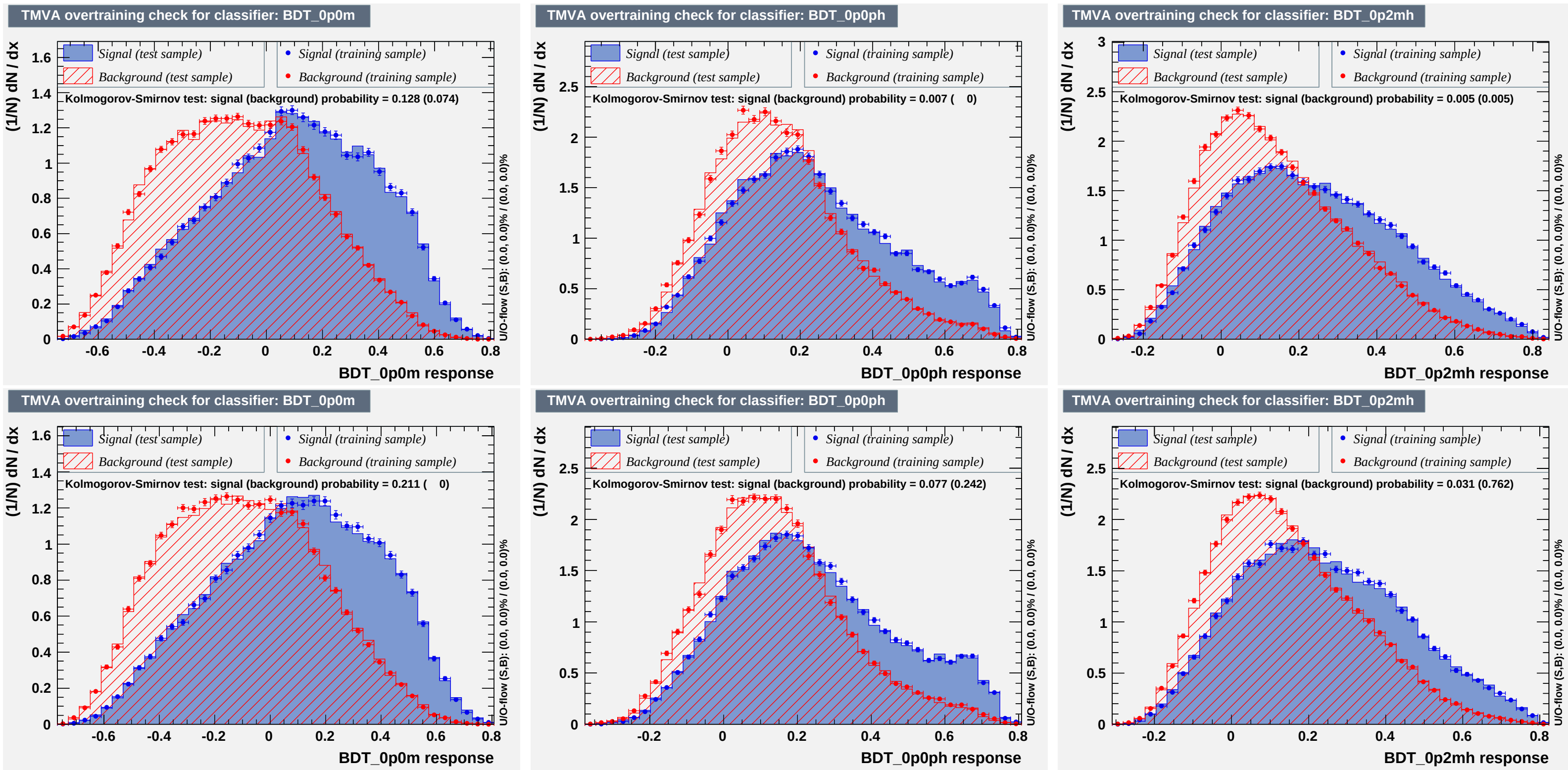

Figure 8.4. BDT distributions for $J^p = 0^+$ vs. $J^p = 0^-$, discrimination (left column), $J^p = 0^+$ vs. $J^p = 0^+_h$ discrimination (middle column) and $J^p = 0^+$ vs. $J^p = 2^+_m$ discrimination (right column). The top row show the training as perform on the 8 TeV (2012) MC, while the bottom row shows the corresponding figures for 7 TeV (2011). The BDT training is performed on an mixture of the four different final states corresponding to their expected normalisations. In all cases, the 0^+ hypothesis is labeled as signal while the alternative distribution is labeled as background. The samples are divided in two; a test and a training sample. The BDT optimisation has been done on the training sample and overtraining is evaluated by comparing the resulting ROC integrals as presented in Tab. 8.2.

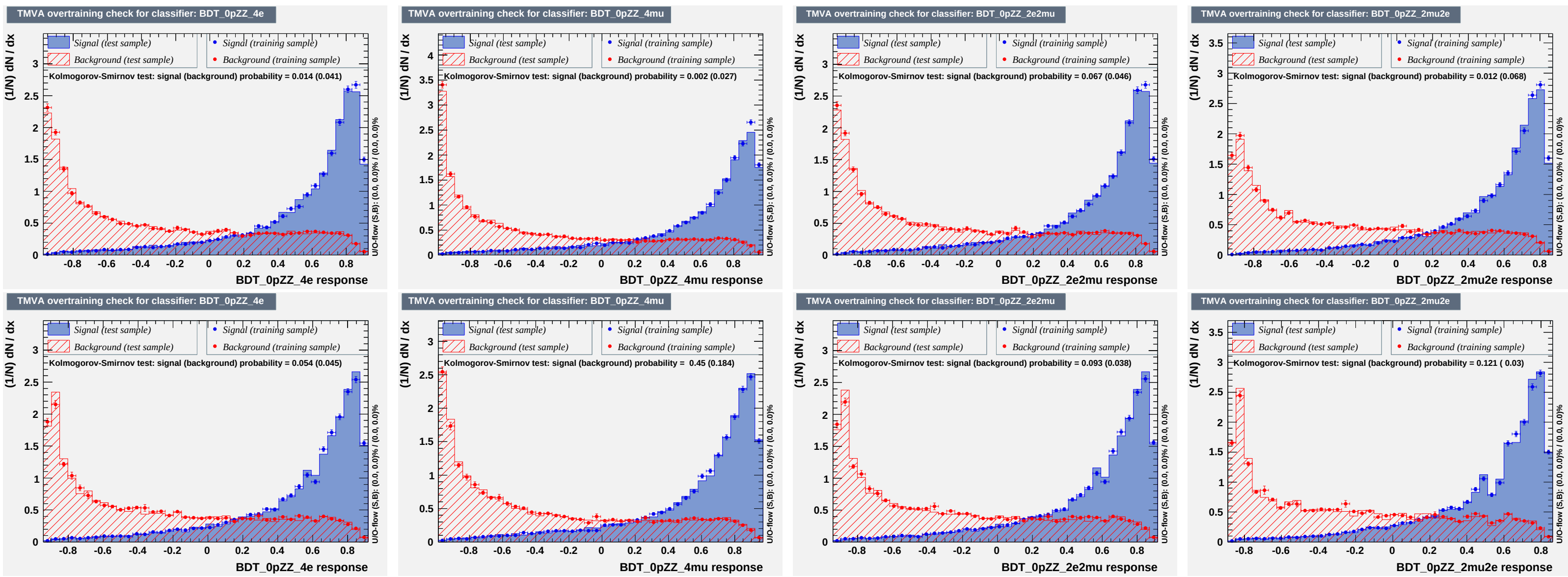

Figure 8.5. BDT distributions for the $J^p = 0^+$ vs. ZZ-continuum discriminant. The BDT training is performed per final state, where the columns from left to right shows the 4e, 4μ, $2e2\mu$, $2\mu 2e$ final states. The top row show the training as perform on the 8 TeV (2012) MC, while the bottom row shows the corresponding figures for 7 TeV (2011). In all cases, the 0^+ hypothesis is labeled as signal while the ZZ-continuum distribution is labeled as background. The samples are divided in two; a test and a training sample. The BDT optimisation has been done on the training sample and overtraining is evaluated by comparing the resulting ROC integrals as presented in Tab. 8.2.

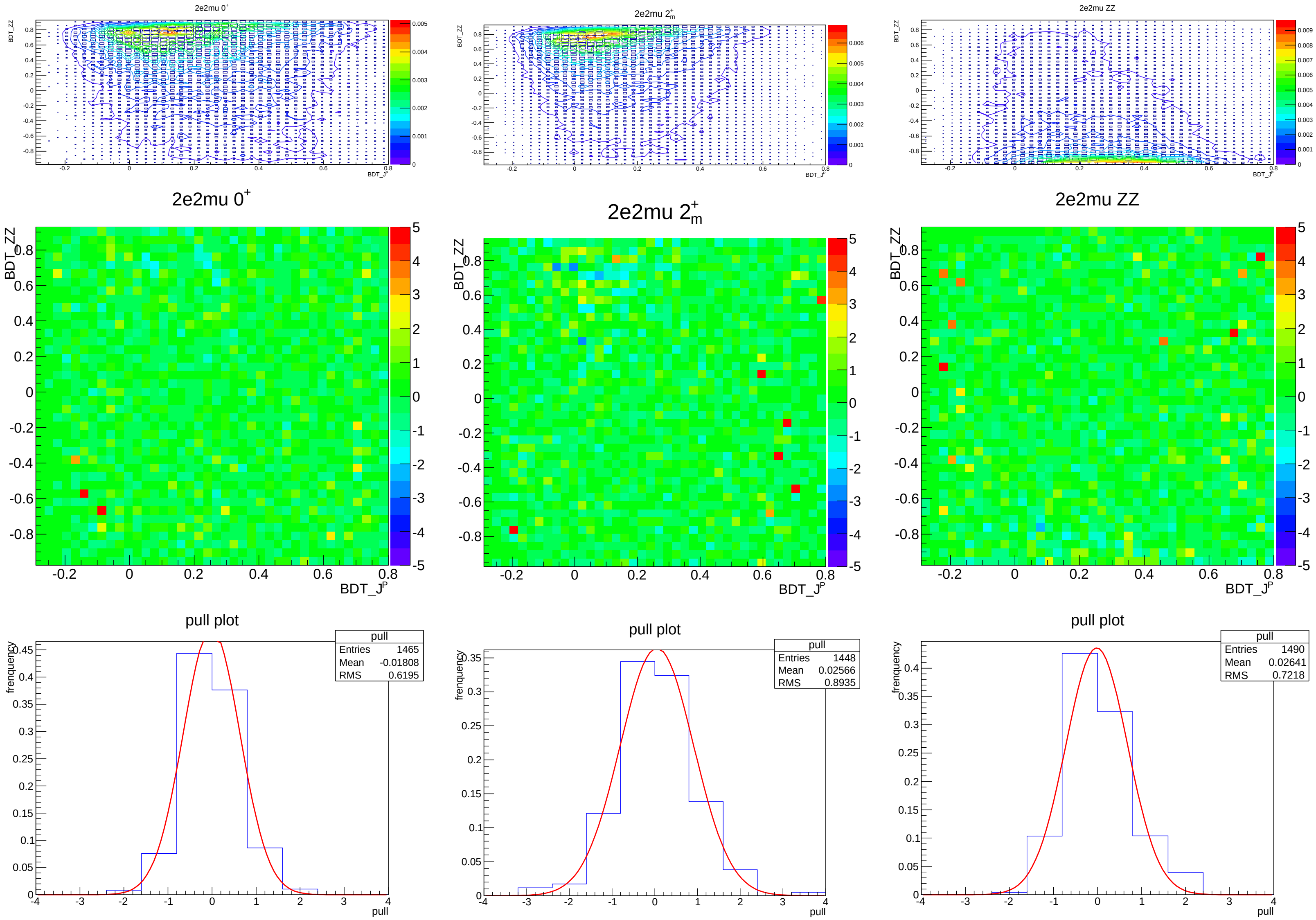

Figure 8.6. Example of validation of the KDE procedure. The presented figures are taken from the $2e2\mu$ final state. Top row: Two dimensional distributions of $J^p = 0^+$ vs $J^p = 2^+_m$ (first axis) and $J^p = 0^+$ vs ZZ^* (second axis) for process types $J^p = 0^+$ (left column), $J^p = 2^+_m$ (middle column) and ZZ^* (right row). The scatter indicate the simulated Monte Carlo events, while the contours show the smoothed distribution arrived at with the KDE approach. Center row: The color of each bin shows the difference between the event distribution and smoothed KDE distribution from above in units of the statistical uncertainty. The corresponding pull distribution for each process type is found in the bottom row. It is seen that the center of each is close to zero and width close to one.

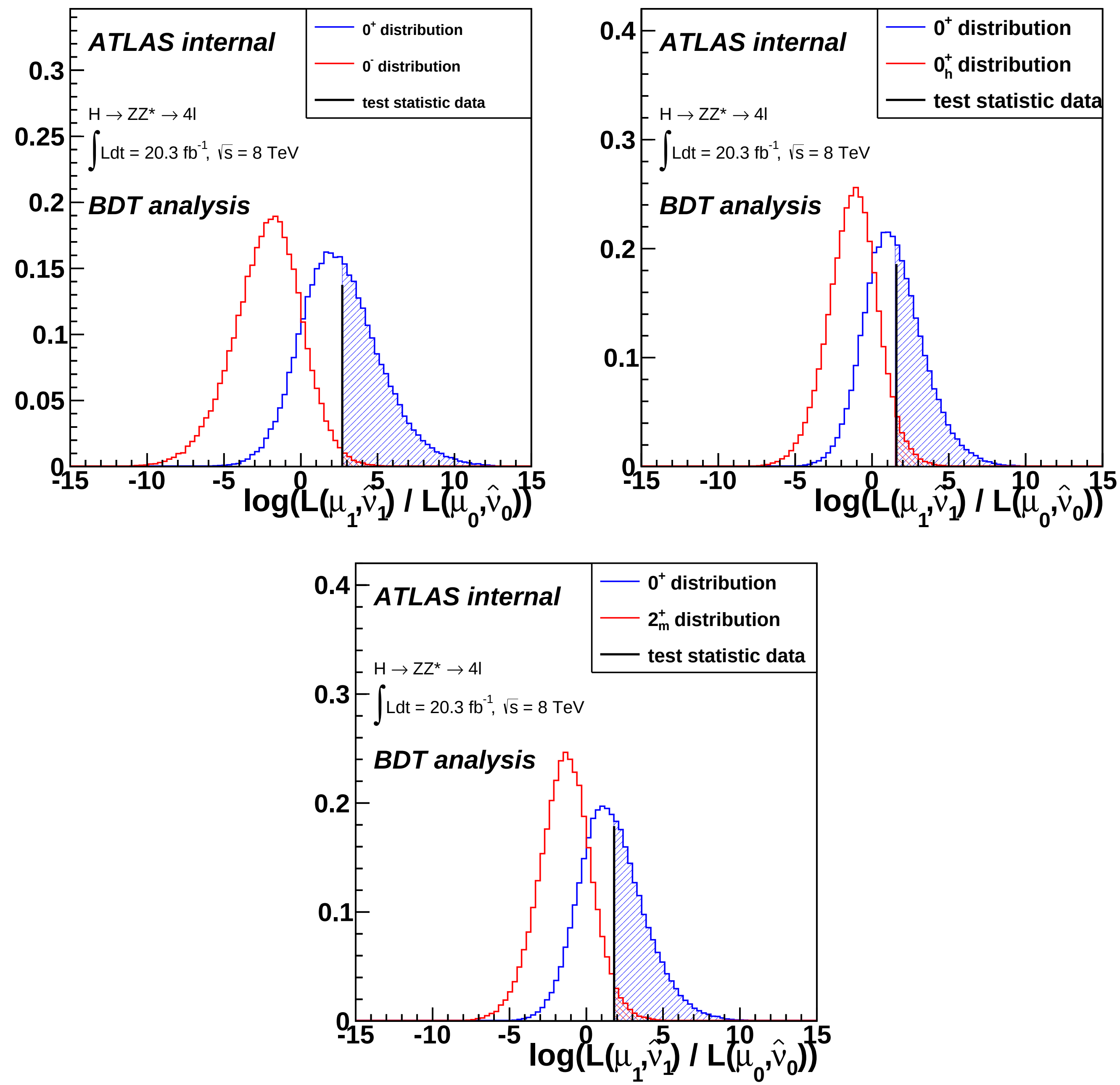

Figure 8.7. MC toys distributions for the different hypothesis tests performed. The three figures from left to right show, $J^p = 0^-,\ 0^+$, $J^p = 0^+_h,\ 0^+$ and $J^p = 2^+_m,\ 0^+$. The test statistic values are calculated as described in Sec. 8.2. In each figure a Standard Model Higgs is assumed and its value indicated by 'test statistic data'. The reported p-values correspond to the tail integral of the alternative models.

Chapter 9

Results

9.1. Results of spin and parity measurement

Figure 9.1 presents a comparison of the J^P 0^+ hypothesis with the 2^+_m hypothesis as a function of the fraction of $q\bar{q}$ in a mixed $q\bar{q}$ and ggF production varying from 0 to 100%. There is little variation in the expected discrimination as a function of the $q\bar{q}$ fraction.

The expected and observed $\mathrm{p_0}$-values when assuming the spin-0^+ hypothesis and testing the 0, 1^+, 1, 2^+_m and 2 hypotheses are presented in Table 9.1. The Table also shows the observed $\mathrm{p_0}$-values when assuming the alternative hypotheses and testing the spin-0^+. The statistical separation between the pairs of hypotheses expressed as a $\mathrm{CL_S}$ confidence level is also provided. The $\mathrm{CL_S}$ is calculated from the observed p0-values for each alternative J^P hypothesis when 0^+ is assumed and the $\mathrm{p_0}$-value of the 0^+ hypothesis when assuming the alternatives, i.e. as $\mathrm{CL_S}$=$\mathrm{p_0}$(alternative J^P)/(1 $\mathrm{p_0}$(0^+)). The results are shown for both the BDT analysis and for the $\mathrm{J^p} - \mathrm{MELA}$ analysis. These results correspond to the combined statistics of $sqrts = 8$ TeV and $\sqrt{s} = 7$ TeV data sets. The profile likelihood is computed including all sources of systematic uncertainty, and allowing the signal strength μ to vary.

It can be observed that the expected sensitivity to discriminate between the Standard Model 0^+ hypothesis and 0, 1^+, 1 and 2 is above the 2.5σ level, while the expected discrimination against 2^+_m is approximately 1.5σ. Both the BDT and $\mathrm{J^p} - \mathrm{MELA}$ approaches show similar expected sensitivity. The observed $\mathrm{p_0}$-values of

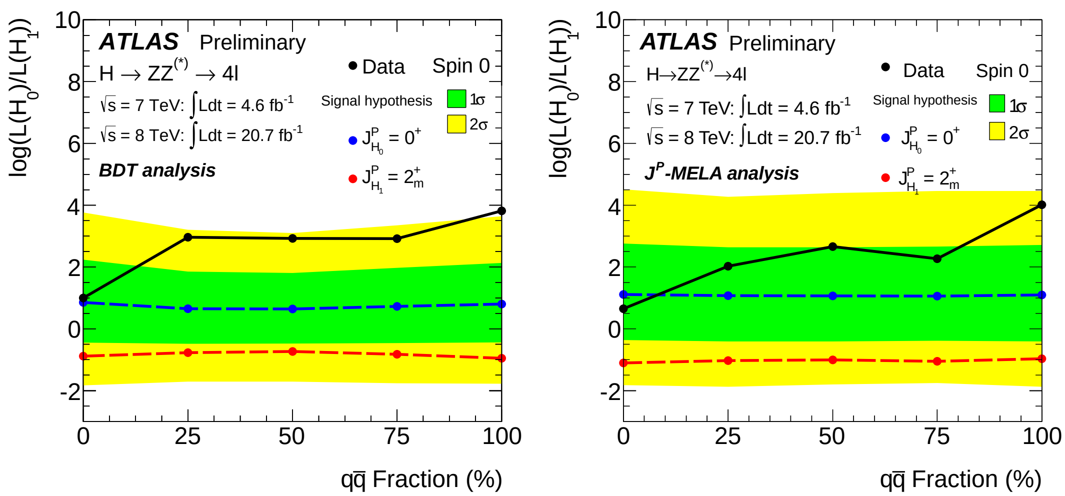

Figure 9.1. Variation of the medians of the log-likelihood ratio distribution generated for varying fractions of $q\bar{q}$ in a mixed $q\bar{q}$ and ggF production for testing the 2^+_m hypothesis when assuming the spin-0^+ hypothesis. Each distribution is generated with more than 500k Monte Carlo experiments. In each experiment the expected numbers of signal and background events are fixed to the observed yields. The blue and red data points correspond to the median values for the 0^+ and 2^+_m hypotheses, respectively, for each fraction. The black points represent the log-likelihood values observed in data. The lines connecting the points are there to guide the eye.

these analyses favour the SM J^P=0^+ hypothesis with respect to 0, 1^+, 1 and 2^+_m. The expected separation for 2 is above 2.6σ, but the observed compatibility with the 0^+ hypothesis renders the result inconclusive. When the 2^+ hypothesis is compared to 0^+ a 1 $\mathrm{CL_S}$ value of 81.8%(83.2%) for the $\mathrm{J^P} - \mathrm{MELA(BDT)}$ analysis is obtained, assuming purely ggF production. The 0, 1^+ and 1 hypotheses are excluded at the 99.6%(97.8%), 99.4%(99.8%) and 96.9%(94.0%) $\mathrm{CL_S}$ confidence levels, respectively, in favour of 0^+ for the $\mathrm{J^P} - \mathrm{MELA(BDT)}$ analyses.

		BDT analysis				$\mathrm{J^P}-\mathrm{MELA}$ analysis			
		tested J^P for an assumed 0^+		tested 0^+ for an assumed J^P	$\mathrm{CL_S}$	tested J^P for an assumed 0^+		tested 0^+ for an assumed J^P	$\mathrm{CL_S}$
		expected	observed	observed*		expected	observed	observed*	
0^-	$\mathrm{p_0}$	0.0037	0.015	0.31	0.022	0.0011	0.0022	0.40	0.004
1^+	$\mathrm{p_0}$	0.0016	0.001	0.55	0.002	0.0031	0.0028	0.51	0.006
1^-	$\mathrm{p_0}$	0.0038	0.051	0.15	0.060	0.0010	0.027	0.11	0.031
2^+_m	$\mathrm{p_0}$	0.092	0.079	0.53	0.168	0.064	0.11	0.38	0.182
2^-	$\mathrm{p_0}$	0.0053	0.25	0.034	0.258	0.0032	0.11	0.08	0.116

Table 9.1. For an assumed 0^+ hypothesis $\mathrm{H_0}$, the values for the expected and observed $\mathrm{p_0}$-values of the different tested spin and parity hypotheses $\mathrm{H_1}$ for the BDT and $\mathrm{J^P}-\mathrm{MELA}$ analyses. The results are given combining the $\sqrt{s} = 7\mathrm{TeV}$ and $\sqrt{s} = 8\mathrm{TeV}$ data sets. Also given is the observed $\mathrm{p_0}$-value where 0^+ is the test hypothesis and the other spins states are the assumed hypothesis(observed*). These two observed $\mathrm{p_0}$-values are combined to provide the $\mathrm{CL_S}$ confidence level for each test hypothesis. The production mode is assumed to be 100% ggF.

9.2. Results of Higgs properties measurements at $H \to ZZ^* \to 4\ell$

Updated search results for the newly observed Higgs-like boson have been presented for the $H \to ZZ^* \to 4\ell$ channel, using data corresponding to integrated luminosities of 4.6 fb^{-1} at $\sqrt{s}$ = 7TeV and 20.7 fb^{-1} at $\sqrt{s}$ = 8TeV recorded by the ATLAS detector. An excess of events over the background is observed with the minimum p_0 of 2.7×10^{11}(6.6 standard deviations) appearing at m_H =124.3 GeV. This channel alone now surpasses the 5σ discovery significance. The best fitted mass is $m_H = 124.3\, ^{+0.6}_{\ 0.5}$(stat) $^{+0.5}_{\ 0.3}$(syst) GeV, and the signal strength (the ratio of the observed cross section to the expected SM cross section) of the Higgs-like boson at this mass is found to be $\mu = 1.7\, ^{+0.5}_{\ 0.4}$.

For the first time the $H \to ZZ^* \to 4\ell$ candidate events have been categorised, allowing the study of Higgs boson couplings via the separation of ggF/$t\bar{t}H$ and VBF/VH production. A VBF-like candidate has been found at 123.5 GeV, where approximately 0.4 VBF events are expected with S/B around 1 if ggF Higgs boson production is counted as background.

Finally, an updated analysis of the spin and parity of the new particle has been presented. Hypothesis tests comparing the SM 0^+ JP hypothesis with 0, 1^+, 1, 2^+_m and 2 have been performed, assuming purely ggF production. The 0^+ hypothesis has also been compared to the 2^+_m hypothesis for varying fractions of ggF and $q\bar{q}$ production. The expected separation is found to be independent of the production fractions. The Higgs-like boson is found to be compatible with the SM expectation of 0^+ when compared pair-wise with 0, 1^+, 1, 2^+, and 2. The 0 and 1^+ states are excluded at the 97.8% confidence level or higher using CL_S in favour of 0^+.

Chapter 10

Conclusions

10.1. Establishing the New Boson as the Higgs Boson Using ATLAS Data

The ATLAS collaboration has presented three independent studies of the spin of the new resonance. The separation between the Standard Model $J^P = 0^+$ and alternative hypotheses was studied in the bosonic decay channels $H \to \gamma\gamma$[4], $H \to WW^* \to \ell\nu\ell\nu$[6] and $H \to ZZ^* \to 4\ell$ which has been discussed in the previous chapters. The full 2012 dataset collected at $\sqrt{s} = 8$ TeV, corresponding to an integrated luminosity of about 21 fb^1, is used for all three analyses. For the analysis of the $H \to ZZ^* \to 4\ell$ channel, an additional dataset corresponding to an integrated luminosity of 4.8 fb^1 collected at $\sqrt{s} = 7$ TeV is added. The observed final states are assumed to be produced in the decay of a single particle with a mass of 125.5 GeV[3]. The spin information is extracted from kinematic observables constructed from the final state particles in each of the channels considered.

By end of 2013, a combination of the spin studies performed in the three decay channels is presented. The focus is discrimination between the Standard Model assignment of $J^P = 0^+$ and a specific $J^P = 2^+$ graviton-inspired model with minimal couplings to Standard Model particles. Since a spin-2 particle can be produced via both the gluon fusion process (gg) and the quark-antiquark annihilation ($q\bar{q}$) process, the studies are generalized and admixtures of $q\bar{q}$ production between 0 and 100% are considered.

Table 10.1 shows the expected and observed p_0 values for both the $J^P = 0^+$ and $J^P = 2^+$ hypotheses for the combination of the $H \to \gamma\gamma$, $H \to WW^* \to \ell\nu\ell\nu$ and $H \to ZZ^* \to 4\ell$ channels. The results are shown as a function of the $q\bar{q}$ spin-2 production fraction. The compatibility of each spin hypothesis with the data is shown in Figure 10.1. The test statistic calculated on data is compared to the corresponding expectations obtained from pseudo-experiments, as a function of $f_{q\bar{q}}$. The number of pseudo-experiments performed to determine the distributions of the test statistics amount to 100k for the $J^P = 0^+$ and 1 million for the $J^P = 2^+$ hypothesis.

Table 10.1. Main parameters of the inner-detector syste

$f_{q\bar{q}}$	Spin-2 assumed exp. $p_0(J^P{=}0^+$	Spin-0 assumed exp. $p_0(J^P{=}2^+)$	obs. $p_0(J^P{=}0^+)$	obs. $p_0(J^P{=}2^+)$	$\mathrm{CL}_s(J^P{=}2^+)$
100%	3.4×10^{-3}	9.4×10^{-5}	0.82	0.4×10^{-5}	0.2×10^{-4}
75%	1.0×10^{-2}	1.1×10^{-3}	0.82	3.7×10^{-5}	2.1×10^{-4}
50%	1.5×10^{-2}	3.5×10^{-3}	0.85	9.1×10^{-5}	6.0×10^{-4}
25%	6.8×10^{-3}	2.4×10^{-3}	0.81	1.0×10^{-4}	5.3×10^{-4}
0%	1.6×10^{-3}	6.1×10^{-4}	0.65	1.4×10^{-4}	4.0×10^{-4}

The data are in good agreement with the Standard Model $J^P = 0^+$ hypothesis. The observed values in Figure 10.1(a) are, however, found to be above the $J^P = 0^+$ median values. This effect can be attributed to the aforementioned statistical fluctuation in the data of the $H \to ZZ^* \to 4\ell$ decay channel.

Figure 10.2 shows the comparison of the expected and observed $\mathrm{CL}_s(J^P = 2^+)$ as a function of $f_{q\bar{q}}$. The expected exclusion of the spin-2 hypothesis shows only a weak dependence on $f_{q\bar{q}}$, due to the complementary sensitivities of the channels to the different production mechanisms of the spin-2 resonance, the observed exclusion of the $J^P = 2^+$ state in favor of the Standard Model $J^P = 0^+$ hypothesis exceeds

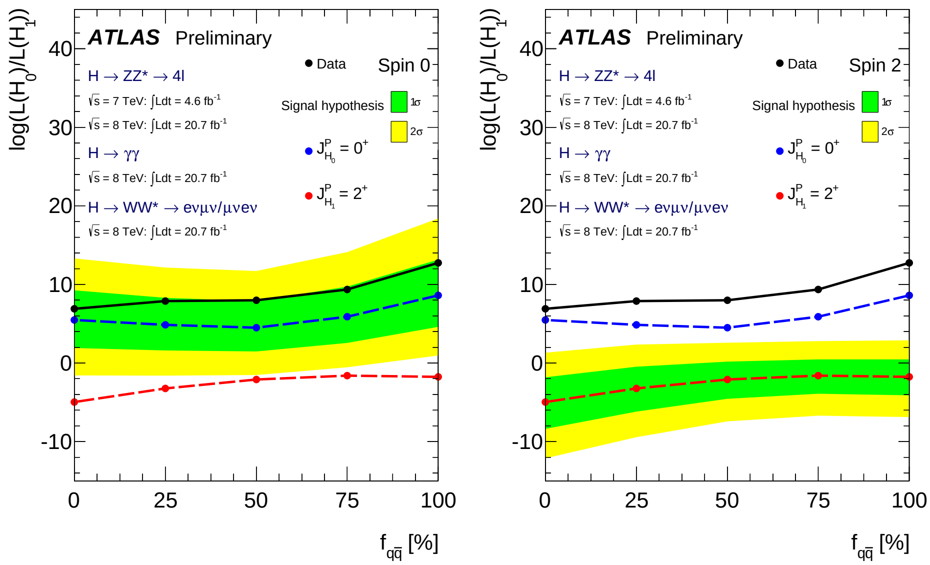

(a) (b)

Figure 10.1. Expected and observed ratio of profiled likelihoods for the combination of channels as a function of the fraction of the $q\bar{q}$ spin-2 production mechanism. The green and yellow bands represent, respectively, the one and two standard deviation bands for the $J^P = 0^+$ (a) and for the $J^P = 2^+$ (b) hypotheses.[5]

99.9% CL for all values of $f_{q\bar{q}}$.

10.2. Conclusion of combination

The Standard Model assignment of $J^P = 0^+$ is compared to a graviton-inspired $J^P = 2^+$ model with minimal couplings to Standard Model particles. The data are in good agreement with the expected distributions of a $J^P = 0^+$ particle while the graviton-inspired $J^P = 2^+$ model, that is expected to be produced dominantly via the gluon fusion process, is excluded at more than 99.9% confidence level. The most general spin-2 model involves a large number of parameters to fully describe the couplings of this resonance particle to the initial and final states relevant for the

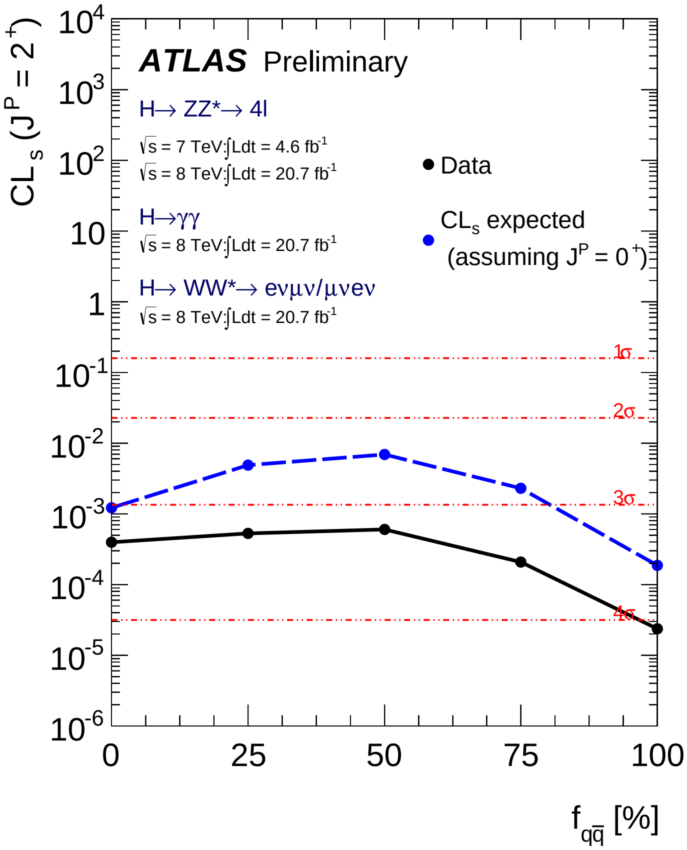

Figure 10.2. Expected (blue dashed line) and observed (black solid line) confidence level, $\mathrm{CL}_s(J^P = 2^+)$, of the $J^P = 2^+$ hypothesis as a function of the fraction of $q\bar{q}$ production of the spin-2 particle.[5]

measurement of the spin. The analysis shown here does not address this general case. However, this study was extended to arbitrary admixtures of gluon fusion and $q\bar{q}$ production processes between 0 and 100%. In this extended study all $J^P = 2^+$ production admixtures are excluded by the data at more than 99.9% confidence level. [5]

10.3. Outlook and Prospects for Future Measurements

To study the new boson - Higgs, we have to do more measurements. We have to update the spin and parity measurement. Also more mass and coupling measurements are needed. In the future, we will understand the new boson much better.

Appendix A

APPENDIX

A.1. Physical Constants and Conversion Factors

Precisely known physical constants:

$$c = 2.998 \times 10^{10} \text{ cm/s}$$

$$\hbar = 6.582 \times 10^{-22} \text{ MeV}\cdot\text{s}$$

$$e = -1.602 \times 10^{-19} \text{ C}$$

$$\alpha = \tfrac{e^2}{4\pi\hbar c} = \tfrac{1}{137.04} = 0.00730$$

$$\tfrac{G_F}{(\hbar c)^3} = 1.166 \times 10^{-5} \text{GeV}^{-2}$$

Particle masses (times c^2):

e: 0.5110 MeV	p: 938.3 MeV
μ: 105.6 MeV	n: 939.6 MeV
τ: 1777 MeV	$\pi^{\pm}$: 139.6 MeV
$W^{\pm}$: 80.2 GeV	π^0: 135.0 MeV
Z^0: 91.19 GeV	

Useful combinations:

Bohr radius: $\alpha_0 = \frac{\hbar}{\alpha m_e c} = 5.292 \times 10^{-9}$ cm

electron Compton wavelength: $\lambda\!\!\!^{-} = \frac{\hbar}{m_e c} = 3.862 \times 10^{-11}$ cm classical electron radius: $r_e = \frac{\alpha\hbar}{m_e c} = 2.818 \times 10^{-13}$ cm

Thomson cross section: $\sigma_T = \frac{8\pi r_e^2}{3} = 0.6652$ barn

Conversion factors:

$$(1 \text{ GeV})/c^2 = 1.783 \times 10^{-24}\ g$$

$$(1 \text{ GeV})/(\hbar c) = 0.1973 \times 10^{-13} \text{ cm} = 0.1973 \text{ fm}$$

$$(1 \text{ GeV})^{-2}(\hbar c)^2 = 0.3894 \times 10^{-27} \text{ cm}^2 = 0.3894 \text{ mbarn}$$

$$1 \text{ barn} = 10^{-24} \text{ cm}^2$$

$$(1 \text{ volt/meter})(e\hbar c) = 1.973 \times 10^{-25} \text{ GeV}^2$$

$$(1 \text{ tesla})(e\hbar c) = 5.916 \times 10^{-17} \text{ GeV}^2$$

A.2. MC Samples

Tables A.1 and A.2 show the list of MC samples for different signal hypotheses and models of final state interference, respectively, used in this analysis.

A.3. JHU Monte Carlo Validation

The JHU $H \rightarrow ZZ^* \rightarrow 4\ell$ sample with spin/CP 0^+ has been compared with the gg fusion initiated SM Higgs boson production predicted by the POWHEG NLO generator. The validation is performed applying the following acceptance cuts to both samples:

1. - $m_{12} > 50$ GeV and $m_{12} < 106$ GeV;

2. - $m_{34} > 17.5$ GeV;

3. - $|\eta_l| < 2.7$;

Table A.1. MC samples of different signal hypotheses used for the spin-CP analysis.

J^P	$\sqrt{s}$	Dataset
$0^+ : g_1 = 1, g_2 = 0, g_4 = 0$	8 TeV	mc12_8TeV.189606.PowhegJHUPythia8_CT10_ggH125p5_Spin0_g1_1_g2_0_g4_0_ZZ4lep.merge.NTUP_HSG2.e2777_s1831_s1741_r4829_r4540_p1344/
$0^+_h : g_1 = 0, g_2 = 1, g_4 = 0$	8 TeV	mc12_8TeV.181992.PowhegJHUPythia8_CT10_ggH125p5_Spin0ph_ZZ4lep.merge.NTUP_HSG2.e2595_s1831_s1741_r4829_r4540_p1344/
0^-: $g_1 = 0, g_2 = 0, g_4 = 1$	8 TeV	mc12_8TeV.181991.PowhegJHUPythia8_CT10_ggH125p5_Spin0m_ZZ4lep.merge.NTUP_HSG2.e2595_s1831_s1741_r4829_r4540_p1344/
Spin-0, $g_1 = 1, g_2 = 1 + i, g_4 = 0$	8 TeV	mc12_8TeV.181994.PowhegJHUPythia8_CT10_ggH125p5_Spin0_g1_1_g2_1pi_g4_0_ZZ4lep.merge.NTUP_HSG2.e2595_s1831_s1741_r4829_r4540_p1344/
Spin-0, $g_1 = 1, g_2 = 0, g_4 = 2 + 2i$	8 TeV	mc12_8TeV.181993.PowhegJHUPythia8_CT10_ggH125p5_Spin0_g11g20g42p2i_ZZ4lep.merge.NTUP_HSG2.e2595_s1831_s1741_r4829_r4540_p1344/
Spin-0, $g_1 = 0, g_2 = 1, g_4 = 1$	8 TeV	mc12_8TeV.181995.PowhegJHUPythia8_CT10_ggH125p5_Spin0_g1_0_g2_1_g4_1_ZZ4lep.merge.NTUP_HSG2.e2595_s1831_s1741_r4829_r4540_p1344/
Spin-0, $g_1 = 1, g_2 = 1, g_4 = 1$	8 TeV	mc12_8TeV.181996.PowhegJHUPythia8_CT10_ggH125p5_Spin0_g1_1_g2_1_g4_1_ZZ4lep.merge.NTUP_HSG2.e2595_s1831_s1741_r4829_r4540_p1344/
Spin-0, $g_1 = 1, g_2 = 1 + i, g_4 = 1 + i$	8 TeV	mc12_8TeV.181990.PowhegJHUPythia8_CT10_ggH125p5_Spin0_g11g21pig41pi_ZZ4lep.merge.NTUP_HSG2.e2595_s1831_s1741_r4829_r4540_p1344/
2^+_m: $g_1 = 1, g_5 = 1$	8 TeV	mc12_8TeV.181997.PowhegMadGraphPythia6_CT10_ggH125p5_Spin2mh_ZZ4lep.merge.NTUP_HSG2.e2847_s1831_s1741_r4829_r4540_p1344/
$0^+ : g_1 = 1, g_2 = 0, g_4 = 0$	7 TeV	mc11_7TeV.189606.PowhegJHUPythia8_CT10_ggH125p5_Spin0_g1_1_g2_0_g4_0_ZZ4lep.merge.NTUP_HSG2.e2776_s1786_s1787_r4980_r4982_p1486/
$0^+_h : g_1 = 0, g_2 = 1, g_4 = 0$	7 TeV	mc11_7TeV.181992.PowhegJHUPythia8_CT10_ggH125p5_Spin0ph_ZZ4lep.merge.NTUP_HSG2.e2594_s1786_s1787_r4980_r4982_p1486/
$0^- : g_1 = 0, g_2 = 0, g_4 = 1$	7 TeV	mc11_7TeV.181991.PowhegJHUPythia8_CT10_ggH125p5_Spin0m_ZZ4lep.merge.NTUP_HSG2.e2594_s1786_s1787_r4980_r4982_p1486/
Spin-0, $g_1 = 1, g_2 = 1 + i, g_4 = 0$	7 TeV	mc11_7TeV.181994.PowhegJHUPythia8_CT10_ggH125p5_Spin0_g1_1_g2_1pi_g4_0_ZZ4lep.merge.NTUP_HSG2.e2594_s1786_s1787_r4980_r4982_p1486/
Spin-0, $g_1 = 1, g_2 = 0, g_4 = 2 + 2i$	7 TeV	mc11_7TeV.181993.PowhegJHUPythia8_CT10_ggH125p5_Spin0_g11g20g42p2i_ZZ4lep.merge.NTUP_HSG2.e2594_s1786_s1787_r4980_r4982_p1486/
Spin-0, $g_1 = 0, g_2 = 1, g_4 = 1$	7 TeV	mc11_7TeV.181995.PowhegJHUPythia8_CT10_ggH125p5_Spin0_g1_0_g2_1_g4_1_ZZ4lep.merge.NTUP_HSG2.e2594_s1786_s1787_r4980_r4982_p1486/
Spin-0, $g_1 = 1, g_2 = 1, g_4 = 1$	7 TeV	mc11_7TeV.181996.PowhegJHUPythia8_CT10_ggH125p5_Spin0_g1_1_g2_1_g4_1_ZZ4lep.merge.NTUP_HSG2.e2594_s1786_s1787_r4980_r4982_p1486/
Spin-0, $g_1 = 1, g_2 = 1 + i, g_4 = 1 + i$	7 TeV	mc11_7TeV.181990.PowhegJHUPythia8_CT10_ggH125p5_Spin0_g11g21pig41pi_ZZ4lep.merge.NTUP_HSG2.e2594_s1786_s1787_r4980_r4982_p1486/
2^+_m: $g_1 = 1, g_5 = 1$	7 TeV	mc11_7TeV.181997.PowhegMadGraphPythia6_CT10_ggH125p5_Spin2mh_ZZ4lep.merge.NTUP_HSG2.e2848_s1786_s1787_r4980_r4982_p1486/

Table A.2. MC samples of final state interference used for the spin-CP analysis.

Description	$\sqrt{s}$	Dataset
$0^+ \rightarrow ZZ \rightarrow 4e$	8 TeV	mc12_8TeV.181607.Prophecy4fPowhegPythia8_AU2CT10_ggH125_ZZ4e.merge.NTUP_HSG2.e2508_s1831_s1741_r4829_r4540_p1344/
$0^+ \rightarrow ZZ \rightarrow 2e2\mu$	8 TeV	mc12_8TeV.181608.Prophecy4fPowhegPythia8_AU2CT10_ggH125_ZZ2e2mu.merge.NTUP_HSG2.e2490_s1831_s1741_r4829_r4540_p1344/

4. - $p_T(l) > 20, 15, 10, 6\text{GeV}$

These acceptance cuts have been chosen to be as much close as possible to the cuts applied to select signal events in data and in full simulated MC samples. Figure A.1 shows some of the relevant kinematic and angular distributions predicted by JHU and PowHeg assuming $J^P = 0^+$ Higgs. All of these agree within the statistical errors. On the other hand, some difference between the transverse momenta distributions of the LO and NLO generators is observed, as expected. Figure A.2 shows that the SM Higgs p_T distribution in JHU is harder with respect to the one in PowHeg, which uses an NLO prediction. This brings to some discrepancy on the prediction of acoplanarity as well1, being these two variables closely related. This discrepancy has no large impact on the spin-parity states separation as long as the Higgs p_T related variables are not used as discriminants in the analysis.

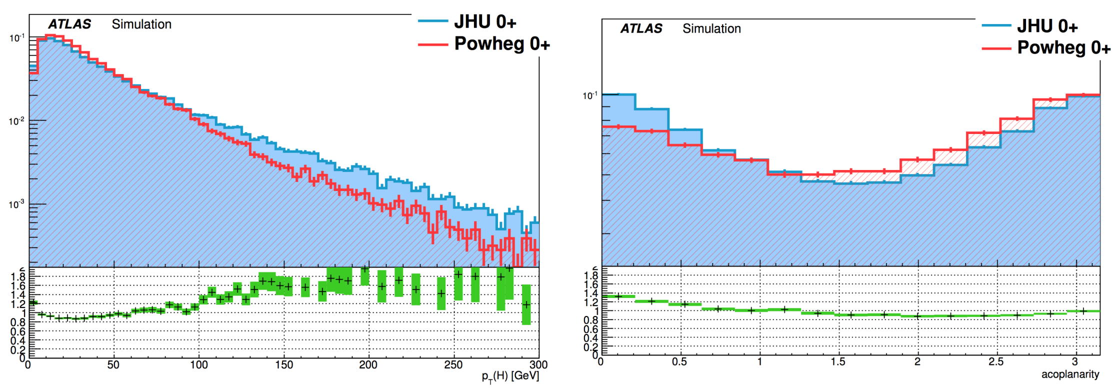

Figure A.1. Comparison between JHU (blue) and POWHEG (red) predictions for SM Higgs p_T and acoplanarity. The ratio between the two predictions is also shown with the statistical error on the bottom of each plot.

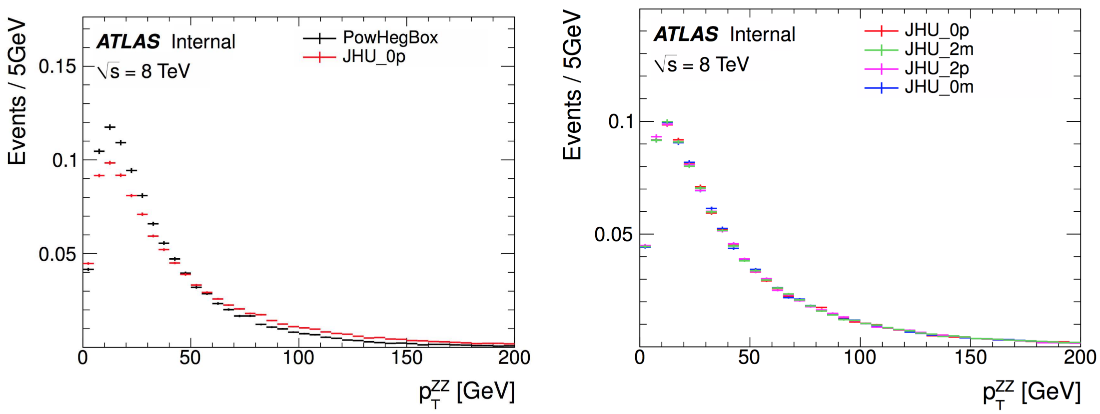

Figure A.2. Comparison of predicted p_T spectra for resonances produced in gg collisions. (a) JHU 0^+ and PowHeg Standard Model Higgs. (b) JHU states with different spin and parity.

A.4. Reco-truth unfolding method

A third method uses the $\ell\ell+XX$ data control region; however, the two subleading electrons have only the electron identification relaxed and do not have an inverted selection applied as for the transferfactor method. This control region thus contains all backgrounds, including the ZZ^* background, and the $H \to ZZ^* \to 4\ell$ signal. The extrapolation to the signal region is performed with the $Z+X$ simulation. This method was used as the baseline for previous publications, but is now superseded by the $3\ell+X$ method, which provides the smallest uncertainties of the data-driven methods. Using the simulation, each of the paired reconstruction categories (EE, EF, FE and FF) of the $\ell\ell+XX$ sample is decomposed into its background origin components ($ee, ff, \gamma\gamma, qq$ and the 12 cross combinations), where the e background category is introduced to contain the isolated electrons from ZZ^* and $H \to ZZ^* \to 4\ell$. This 4×16 composition table is summed with efficiency weights, in bins of p_T and η, obtained from the $Z+X$ simulation, which is corrected from comparison with data as previously mentioned. To remove the ZZ^* and $H \to ZZ^* \to 4\ell$ contributions from this estimate, the background origin category ee is removed from the sum, and an estimated residual of 1.2 ± 0.4 ZZ^* events are subtracted to obtain the final result, which is also given in Table 5.2.4.1.

REFERENCES

[1] https://twiki.cern.ch/twiki/bin/view/atlaspublic/muontriggerpublicresults.

[2] Muon reconstruction efficiency in reprocessed 2010 LHC proton-proton collision data recorded with the ATLAS detector. Tech. Rep. ATLAS-CONF-2011-063, CERN, Geneva, Apr 2011.

[3] Combined measurements of the mass and signal strength of the Higgs-like boson with the ATLAS detector using up to 25 fb^{-1} of proton-proton collision data. Tech. Rep. ATLAS-CONF-2013-014, CERN, Geneva, Mar 2013.

[4] Study of the spin of the Higgs-like boson in the two photon decay channel using 20.7 fb^{-1} of pp collisions collected at $\sqrt{s}$ = 8 TeV with the ATLAS detector. Tech. Rep. ATLAS-CONF-2013-029, CERN, Geneva, Mar 2013.

[5] Study of the spin of the new boson with up to 25 fb^{-1} of ATLAS data. Tech. Rep. ATLAS-CONF-2013-040, CERN, Geneva, Apr 2013.

[6] Study of the spin properties of the Higgs-like particle in the $\boldsymbol{H \rightarrow WW^{(*)} \rightarrow e\nu\mu\nu}$ channel with 21 fb^{-1} of $\sqrt{s}$ = 8 TeV data collected with the ATLAS detector. Tech. Rep. ATLAS-CONF-2013-031, CERN, Geneva, Mar 2013.

[7] Updated coupling measurements of the Higgs boson with the ATLAS detector using up to 25 fb^{-1} of proton-proton collision data. Tech. Rep. ATLAS-CONF-2014-009, CERN, Geneva, Mar 2014.

[8] Measurements of the Higgs boson production and decay rates and coupling strengths using pp collision data at s = 7 and 8 TeV in the ATLAS experiment. Tech. Rep. ATLAS-CONF-2015-007, CERN, Geneva, Mar 2015.

[9] Study of the spin and parity of the Higgs boson in HVV decays with the ATLAS detector. Tech. Rep. ATLAS-CONF-2015-008, CERN, Geneva, Mar 2015.

[10] Aad, G., et al. The ATLAS Experiment at the CERN Large Hadron Collider. *JINST 3* (2008), S08003.

[11] Aad, G., et al. Expected Performance of the ATLAS Experiment - Detector, Trigger and Physics.

[12] Aad, G., et al. Electron and photon energy calibration with the ATLAS detector using LHC Run 1 data. *Eur.Phys.J. C74*, 10 (2014), 3071.

[13] Aad, G., et al. Electron reconstruction and identification efficiency measurements with the ATLAS detector using the 2011 LHC proton-proton collision data. *Eur.Phys.J. C74*, 7 (2014), 2941.

[14] Aad, G., et al. Measurements of Four-Lepton Production at the Z Resonance in pp Collisions at $\sqrt{s}$ =7 and 8 TeV with ATLAS. *Phys.Rev.Lett. 112*, 23 (2014), 231806.

[15] Aad, G., et al. Measurements of Higgs boson production and couplings in the four-lepton channel in pp collisions at center-of-mass energies of 7 and 8 TeV with the ATLAS detector. *Phys.Rev. D91*, 1 (2015), 012006.

[16] Ali, A. *Higgs Particle(s): Physics Issues and Experimental Searches in High-Energy Collisions.* 2013.

[17] Bernstein, J. Spontaneous symmetry breaking, gauge theories, the Higgs mechanism and all that. *Rev. Mod. Phys. 46* (Jan 1974), 7–48.

[18] Bolognesi, S., Gao, Y., Gritsan, A. V., Melnikov, K., Schulze, M., et al. On the spin and parity of a single-produced resonance at the LHC. *Phys.Rev. D86* (2012), 095031.

[19] Bozzi, G., Catani, S., de Florian, D., and Grazzini, M. Transverse-momentum resummation and the spectrum of the Higgs boson at the LHC. *Nucl.Phys. B737* (2006), 73–120.

[20] Bredenstein, A., Denner, A., Dittmaier, S., and Weber, M. M. Precise predictions for the Higgs-boson decay $H \to WW/ZZ \to 4$ leptons. *Phys. Rev. D 74* (Jul 2006), 013004.

[21] Carena, M., and Haber, H. E. Higgs boson theory and phenomenology. *Prog.Part.Nucl.Phys. 50* (2003), 63–152.

[22] Collaboration, A. Electron performance measurements with the ATLAS detector using the 2010 LHC proton-proton collision data, 2011. ATLAS-COM-PHYS-2011-546.

[23] Collaboration, A. Improved electron reconstruction in ATLAS using the Gaussian Sum Filter-based model for bremsstrahlung. Tech. Rep. ATLAS-CONF-2012-047, CERN, Geneva, May 2012.

[24] Collaboration, A. 4leptons selection cut flow chart, 2013.

[25] Collaboration, A. Measurements of the properties of the Higgs-like boson in the four lepton decay channel with the ATLAS detector using 25 fb1 of proton-proton collision data. Tech. Rep. ATLAS-CONF-2013-013, CERN, Geneva, Mar 2013.

[26] Collaboration, T. A. *Expected performance of the ATLAS experiment: detector, trigger and physics*. CERN, Geneva, 2009.

[27] Collaboration, T. A. Preliminary results on the muon reconstruction efficiency, momentum resolution, and momentum scale in ATLAS 2012 pp collision data. Tech. Rep. ATLAS-CONF-2013-088, CERN, Geneva, Aug 2013.

[28] Collins, J. C., and Soper, D. E. Angular distribution of dileptons in high-energy hadron collisions. *Phys. Rev. D 16* (Oct 1977), 2219–2225.

[29] Cowan, G., Cranmer, K., Gross, E., and Vitells, O. Asymptotic distribution for two-sided tests with lower and upper boundaries on the parameter of interest.

[30] de Florian, D., Ferrera, G., Grazzini, M., and Tommasini, D. Transverse-momentum resummation: Higgs boson production at the Tevatron and the LHC. *JHEP 1111* (2011), 064.

[31] Dittmaier, S., Mariotti, C., et al. Handbook of LHC Higgs Cross Sections: 1. Inclusive Observables.

[32] et al., K. O. *The Review of Particle Physics*. July 2014.

[33] et al., K. O. *The Review of Particle Physics*. July 2014.

[34] Gao, Y., Gritsan, A. V., Guo, Z., Melnikov, K., Schulze, M., et al. Spin determination of single-produced resonances at hadron colliders. *Phys. Rev. D 81* (2010), 075022.

[35] Gao, Y., Gritsan, A. V., Guo, Z., Melnikov, K., Schulze, M., and Tran, N. V. Spin determination of single-produced resonances at hadron colliders. *Phys. Rev. D 81* (Apr 2010), 075022.

[36] Hassani, S., Chevalier, L., LanCon, E., Laporte, J., Nicolaidou, R., and Ouraou, A. A muon identification and combined reconstruction procedure for the ATLAS detector at the LHC using the (MUONBOY, STACO, MuTag) reconstruction packages. *Nuclear Instruments and Methods in Physics Research A 572* (mar 2007), 77–79.

[37] Heinemeyer, S., et al. Handbook of LHC Higgs Cross Sections: 3. Higgs Properties.

[38] Henderson, J. Discriminative Training of a Neural Network Statistical Parser, 2004.

[39] Hoecker, A., Speckmayer, P., Stelzer, J., Therhaag, J., and etc. TMVA - Toolkit for Multivariate Data Analysis. *ArXiv Physics e-prints* (mar 2007).

[40] Kibble, T. W. B. Englert-Brout-Higgs-Guralnik-Hagen-Kibble mechanism, 2008.

[41] Kibble, T. W. B. Englert-Brout-Higgs-Guralnik-Hagen-Kibble mechanism, 2008.

[42] Kibble, T. W. B. Englert-Brout-Higgs-Guralnik-Hagen-Kibble mechanism, 2008.

[43] Klamke, G., and Zeppenfeld, D. Hjj production: Signals and CP measurements.

[44] Kniehl, B. A. Standard model of the electroweak interaction: Theoretical developments.

[45] Lagouri, T., Adams, D., Assamagan, K., Biglietti, M., Carlino, G., et al. A Muon Identification and Combined Reconstruction Procedure for the ATLAS Detector at the LHC at CERN. *IEEE Trans.Nucl.Sci. 51* (2004), 3030–3033.

[46] Mohapatra, R. N. *Spontaneous Symmetry Breaking, Nambu-Goldstone Bosons, and the Higgs Mechanism*. 1986.

[47] Nambu, Y. Quasi-particles and gauge invariance in the theory of superconductivity. *Phys. Rev. 117* (Feb 1960), 648–663.

[48] Oleari, C. The POWHEG-BOX. *Nucl.Phys.Proc.Suppl. 205-206* (2010), 36–41.

[49] Peskin, M. E., and Schroeder, D. V. *An Introduction to Quantum Field Theory; 1995 ed.* Westview, Boulder, CO, 1995. Includes exercises.

[50] Pivk, M., and Le Diberder, F. R. Plots: A statistical tool to unfold data distributions. *Nuclear Instruments and Methods in Physics Research A 555* (dec 2005), 356–369.

[51] Plehn, T. *Lectures on LHC Physics*. Springer Cham Heidelberg New York Dordrecht London, 2014.

[52] the ATLAS collaboration, T. C. F. Measurements of Higgs Boson Properties using the ATLAS Detector.

[53] Verkerke, W., and Kirkby, D. RooFit Users Manual v2. 91. Tech. rep., 2008.

[54] Webber, D., et al. Measurement of the Positive Muon Lifetime and Determination of the Fermi Constant to Part-per-Million Precision. *Phys.Rev.Lett. 106* (2011), 041803.

[55] Welling, M. Fisher linear discriminant analysis. *Department of Computer Science, University of Toronto 3* (2005).

[56] Wikipedia, t. f. e. Crystal Ball function, 2013.

[57] Zeppenfeld, J. T. C. E. M. W. D. *Physics in D ¿ 4 : proceedings of the Theoretical Advanced Study Institute in Elementary Particle Physics : Boulder, CO, USA, 6 June-2 July 2004*. 2006.